Ion-Desorption and Photoemission Studies of NO, O_2 and K Adsorbed Si(111) Surfaces

Kazuyuki Sakamoto

Department of Material Physics,
Faculty of Engineering Science,
Osaka University

January 28, 1994

Abstract

The adsorption states and desorption processes of ions on the Si(111) surface were studied by means of ESD for the O_2/Si(111) surface and by means of both ESD and PSD for the NO/Si(111) surface. We also studied the surface electronic states of Si(111)3×1-K using ARUPS.

The ESD experiment of the O_2/Si(111) was done at room temperature. At low oxygen exposures (1 and 2 L), desorbed H^+, O^+ and O_2^+ were observed, whereas only H^+ and O^+ were observed at high exposures (above 4 L). This was the first observation of O_2^+ in the ESD experiment. With increasing the coverage, the signal of O_2^+ disappeared. So, it is concluded that the oxygen adsorbs only dissociatively at high exposure, and molecular surface species survive only at low coverage at room temperature. The patterns of ESDIAD are reconciled with the model that the molecular surface species are adsorbed at the on-top site. Its lifetime and the thermal activation energy was measured to be about 8 hours and 0.56 eV, respectively, for 1 L exposure.

In the ESD experiment of the NO/Si(111) surface, the desorbed ion species were H^+ and O^+ at room temperature. In addition, N^+ was observed for the first time in the ESD experiment at 190 K. We have found two types of N^+ which have different kinetic energies. From the ESDIAD patterns, we have found that these two types correspond to two adsorption sites of NO. In the PSD experiment, NO^+, O_2^+ and N_2O^{2+} were observed for the first time in addition to the H^+, O^+ and N^+ ions at 90 K. From the photon energy dependence of the PSD experiment and the UPS spectra, we have found that N^+ desorbs from the molecularly adsorbed NO through the excitation of the 3σ molecular orbital (mainly O 2s). This result suggests that N^+ ions desorb from the NO molecules which are bonding to the surface Si atoms with the O atoms.

Surface electronic states of the Si(111)3×1-K surface were studied by means of ARUPS along the $[11\bar{2}]$ and the $[10\bar{1}]$ directions. Comparing the spectra of the Si(111)7×7 clean surface and that of the Si(111)3×1-K surface, we have found that the 3×1-K surface is no longer metallic as the 7×7 clean surface but semiconducting. Judging from its dispersion behavior, the 3×1-K surface seems to contain π-bonded chains. The saturation coverage of K on the Si(111)3×1-K surface is found to be 1/3 ML from the comparison of the intensity ratio between the Si *LVV* Auger and K 2p peaks with that of the Si(111)δ7×7-K surface, on which the saturation coverage is considered to be 1 ML. From these results, we suggest a new surface geometrical structure model for the Si(111)3×1-K surface.

Acknowledgements

The author would like to express his sincere gratitude to Professor Shigemasa Suga for his stimulating discussions and a careful reading of the manuscript. He is also grateful to Professor Hiroshi Daimon for introducing him to the problems of this thesis. He is thankful to Professor Akihito Kakizaki and Doctor Toyohiko Kinoshita of the Institute for Solid State Physics (ISSP) of the University of Tokyo, Doctor Hidetoshi Namba of the Faculty of Science of the University of Tokyo, and the staff and graduate students of SRL, ISSP, the University of Tokyo and Hiroshima University for their hospitality during the experiment at Photon Factory of the National Laboratory. He would like to express his thanks to Professor Kikuo Cho, Professor Kenji Makoshi and Dr. Yasushi Ohfuchi of Osaka University for their critical discussions. He also thanks Dr. Shin Imada and other members of Suga research group for their encouragement and friendly help in accomplishing this thesis. This work was partly supported by a Grant in Aid for Scientific Research from Ministry of Education, Science and Culture of Japan.

Contents

Abstract i

Acknowledgements ii

Acronyms 3

1 Introduction 4

1.1 Preface 4

1.2 Si(111)7×7 and 2×1 clean surface 7

1.3 Desorption Processes 17

1.3.1 MGR model 17

1.3.2 Antoniewicz model 20

1.3.3 KF model 24

1.3.4 Other models 26

1.4 Principle of ESDIAD 27

1.5 Principle of ARUPS 30

1.6 Two-dimensional display-type spherical mirror analyzer 35

1.6.1 Charged particle orbit 37

1.6.2 Energy resolution 40

2 ESD studies of the O_2/Si(111) surface 45

2.1 Preface 45

2.2 Experimental 51
2.3 Results and discussion 51
2.4 Summary 61

3 ESD and PSD studies of the NO/Si(111) surface **63**
3.1 Preface 63
3.2 Experimental 66
3.2.1 ESD 67
3.2.2 PSD 68
3.3 Results and discussion 70
3.3.1 ESD 70
3.3.2 PSD 76
3.4 Summary 86

4 Photoemission studies of the Si(111)3×1-K surface **87**
4.1 Preface 87
4.2 Experimental 92
4.3 Results and discussion 95
4.4 Summary 113

5 Summary **115**

Bibliography **118**

List of Publications **123**

Acronyms

AES	Auger electron spectroscopy
ASD	Auger stimulated desorption
ARUPS	angle-resolved ultraviolet photoelectron spectroscopy
CITS	current-imaging-tunneling spectroscopy
DAS	dimer-adatom-stacking-fault
DIET	desorption induced by electronic transitions
DOS	density of states
EELS	electron energy loss spectroscopy
ESD	electron stimulated desorption
ESDIAD	electron stimulated desorption ion angular distribution
HREELS	high-resolution electron energy loss spectroscopy
IPES	inverse photoelectron spectroscopy
ISS	ion scattering spectroscopy
JDOS	joint density of states
KRIPES	k-resolved inverse photoelectron spectroscopy
LEED	low energy electron diffraction
PES	photoelectron spectroscopy
PSD	photon stimulated desorption
RHEED	reflection high energy electron diffraction
SBZ	surface Brillouin zone
SIMS	secondary ion mass spectroscopy
STM	scanning tunnelling microscopy
STS	scanning tunnelling spectroscopy
TED	transmission electron diffraction
TD	thermal desorption
TOF	time of flight
TPD	temperature programmed desorption
UHV	ultra-high vacuum
UPS	ultraviolet photoelectron spectroscopy
VUV	vacuum-ultra-violet
XESD	X-ray electron stimulated desorption
XPS	X-ray photoelectron spectroscopy

Chapter 1

Introduction

1.1 Preface

The surface is different from the bulk because the effective dimensionality is only two and not three, and so the surface is a place where various chemical reactions and physical phenomena occur. Due to the development of the ultra-high vacuum (UHV) technique and experimental methods like scanning tunnelling microscopy (STM) in recent years, studies of the surface became more and more extensive.

Generally, to lower the free energy and to become more stabilized, surface atoms of many crystals reconstruct and make different periodic structures from those of bulk atoms. Among them, the reconstructed Si(111)7×7 clean surface is well known. The details of this surface will be explained in section 1.2 . There are many techniques (for example, low energy electron diffraction (LEED), reflection high energy electron diffraction (RHEED), ion scattering spectroscopy (ISS) and STM) to study the arrangements or the regularity of the surface atoms. STM is very useful since it is a device which provides directly the real space images of surface topography on the atomic scale. These techniques are also useful to know the change of the reconstructed surface structure when different species atoms are adsorbed on the sample surface. In recent years, the technique of photoelectron holography has been developed to get informations about the position and the distance of the surface atoms and adsorbates, that is about the three dimensional atomic structure by

simple Fourier transformation.

The electronic states of the surface are also different from those of the bulk on account of the same reason of the atom rearrangement. For example, the band bending occurs at the semiconductor surface to produce the Fermi level pinning (which means that the work function hardly changes with the quantity of impurity doping). Auger electron spectroscopy (AES), electron energy loss spectroscopy (EELS), X-ray photoelectron spectroscopy (XPS) and ultraviolet photoelectron spectroscopy (UPS) are the techniques which are used to measure the occupied surface electronic states. Moreover, by the use of the angle-resolved measurements in the photoelectron experiments, the complete surface state band structure has been determined for several surfaces. The principle of this method will be explained in section 1.5. Inverse photoelectron spectroscopy (IPES) is a method to measure the unoccupied surface states.

Studies of gases adsorptions on the surfaces are important to know the oxidation or the catalysis processes of crystals. EELS is a technique to know the adsorption site of the adsorbed atoms and/or molecules, measuring the vibrational mode. Electron stimulated desorption (ESD), photon stimulated desorption (PSD) and temperature programmed desorption (TPD) are used to study the adsorption sites and the desorption processes. The damage of surface in ESD and PSD experiments is much less than that in TPD experiment. So, we can say that ESD and PSD are useful methods to study the adsorbates.

As for the above analysis methods, which use electron for the primary (or secondary) probe, we have to consider the role of the mean free path of the incident (or emitted) electron. Figure 1.1 shows the inelastic mean free path versus electron kinetic energy [1]-[3]. The origins of the inelastic process are plasmon excitation, electron excitation, and so on. Looking at Fig. 1.1, we remark that the mean free path has a minimum near 70eV. And so, when we make the electron spectroscopy, we have to choose the kinetic energy of the electron to get maximum surface's informations. The mean free path of the low

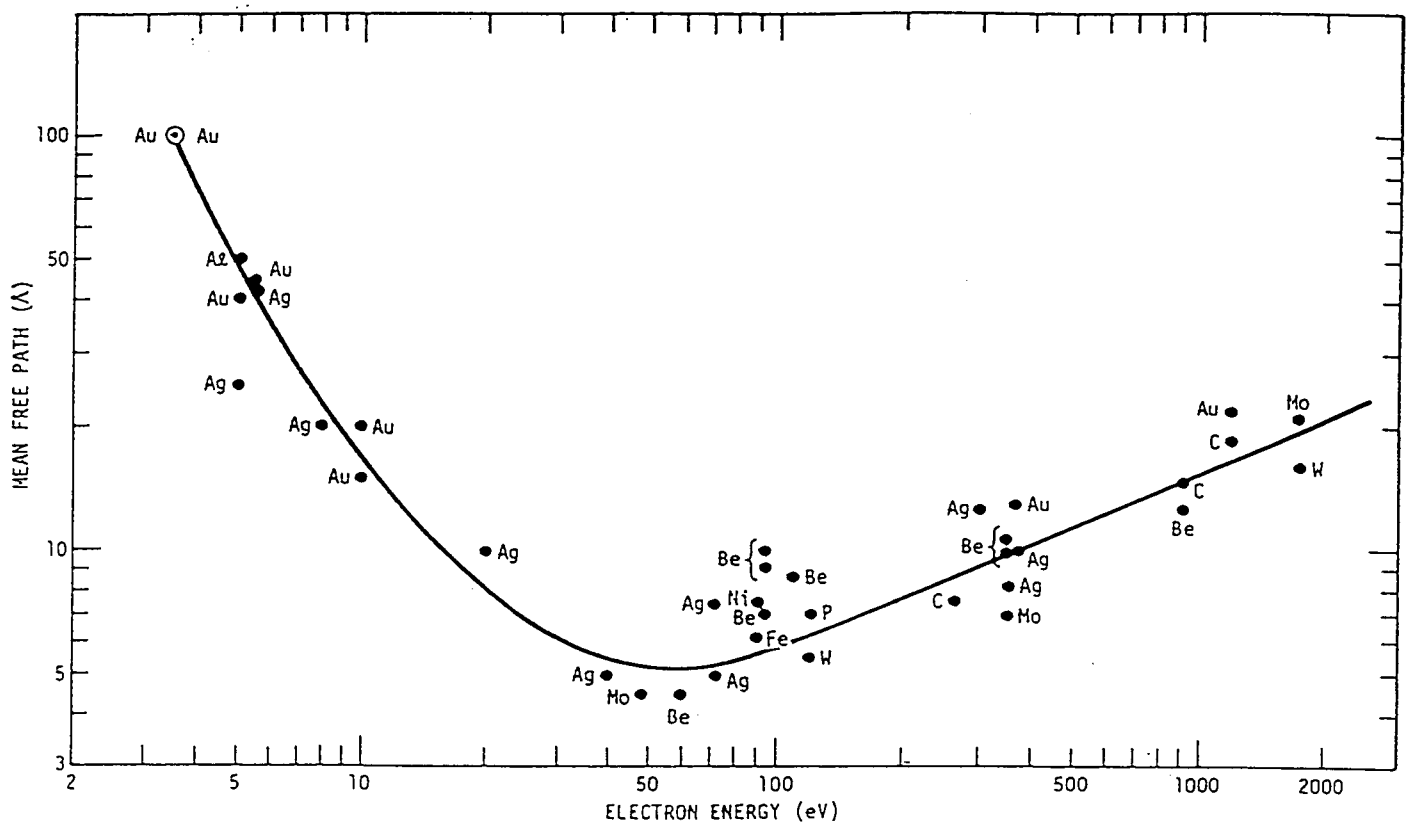

Figure 1.1: "Universal curve" for the electron mean free path as a function of electron kinetic energy. Dots indicate individual measurements. (from ref.[2])

kinetic energy electrons becomes longer since they cannot excite plasmons, and those of the high kinetic energies becomes longer because they have a small cross section to lose their energy. This is the origin of the minimum of the mean free path. Considering this mean free path, we can easily understand that UPS is more sensitive than XPS to study the surface electronic states.

In this thesis, I would like to mention or describe about the studies of adsorption sites and desorption processes of oxygen from the O_2/Si(111) surface by means of ESD, those of nitric oxide from the NO/Si(111) surface using ESD and PSD, and the electronic structure of the Si(111)3×1-K surface by the angle-resolved UPS (ARUPS) method (chapters 2, 3 and 4, respectively).

1.2 Si(111)7×7 and 2×1 clean surface

When we cleave a Si crystal, we can observe a Si(111)2×1 reconstructed surface at first. The buckling model [4] (Fig. 1.2(a)) with alternate rows of the surface atoms moving in and out of the surface had been the most accepted model for this surface. However, according to the result of the polarization-dependent ARUPS [5] and the core-level shifts [6], Pandey [7][8] proposed a new model, π-bonded chain model, which contains π-bonded chains as shown by its name, for this surface. Figure 1.2(b) shows the surface structure of the π-bonded chain model. Regarding the first and the second layers, we can remark that this surface structure is similar to that of the ideal Si(110) surface. The surface states calculated by Pandey [7] is shown in Fig. 1.3. $\bar{\Gamma}, \bar{\mathrm{J}}, \bar{\mathrm{J}}'$ and $\bar{\mathrm{K}}'$ are the symmetry points of the surface Brillouin zone (SBZ) and the parameter Δd_c is the bond-length contraction of 0.1Å. The first observation on the surface state of Si(111)2×1 surface was obtained from the angle-integrated photoelectron spectroscopy by Eastman *et al.*[9] and Wagner *et al.*[10]. Many ARUPS measurements (for example, ref.[5],[11]-[14]) were done for this surface, but

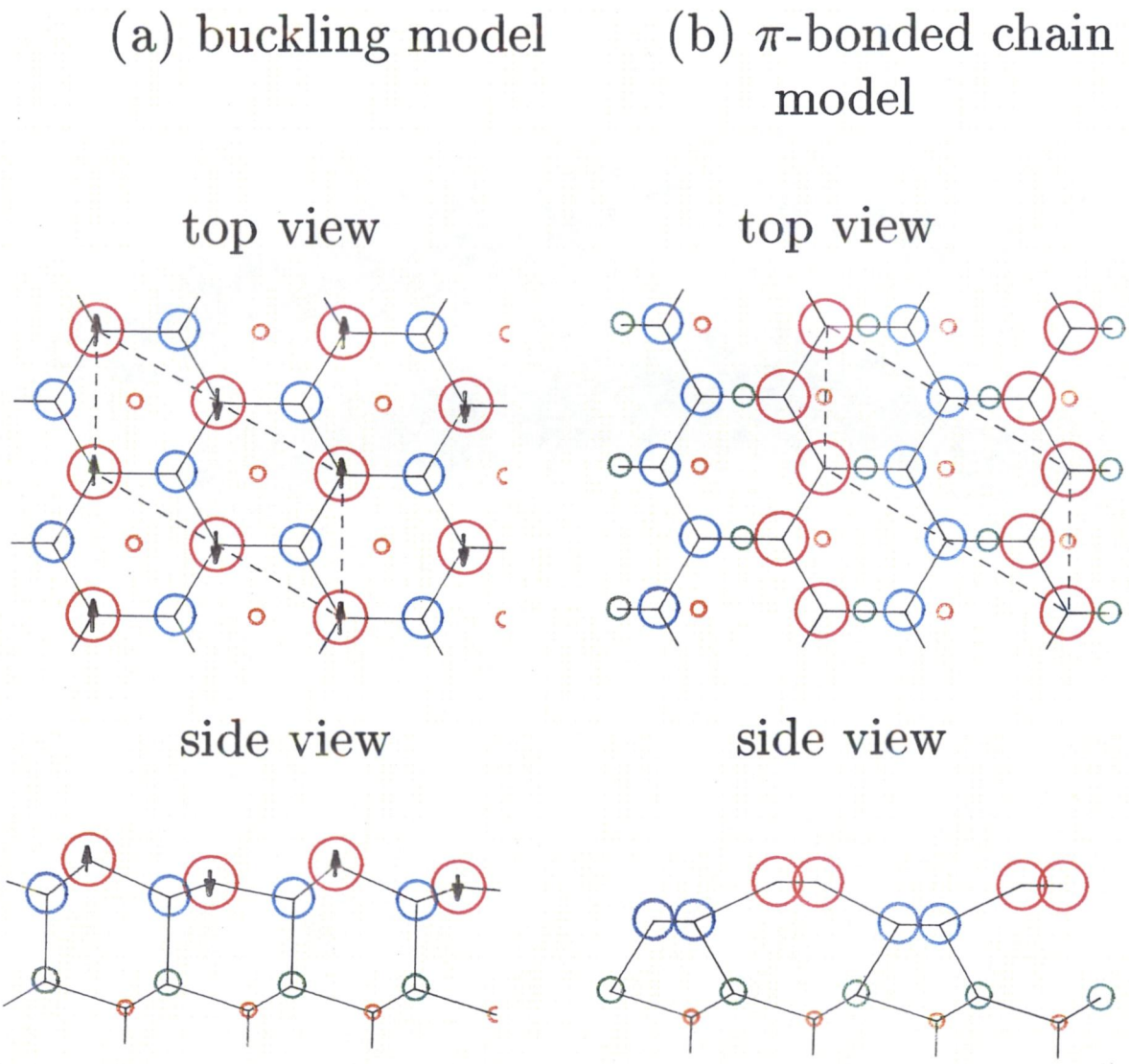

Figure 1.2: Geometrical structure model for the Si(111)2×1 surface. ((a)The buckling model and (b) the π-bonded chain model.) Arrows indicate the movements of the surface atoms (in and out of the surface). The broken lines are the unit cells of the 2×1 structure.

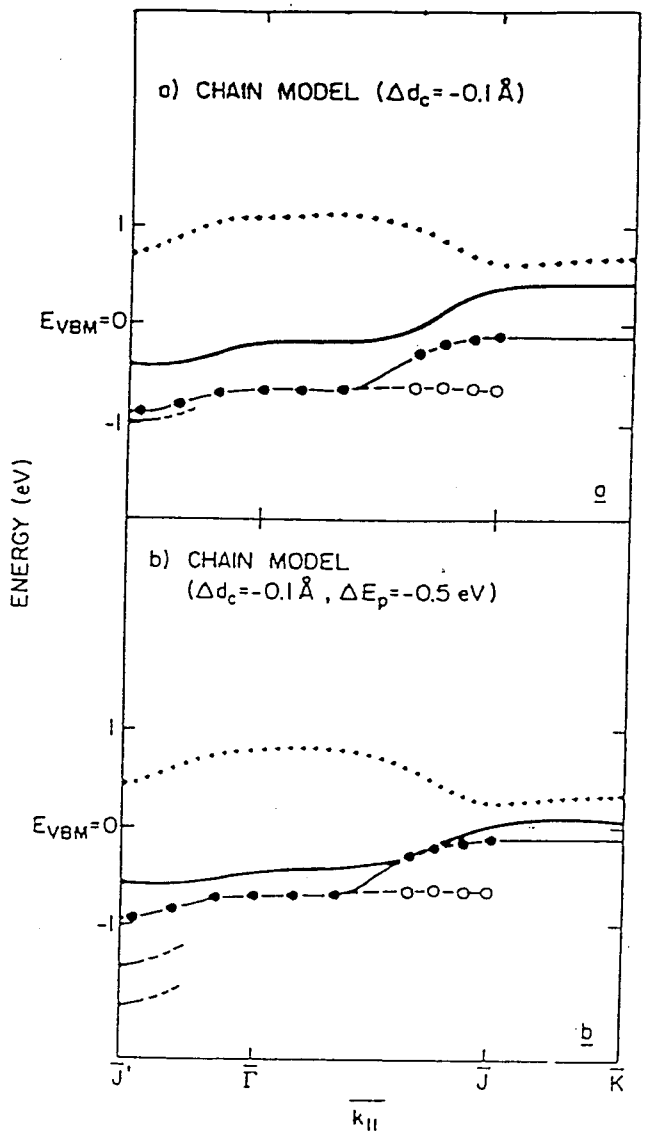

Figure 1.3: Results for two different calculated surface states for the π-bonded chain model of Si(111)2×1 surface (given by the dotted and solid lines) compared with the UPS results (filled and open circles). (from ref.[7])

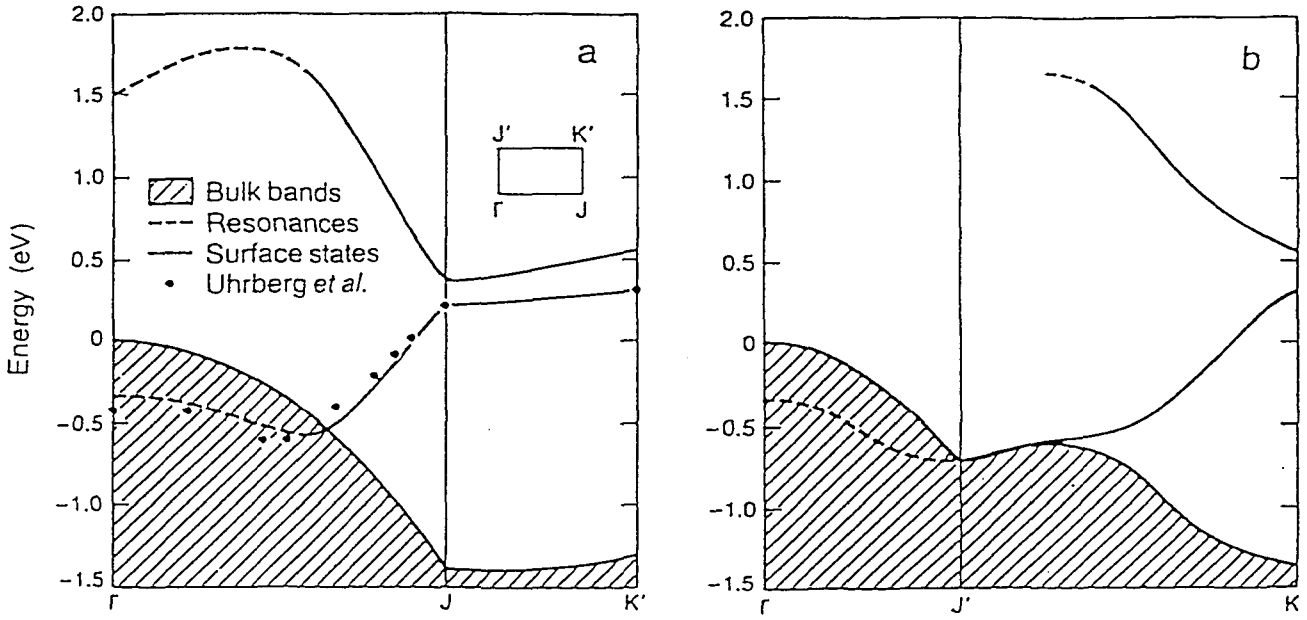

Figure 1.4: Calculated dispersion of the surface states and resonances along the $\bar{\Gamma} \rightarrow \bar{J} \rightarrow \bar{K}'$ (a) and the $\bar{\Gamma} \rightarrow \bar{J}' \rightarrow \bar{K}'$ (b) directions. The dotted points are the experimental data of Uhrberg *et al.*[12]. (from ref.[15])

their results were different from each other. One of the reasons for this discrepancy is that the Si(111)2×1 surface has low symmetry and the dispersion has been measured for inequivalent directions. Among these, the surface states calculated by Northrup *et al.*[15] and the experimental data of Uhrberg *et al.*[12] show a good agreement. These results are shown is Fig. 1.4. We can recognize that the dispersion calculated by Northrup is a little different from that of Pandey. That is, the dispersion of Pandey has no minimum along the $\bar{\Gamma} - \bar{\mathrm{J}}$ direction. The experiment of the unoccupied surface-state was done by, for example Perfetti *et al.*[16] using the k-resolved IPES (KRIPES) method. Their data are shown in Fig. 1.5 with the calculated dispersion of Pandey [17]. Due to the one-dimensional π-bonded chain, this surface is in principle a one dimensional metal, but practically some distortion can induce a band gap and a semiconducting character.

The Si(111) surface changes to a 1×1 structure at high temperature. Cooling down this high-temperature phase, we obtain a 7×7 structure. This phase transition has been observed using electron microscope by Osakabe *et al.*[18]. The structure of the 7×7 surface has been discussed for a long time. Takayanagi *et al.* proposed the dimer-adatom-stacking-fault (DAS) model in 1985 [19]. The top and side views of the DAS model are shown in Figs. 1.6(a) and (b), respectively. The circles represent Si atoms, the largest ones the adatoms, the second largest ones those of the first layer, etc. The filled green circles are the Si atoms which form dimers. This model has dimers, adatoms and stacking-fault as meant by its name. We can see the existence of stacking-fault in the left half of the unit cell of DAS model. The marks F and U, in the lozenge at the upside of the figure, indicate the faulted part and unfaulted part of the unit cell, respectively. The layers of the unfaulted part stack as

(bulk) ··· C'A A'B B'C C'A adatom layer

and those of the faulted part stack as

(bulk) ··· C'A A'B B'C C'B adatom layer

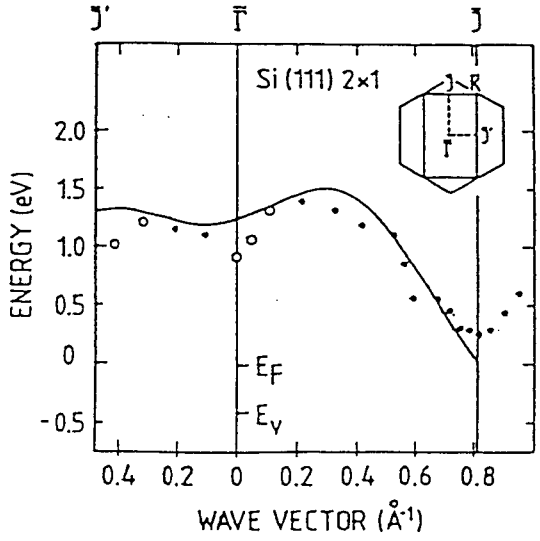

Figure 1.5: Unoccupied surface state of the Si(111)2×1 surface. The dots and open circles are from ref.[16] and the solid line represents the energy dispersion calculated by Pandey[17]. E_{V} indicate the position of the valence-band edge ($E_{\mathrm{V}} = E_{\mathrm{F}} - 0.40$ eV).

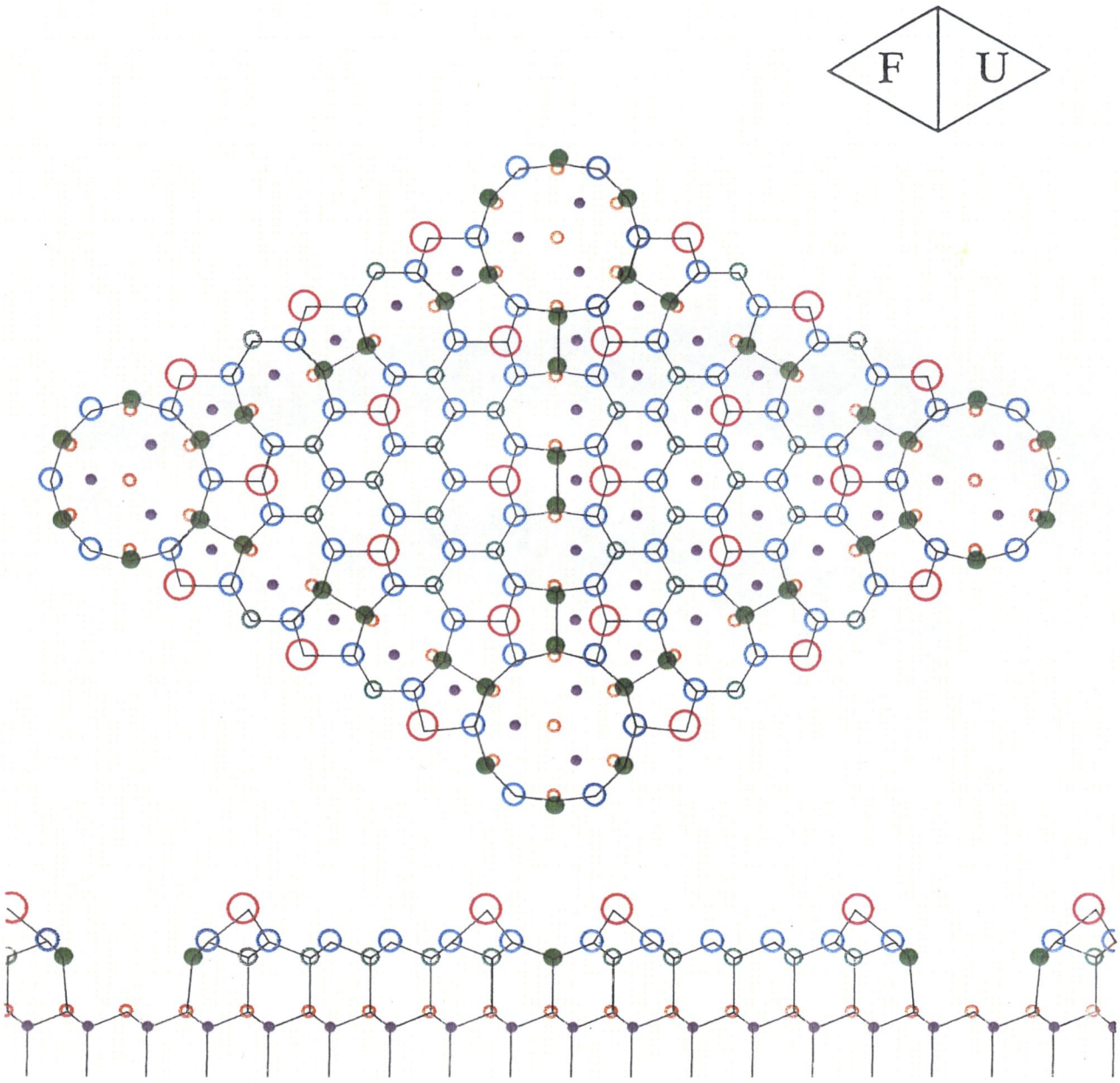

Figure 1.6: The top view (a) and the side view (b) of the DAS model of the Si(111)7×7 surface. The circles represent Si atoms, the largest ones the adatoms, the next ones those of the first layer, etc. The filled green circles are the Si atoms which form dimers. The marks F and U, in the lozenge at the upside of the figure, indicate the faulted part and unfaulted part of the unit cell, respectively.

where the first layer is replaced. The letters A, B and C indicate the three (111) layers of the face-centered cubic structure. The lateral atomic positions in B and C layers are shifted by $a/\sqrt{6}$ and $2a/\sqrt{6}$ to the $[11\bar{2}]$ direction with respect to A, respectively. A', B' and C' are the layers which are shifted by $(\frac{a}{4}\frac{a}{4}\frac{a}{4})$ from A, B and C, respectively. The interval between the layers indicated by the same letter (for example A and A') is $\sqrt{3}a/4$, and the lateral atomic positions in those layers are the same. On the boundary line of the faulted and unfaulted parts, six atoms of the second layer form three dimers, since each of them lacks one bonding partner. Their bond lengths have been determined by transmission electron diffraction (TED) [19]. The numbers of characteristic elements of the DAS model are

dimer	9
adatom	12
stacking-fault	1/2
rest atom	6
corner hole	1

per unit cell. Each adatom, rest atom and corner hole has 1 dangling bond. Hence, the number of dangling bonds per unit cell is 19. This number is much less than that (49) in the 7×7 unit cell of the hypothetical ideal 1×1 surface). This fact was a guiding principle to construct a model of stable structure.

The electronic structure of the 7×7 surface has been measured by means of ARUPS [20], UPS and IPES [21] and STM [22].The result of ARUPS measured by Yokotsuka *et al.*[20] is shown in Fig. 1.7. There are three peaks in each spectrum, whose binding energies are independent of the emission angle value. These three peaks are located at 0.2 (S_1), 0.8 (S_2) and 1.8 eV (S_3) below E_F. Himpsel *et al.*[21] performed the UPS and IPES measurements for the Si(111)7×7 clean surface and the hydrogen or oxygen adsorbed surfaces. Comparing the result of the clean and adsorbed surfaces, they concluded the peak at 0.2 eV below E_F (S_1) as the surface state, those at 0.8 (S_2) and 1.8 eV (S_3) (below E_F) as the resonance states in the bulk valence band from the UPS data. They observed one peak at 0.5 eV above E_F (U_1) in the IPES data (Fig. 1.8). Hamers *et al.*[22] reported the STM images at different voltages, that is current-image-tunneling spectroscopy (CITS) images. Figure

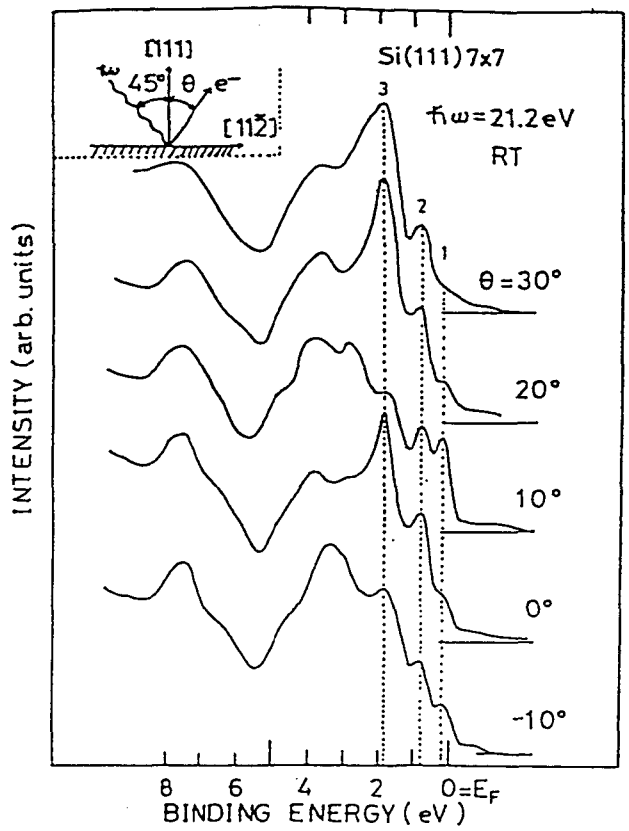

Figure 1.7: ARUPS spectra of the Si(111)7×7 surface. The inset shows the geometry of measurement. (from ref.[20])

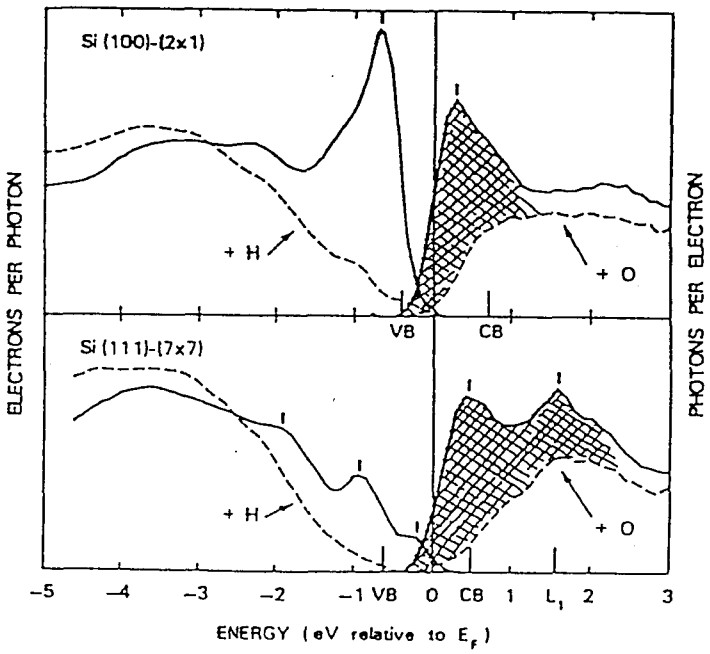

Figure 1.8: (a) The solid lines are the spectra of the Si(111)7×7 clean surface, observed using UPS and IPES. The dotted lines are those for the adsorbed surfaces for comparison. Tick marks represent the surface states. The symbols VB and CB mean the bulk band edges. (b) Spectra for the Si(100) surface is irrelevant here. (from ref.[5])

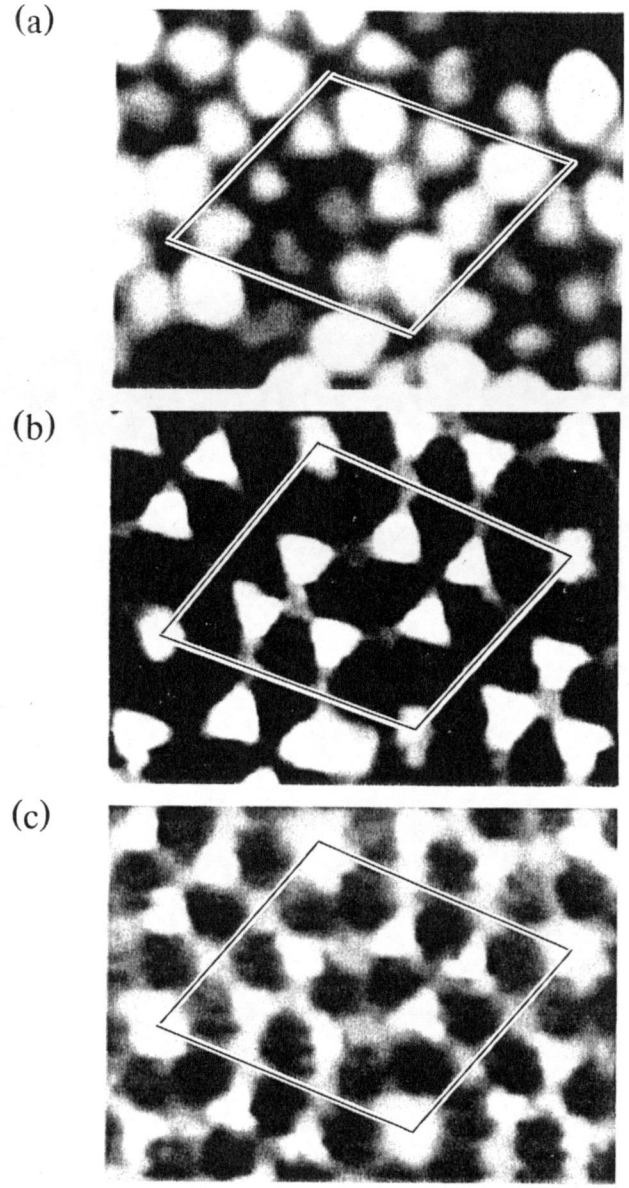

Figure 1.9: Current-image-tunneling spectroscopy (CITS) images of occupied Si(111)7×7 surface from ref.[22]. (a) Adatom state at -0.35eV, (b) dangling bond state at -0.8eV and backbond state at -1.7eV below the Fermi level. The left half of the unit cell corresponds to the unfaulted part of the DAS model.

1.9 shows the images of the surface state at (a) 0.35 eV, (b) 0.8 and (c) 1.8 below E_F. We can see the adatom surface states (S_1) in the panel (a) which have the clear intensity asymmetry between the faulted and unfaulted sites. The panel (b) shows the rest atom states (S_2) which have no asymmetry. The panel (c) shows the back-bond states (S_3). This state (S_3) probably correspond to the $3p_x$ and $3p_y$ orbitals of the adatoms, bonded to the $3p_z$ orbitals of the atoms directly below them.

1.3 Desorption Processes

When we irradiate electron or photon beams to the surface, we can observe ionic and neutral desorbing species from the surface. These desorptions are called ESD and PSD. ESD and PSD occur generally with electronic excitation at the surface, and so they are called DIET (desorption induced by electronic transitions). DIET is a useful method to study the adsorbates. That is, using these methods we can obtain information not only about the adsorbed species but also about the adsorption geometries. Moreover, the characteristic of these methods is that the damage of the surface is less than that of the thermal desorption (TD), secondary ion mass spectroscopy (SIMS) or ISS.

1.3.1 MGR model

Menzel and Gomer [23][24], and Redhead [25] have proposed independently a model for desorption process about the same time. They proposed that desorption occurs by an excitation of the electronic state, like the dissociation of molecules, that is like the excitation from the bonding-orbital state to the anti-bonding-orbital state of molecules, in the gas phase. This model is generally called MGR model, although similar idea was proposed much earlier by Ishikawa [26]-[28] who measured the desorption on H_2/Pt and H_2O/Pt surfaces. This model incorporates adiabatic approximations and a semiclassical

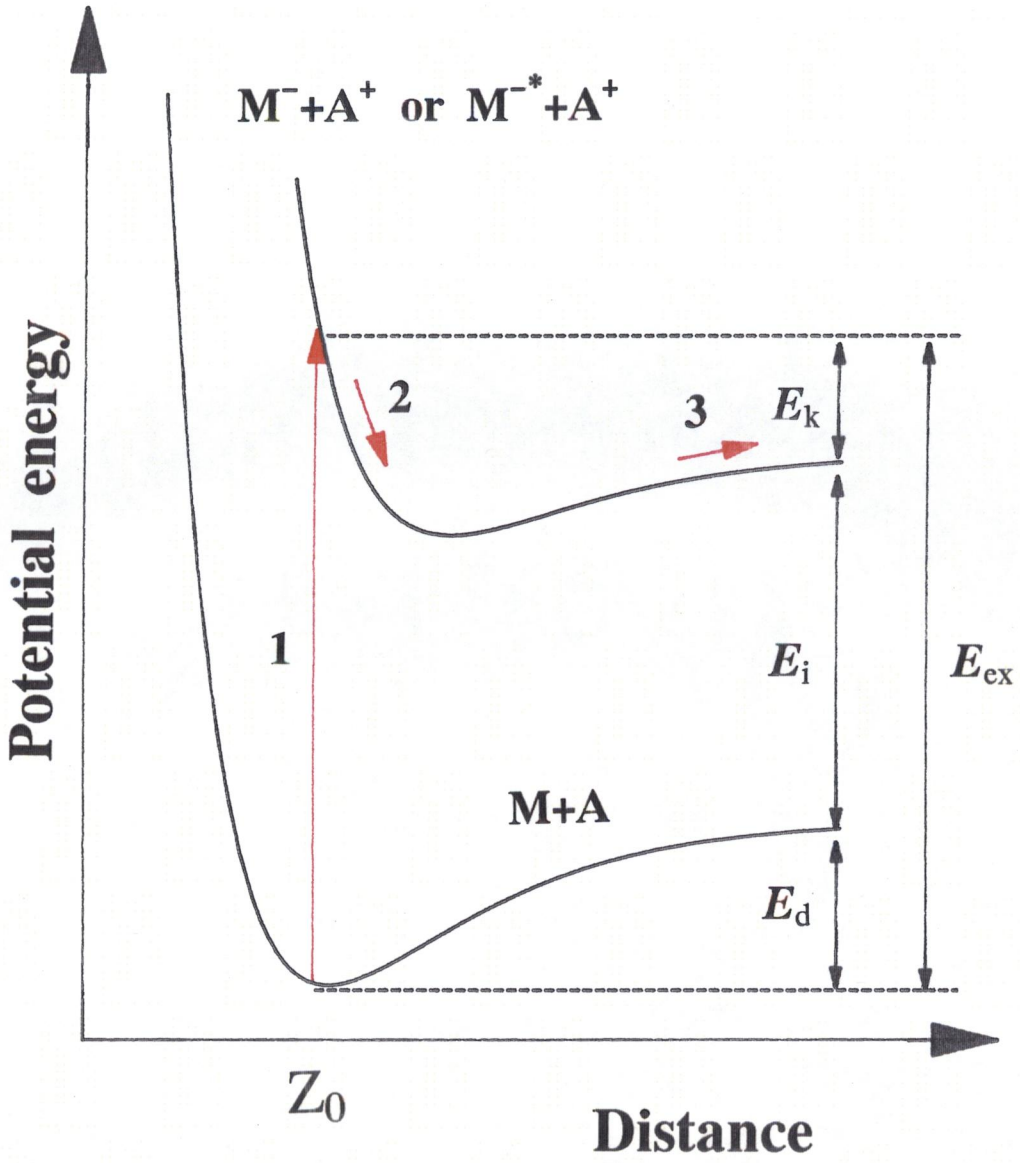

Figure 1.10: Potential diagram for adsorption. M+A and M^-+A^+ (or $M^{-*}+A^+$) represent the bonding-ground-state, the bonding-ionic-state, respectively. Z_0 is the distance of the substrate atom and the adsorbate at the bonding-state. E_k, E_i and E_d represent the kinetic energy of the desorbing ion, the ionization potential of A and the adsorption energy, respectively.

description of possible excitations of an substrate(M)−adsorbate(A) system. Figure 1.10 shows the one-dimensional potential curves which explain the mechanism of ion desorption using this model. In this model, there are three steps for the ion desorption. That is,

1. due to the stimulation by electron or photon, a Franck-Condon transition occurs and the ground-state (M+A) is excited to the ionic state (M^-+A^+). When the Franck-Condon transition is assumed, the transition is vertical and the nuclear motion is negligible during the excitation interval ($\sim 10^{-15}$ sec).

2. The ionized adsorbate (A^+) receives a repulsive force from the potential gradient and goes along the potential curve,

3. and finally desorbs.

The numbering of these processes corresponds to that of the red-line arrows in Fig. 1.10. When the adsorbate is excited and desorbs as an ion, the kinetic energy will be

$$E_{\mathrm{k}} = E_{\mathrm{ex}} - E_{\mathrm{i}} - E_{\mathrm{d}} \tag{1.1}$$

from the energy conservation law. E_{k}, E_{ex}, E_{i} and E_{d} are the kinetic energy of the desorbing ion, the excitation energy, the ionization energy of the desorbed ion and the adsorption energy, respectively. The lifetime of the excited states is much shorter than the time which is spent to desorb.The lifetime of the excited state of atoms on a metal surface is $\sim 10^{-16}$ sec and it takes $\sim 10^{-14}$ sec for an atom (H of $E_K = 1$ eV) to move 1Å. Since the relaxation processes on a metal surface are about two orders of magnitude faster, most of ions return to the ground-state and become neutral during the desorption process. Here, I described only the desorption process of positive-ion. But, considering other excited states like the the metastable state $(M+A)^*$, anti-bonding state $(M+A)^a$ or the ionic-state (M^++A^-), it is easy to find out that the desorption of neutral atom and negative-ion occur with the same process.

1.3.2 Antoniewicz model

The desorption process of chemisorbed species is explained well with the MGR model, but it was difficult to explain the desorption of adsorbed noble gases. Antoniewicz [29] has proposed a desorption model which can explain the desorption of physisorbed species. This model has a good agreement with the ESD experiments of Xe and Kr adsorbed W(110) surfaces [30][31] and Xe, Kr and Ar physisorbed Ag(111) surface [32]. In this model, the desorption of neutral atom, negative-ion and positive-ion can be explained by the excitation from the same ground-state. Here, I will explain only about the desorption of neutral atom and positive-ion.

Neutral atom desorption

The potential-energy curves to explain the desorption of neutral atom and ion are shown in Fig. 1.11. We can see three potential-energy curves in this figure. V_0, V_1 and V_2 correspond to the bonding-ground-state (M+A), bonding-ground-state of ionized adsorbate ($M+A^+$) and bonding-excited-ionic-state $(M+A^+)^*$, respectively. The desorption process of neutral atom needs two potential curves at least. This desorption process occurs with

1. the excitation from the ground-state to the ionized state of adsorbate ($V_0 \rightarrow V_1$).

2. The ion feels a screened image charge potential, which attracts it toward the surface. Considering the smaller radius of ion, Pauli repulsion is diminished as compared to the neutral atom. From these two effects, the ion moves closer to the surface along the potential curve (V_1).

3. Due to this motion, the probability of resonance tunneling or Auger neutralization by substrate electrons increases radically. Therefore, the ion becomes neutralized ($V_1 \rightarrow V_0$).

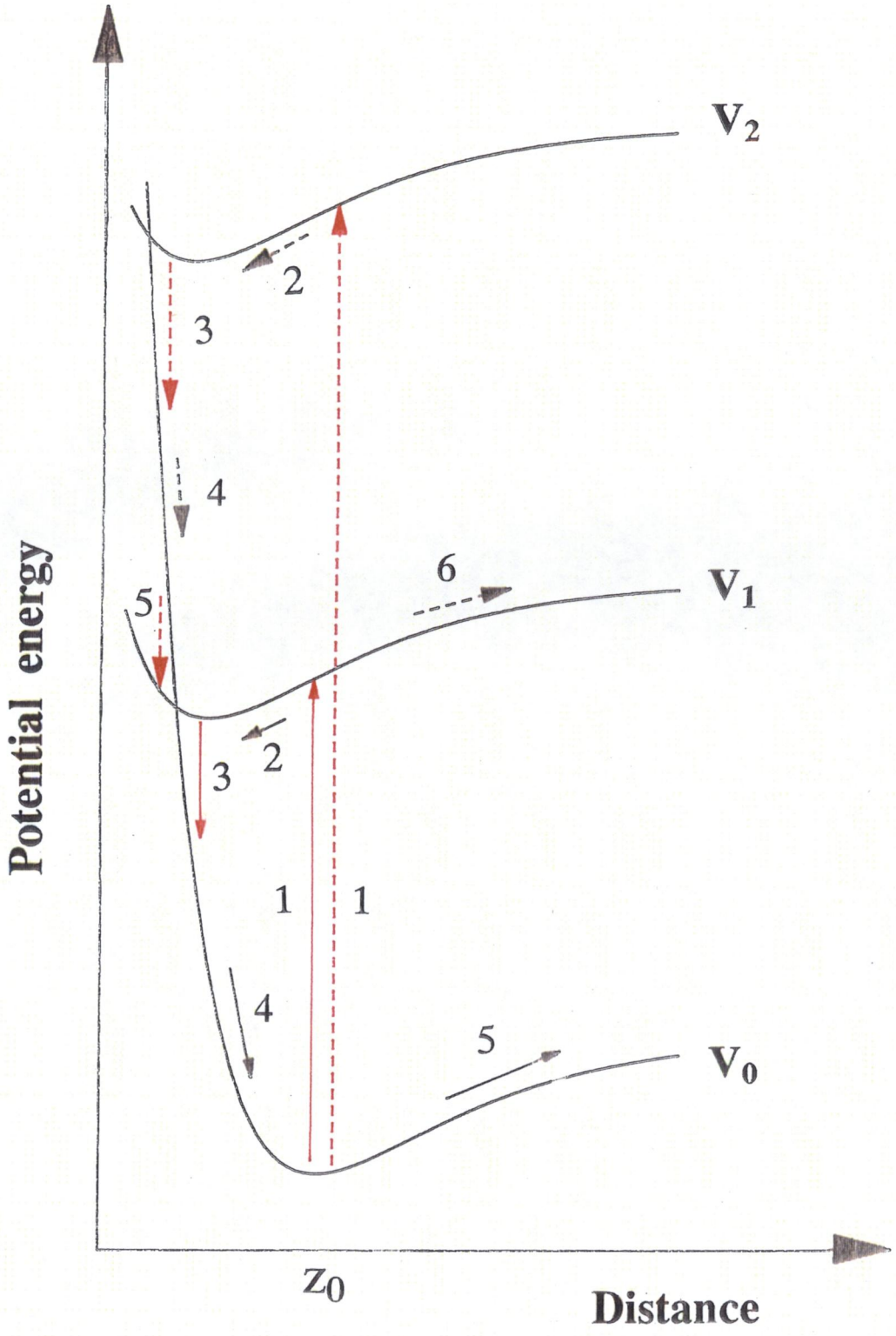

Figure 1.11: Potential-energy curve for adsorption. V_0 is the potential-energy curve for the neutral atom, V_1 for the ground-state ion and V_2 for the excited ion. The solid-line arrows and the broken-line arrows represent the desorption process of the neutral atom and ion, respectively. The red-line arrows and the black-line ones indicate the transition from one potential curve to another one and the movement of the adsorbate, respectively

4. Then, the image potential vanishes and only the Pauli repulsion remains. So, the neutral atom begins to go away from the surface,

5. and finally desorbs.

The numbering of these processes corresponds to that of the solid-line arrows in Fig. 1.11. The red-solid-line arrows represent the transition from one potential curve to another one. Other solid-line arrows represent the movements of adsorbate. The kinetic energy of the ion does not change before and after the neutralization. Therefore, the neutral atom desorbs with a kinetic energy

$$E_{\mathrm{nk}} = E_{\mathrm{nex}} - E_{\mathrm{nde}} - E_{\mathrm{na}}, \tag{1.2}$$

where E_{nk}, E_{nex}, E_{nde} and E_{na} are the kinetic energy of desorbing neutral atom, the excitation energy, the de-excitation energy and the adsorption energy of neutral atom, respectively. According to this discussion, we can understand that a neutral species is desorbed with the creation of an ion for a moment.

Positive-ion desorption

The desorption process for positive-ion is more complicated in this model, requiring at least two tunneling processes. Positive-ion desorption process occurs with

1. the excitation of the neutral atom state to the excited ionic-state ($V_0 \rightarrow V_2$).

2. The excited ion moves toward the surface, with the same reason as the second process of the neutral atom desorption.

3. Tunneling from the substrate electrons neutralizes the ion ($V_2 \rightarrow V_0$) at high part on the ground-state curve (V_0).

4. According to the Pauli repulsion, the neutral atom goes away from the surface.

5. Since the probability of electron tunneling is larger at short distance, the neutral species may be re-ionized during its escape ($V_0 \rightarrow V_1$),

6. yielding positive-ionic desorbing species.

The numbering of these processes corresponds to that of the broken-line arrows in Fig. 1.11. The transitions from one potential curve to another one and the movements of adsorbate are shown with the same way as those explained at the desorption mechanism of the neutral atom desorption. The kinetic energy of desorbed positive-ion is expressed as

$$E_{ik} = E_{iex} - E_{ide} - E_{iri} - E_i, \tag{1.3}$$

where E_{ik}, E_{iex} , E_{ide}, E_{iri} and E_{ia} are the kinetic energy of the desorbing positive-ion, the excitation energy, the de-excitation energy, the re-ionization energy and the ionization energy of desorbed ion, respectively.

I have considered only the desorption of neutral atom and positive-ion. But taking account above discussion, it is easy to understand that only adapting a suitable potential-energy curve, this model is good for neutral atom, positive and negative-ion desorptions. Therefore, we can explain neutral atom, positive and negative-ion desorptions excited from the same initial ground-state. Yu [33] have observed this phenomenon on an oxygen adsorbed Mo surface. They observed different desorbing species (O^+ and O^-) from the same site of the Mo surface. That is, they observed different desorbing species from the same initial ground-state.

Following models

Following the idea of Antoniewicz [29], some models have been developed.

Gortel have developed rigorous classical and quantum mechanical model with his colleagues [34]-[37]. They compared the experimental results and their theoretical calculations

for He and N_2O physisorbed W and Ru(001) surfaces etc. They concluded that the classical description is adequate for heavy adsorbates.

Walkup *et al.*[38] provided further analysis of the Antoniewicz motion [29] of noble-gas ions near a metal surface. Using the local density functional calculations, they showed that the attractive force on a positive-ion is substantially smaller than that calculated using the standard image potential methods.

1.3.3 KF model

Feibelman and Knotek [39] have measured the ESD of O^+ from the maximal-valency transition-metal oxides TiO_2, WO_3 and V_2O_5. They have found out that (1) the cross section for ion desorption is large, (2) the threshold energies are higher than the valence excitation region, (3) the kinetic energy of desorbing particle is high, and (4) since the oxygen atoms are adsorbed as negative-ions many charges have to move for the positive-ion desorption. The MGR model cannot explain these results. They have also found out that the threshold energy for desorption is equal to the ionization energy of core electron of the metal atom. Therefore, they proposed another model, so called KF model, for desorption.

Figure 1.12 shows the desorption mechanism of O^+ from the TiO_2 surface. On this surface, the O atoms are charged as $O^{(1+x)-}$ and the Ti atoms as $Ti^{(2+2x)+}$, where $0< x <1$. The desorption process is expressed as follows;

1. The incident electron excites the 3p core electron of the Ti atom and makes a hole.

2. One O 2p electron fills the core hole with exciting an other electron by Auger process.

3. One O 2p electron is emitted as Auger electrons.

As a result of this mechanism, O atom loses two electrons and finds itself in a O^+ state. The Ti atom remains at the same state as the initial one. Therefore, the O ion desorbs as a result of the Coulomb repulsion in addition to the Pauli repulsion.

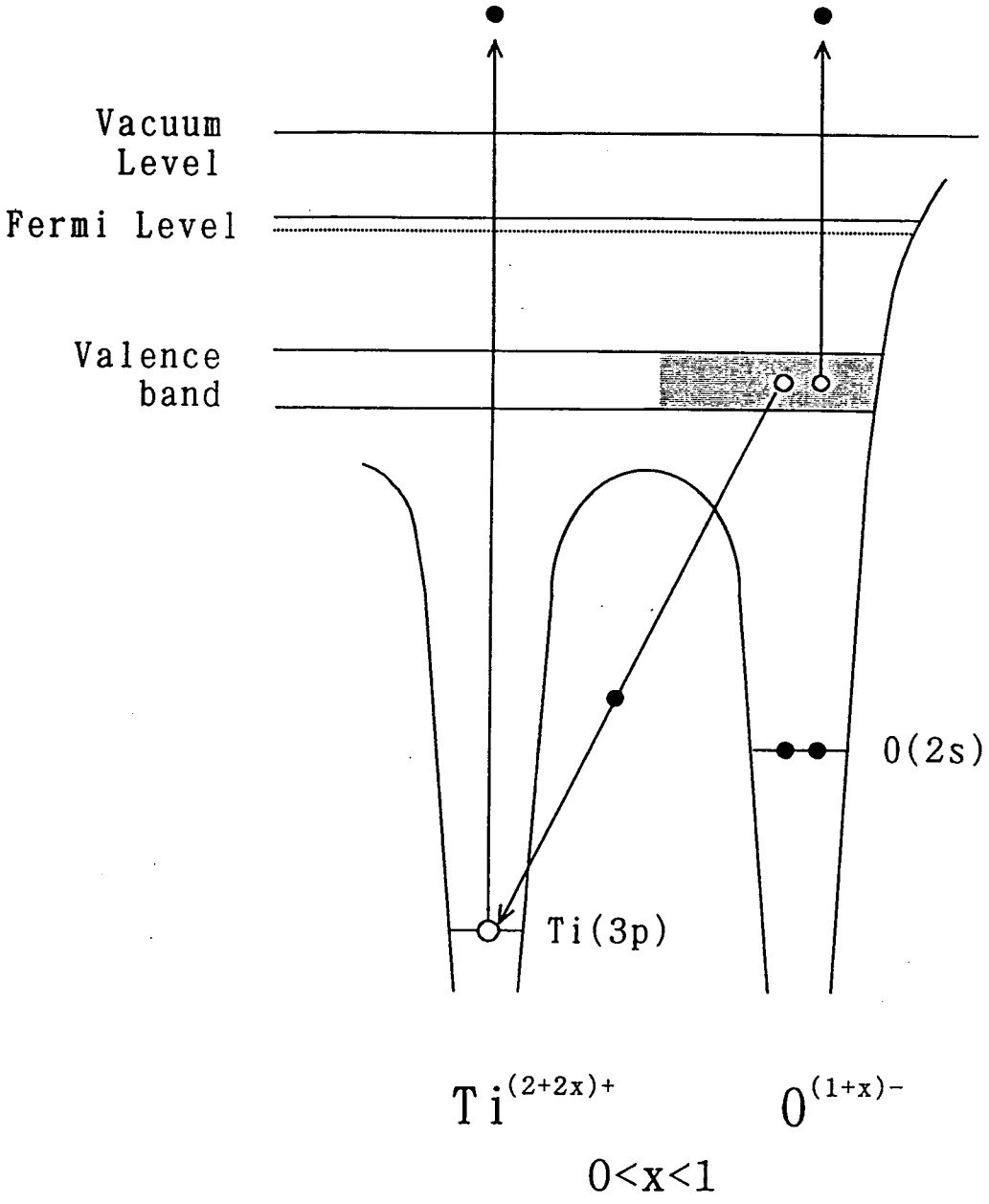

Figure 1.12: The desorption mechanism of O^+ from the TiO_2 surface. Arrows represent the transfer of electrons. Filled circles represent electrons and open circles represent holes.

In this model the desorption occurs by the inter-atomic Auger transition process, and it is necessary that the bonding between Ti and O atoms are ionic and the valence electrons of the Ti atoms are transferred to the O atoms in the initial state. That is, this ionic bonding is the origin of the Coulomb repulsion. Furthermore, the ionic bonding lowers the neutralization probability of the desorbed ions and then the desorption cross section of ions become large.

1.3.4 Other models

Francy and Menzel [40] measured the ion desorption from the CO/W(001) surface and observed the increase of CO^+ and O^+ ion yields, when the C(1s) and O(1s) cores are excited. To explain this phenomenon, they proposed a model expressed as;

1. The core holes are created.
2. Auger processes occur.
3. Multiple holes gather on the ionized atom. When two holes are localized, the lifetime of this excited state becomes long [41].
4. Localization of multiple holes in either the C−O or W−CO bond (in this case) will cause the Coulomb repulsion.
5. Ions desorb as O^+ or CO^+.

This model is named Auger Stimulated Desorption (ASD) model. In this model, the desorption occurs rapidly, and so the desorbing species should be ejected in the direction which reflects the original bonding geometry. Ramaker *et al.*[42] proposed a detailed model for ASD or Auger induced decomposition which can be applied to covalent, ionic or chemisorbed systems. The crucial features of this model are;

1. It naturally generates ions with large kinetic energies while providing relatively long lived holes in the excited state with a many body mechanism.

2. This model relates the desorption cross-section and desorbed ion energies to the electronic properties of the system.

They reported the results of decomposition cross-section for SiO_2, $LiNO_3$ and Li_2NO_4 comparing to the theoretical values.

Pooley [43]-[45] and Hersh [46] have proposed independently a similar model (PH model) for ESD and PSD from alkali-halide surfaces. In this model, the incident electron (or photon), induced on an ionic crystal at low temperature, excites an electron-hole pair in a halogen atom. Then the distance between two halogen atoms becomes short and these two halogen atoms form an excited dihalide anion. After a finite lifetime, the dihalide species dissociates, providing enough momentum to place one of its atomic constituents into an interstitial lattice site.

Irradiating X-ray to the sample, secondary electrons are plausible to excite the adsorbate. This desorption, occurring with this secondary process, is called X-ray ESD (XESD). In many cases, XESD is not the major factor causing ion desorption. But, there are several examples which have good agreement with this model. For example, the desorption of H^+ from multilayers on NH_3 on Ni(001) surface [47][48], and that of Cl^+ from Si(111)7×7-Cl surface [49] can be explained by XESD.

1.4 Principle of ESDIAD

The first observation of angular distribution in ESD experiment was done by Czyzewski *et al.*[50]. They observed sharp patterns of O^+ desorbing from the O/W(001) surface. Those patterns are related to the substrate condition. Later they suggested that these sharp patterns come from the tearing of the O−W bond and the direction of desorption relates to the bonding direction [51].

The angular distribution of desorbing ions depends on the adsorbed structure, on the

angular dependence of the neutralization probability during the desorption process and on the image force of the surface. Considering the masses of electron and the adsorbate, we can see easily that the incident direction of the electron beam is independent on the desorption direction. That is, desorption does not occur with elastic process. Now, I will discuss the three origins of the angular distribution of desorbing ions.

First, the desorption direction of desorbing ions and its extension depend on the adsorbate structure and its thermal vibration. The relation of adsorbate structure and desorption direction is shown in Fig. 1.13 . The order of the rotational and vibrational periods of adsorbates are $10^{-12\sim-13}$sec and the time required to desorb out of the surface is $10^{-14\sim-15}$sec. Therefore, the angular distribution of the desorbed ion reflects the angular distribution of the bond angle which is caused by the thermal vibrations .

Second, the direction dependence of the neutralization probability changes the angular distribution of desorbing ions. Woodruff [52][53] investigated the anisotropic neutralization using a model which estimate the isotropicall desorption from the surface. The essential feature of this model is that the ion neutralization rate is taken as

$$R = \sum_j A_j \exp(-a_j r_j) \tag{1.4}$$

with r_j the adatom to jth substrate atom distance and the constants A_j, a_j dependent only on the atomic species considered [52][53].

Finally, the image potential is an important factor which effects on the orbit. This image potential retards the z-component of the momentum of the ion. And, the range of this attractive Coulomb force is much longer than that of the repulsive force which I have discussed above. The x- and y-components of the momentum of the ion are unaffected. Therefore, the image force is anisotropic, and only the polar angle (θ) changes by this force.

Clinton [54] proposed a model for the final effect, that is the effect of the image potential. According to his model, the relation of the original desorption angle (θ_i), the final desorption

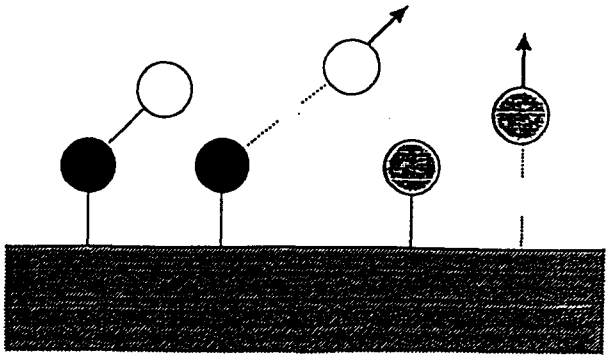

Figure 1.13: Relation of the structure of adsorbates and the desorption direction. Arrows represent the desorption direction.

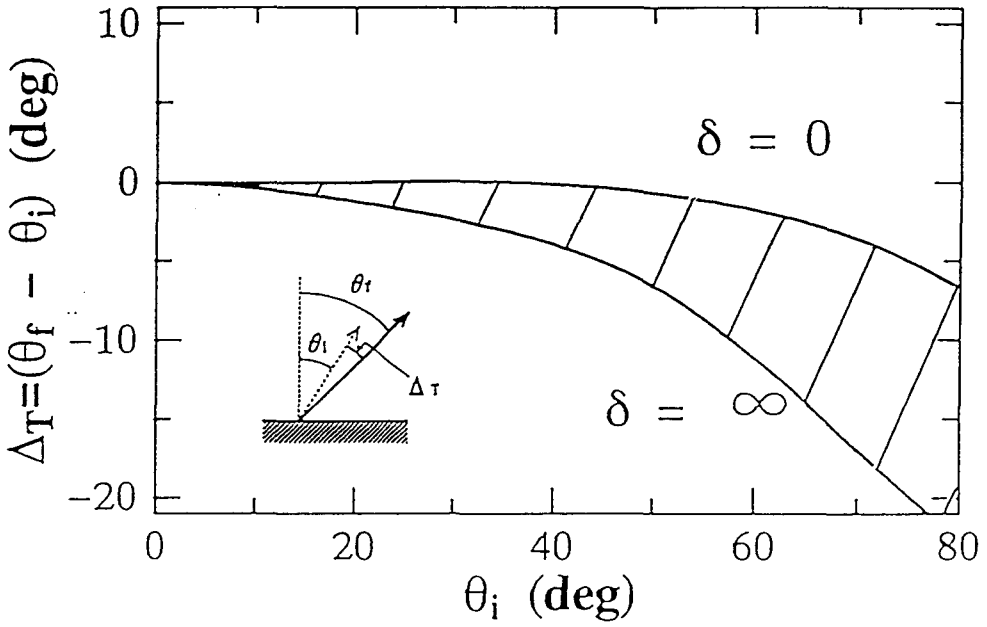

Figure 1.14: Total deviation (Δ_T) of observed ESDIAD beam location (θ_f) from the original desorption angle (θ_i). The hatched area illustrates the possible range of Δ_T as δ goes from zero to infinity.

angle (θ_f) which we can observe, and the image potential (V_i) is expressed as

$$\cos\theta_f = \{(1+\delta)[\cos\theta_i]^2 - \delta\} \quad (1.5)$$

$$\delta = |\, V_i(z_0)\,| / E_k, \quad (1.6)$$

where E_k and z_0 are the ion kinetic energy and the initial distance of the ion from the image plane, respectively. Considering eqs. (1.5) and (1.6), we can find that ions desorbing at large polar angles are deflected more than those desorbing nearly normal from the surface. Miskorić *et al.*[55] provided a similar model and have calculated the relation of the total deviation $\Delta_T = \theta_f - \theta_i$ and θ_i. This relation is shown in Fig. 1.14. We can see that Δ_T is small when we observe the ions desorbing nearly normal from the surface, and it become large at $\theta_i > 50°$. Hence, we have to correct the observed angle when we discuss the desorbing ions with large desorption angles.

According to above analysis methods, we can determine the adsorption geometry from the angular distribution of desorbing ions. There are several ESDIAD experimental equipments to measure the angular distribution of desorbing ions. For our ESDIAD experiment, we used a two-dimensional display-type spherical mirror analyzer [57]-[59], of which the detail will be explained at section 1.6 .

1.5 Principle of ARUPS

Photoelectron spectroscopy (PES) and IPES are useful methods to study the electronic properties of solids. PES is a method measuring the energy distribution of photoelectron with irradiating X-ray or vacuum-ultra-violet (VUV) light on solids. This energy distribution reflect the density of state (DOS) for XPS and UPS, so we can know the binding energy of the initial state of photoelectron. Hence, PES is a way to have knowledge about the occupied states. But we have to pay attention that the energy distribution of photoelectron for UPS reflects not only the DOS of the occupied states but also that of the

unoccupied states when the final state of photoelectron is not fixed. So, the measured energy distribution of photoelectron is not the exact DOS of the occupied states but the joint DOS (JDOS) for UPS. Measuring under a particular condition specifying the initial or the final state, we can have informations about the unoccupied states, too. IPES is a method using an inverse process of PES. That is, an electron beam is incident on the surface and electrons transfer to the unoccupied state, radiating photons. The energy distribution of these photons corresponds to that of the unoccupied state. So, we can say that it is a method to have knowledge about the unoccupied states. In this thesis, I discuss only the occupied states, and so, here I will talk only about PES. XPS and UPS are used to obtain informations about the core and valence level, respectively. As I introduced in section 1.1, we can pick up only surface sensitive informations, utilizing the photoelectron mean free path. ARUPS is a method using the energy and momentum conservation laws of the photoelectric effect of the sample. The first demonstration of band mapping using this method was published by Smith *et al.* in 1974 [56]. Now, I will explain the relation of the parallel component of the electron wave vector, the kinetic energy of the emitted electron and its emission angle. When an electron of the valence band, which has a binding energy of E_i (initial state), is excited by a photon of energy $h\nu$ to the conduction band, whose the energy is E_f (final state) above the vacuum level, and then emitted from the sample surface, its kinetic energy (E_k) should be expressed as

$$E_\mathrm{k} = E_\mathrm{f} = h\nu - \Phi - E_\mathrm{i} \tag{1.7}$$

from the energy conservation law. Here, Φ is the work function of the sample. This relation is illustrated in Fig. 1.15(a). According to this figure, it is easy to know that the intensities of the photoelectron reflect the JDOS of the sample. The relation of the kinetic energy and the wave-number vector (momentum) of the photoelectron is expressed as

$$E_\mathrm{k} = \frac{h^2\vec{k}^2}{2m(2\pi)^2}. \tag{1.8}$$

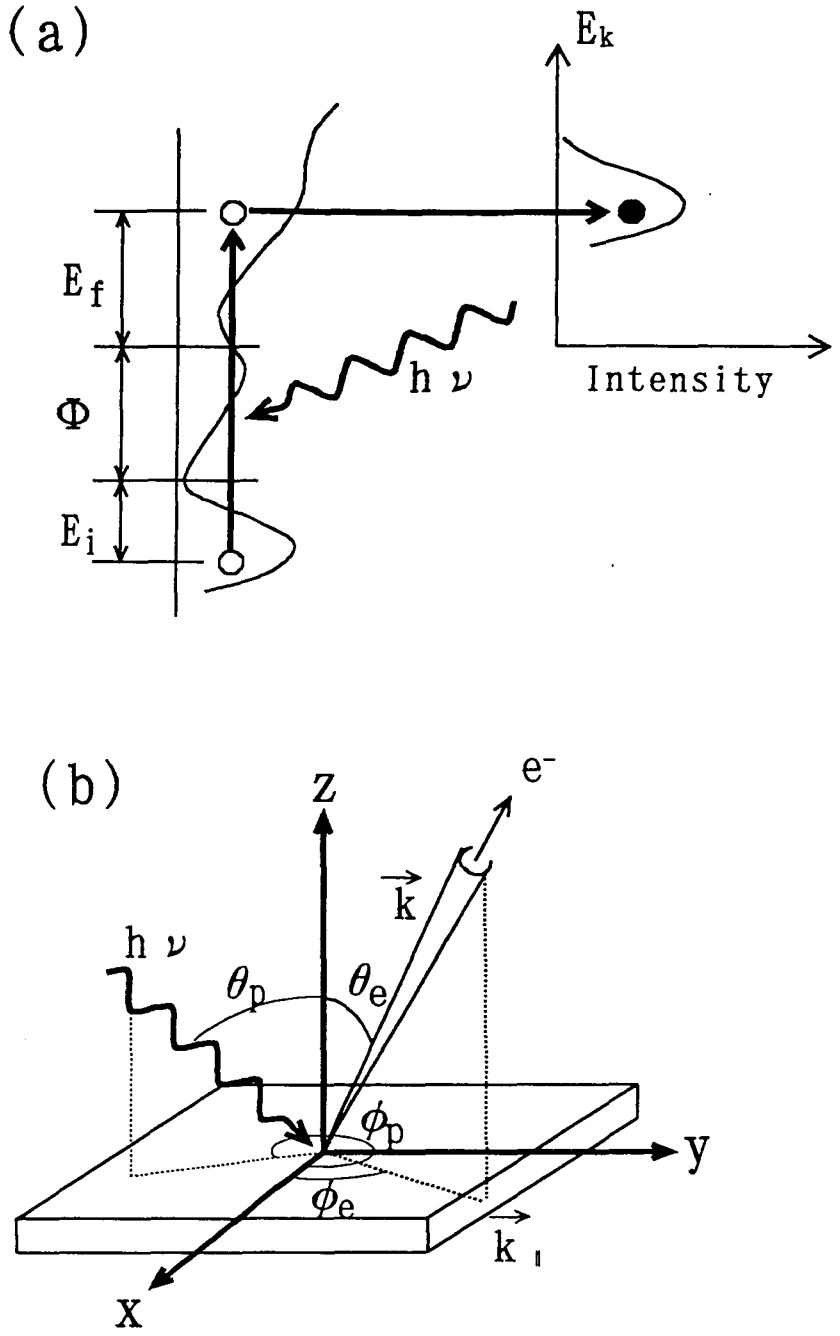

Figure 1.15: (a) The principle of the photoemission. E_i, E_f (E_k), Φ, E_F, E_V and hν represent the binding energy of the electron (initial state), the kinetic energy of the emitted electron (final state), the work function , the Fermi level and vacuum level of the sample, and the photon energy, respectively. (b) The principle of ARUPS. θ_p and ϕ_p are the azimuthal and polar angles of the photon. θ_e and ϕ_e are those of the emitted electron (photoelectron). $\vec{k}$ and $\vec{k}_{||}$ are the wave-number vector of the photoelectron and its component parallel to the surface.

The wave number of the VUV light is about 10^{-3} smaller than the lattice constant of the sample. So, the relation of the wave number vector between the initial state ($\vec{k}_{\rm i}$) and final state ($\vec{k}_{\rm f}$) will be expressed as

$$\vec{k}_{\rm f} = \vec{k}_{\rm i} + \vec{G}, \tag{1.9}$$

where $\vec{G}$ is the reciprocal lattice vector. Equation (1.7) indicates that the transition occurs at the same point of the Brillouin zone. Therefore, this transition will be a direct transition. When the final state electron is emitted from the sample to the vacuum, the component of the wave-number vector which is parallel to the surface is conservated, but that perpendicular to the surface is not conservated.

$$\begin{aligned} \vec{k}_{\rm f||} &= \vec{k}_{||}, \\ \vec{k}_{\rm f\perp} &\neq \vec{k}_{\perp} \end{aligned} \tag{1.10}$$

Considering equations (1.10) and (1.11), we can obtain that the parallel component of the wave-number vector of the initial state is equal to that of the emitted electron.

$$\vec{k}_{\rm i||} = \vec{k}_{||} \tag{1.11}$$

Therefore, the parallel component of the wave-number vector of the initial state will be expressed as

$$\vec{k}_{\rm i||} = \frac{2\pi}{h}[2mE_{\rm k}]^{1/2}\sin\theta_e \tag{1.12}$$

$$(k_x, k_y) = (k_{\rm i||}\cos\phi_e, k_{\rm i||}\sin\phi_e), \tag{1.13}$$

where θ_e and ϕ_e are the emitted angles, measured from the z-axis and xy-plane, respectively, and k_x and k_y are the x- and y-components of k_i (Fig. 1.15(b)). Hence, measuring the work function of the sample (Φ), the excitation energy (the photon energy $h\nu$), the kinetic energy of the emitted electron ($E_{\rm k}$) and its emitted angle from the normal direction (θ_e), we can obtain the binding energy (initial state energy $E_{\rm i}$) and the parallel component of the wave-number vector of the initial state ($\vec{k}_{\rm i||}$) at the same time. Moreover, considering

eqs. (1.13) and (1.14) together, we can obtain the two-dimensional band dispersion of the sample, and these equations are now the standard algorithm in the analysis of angle-resolved photoelectron data. According to Fig. 1.15(b), we can recognize that the angle θ_e determines the parallel component of the wave-number vector $k_{||}$. Therefore, we have to have to determine the direction of $\theta_e = 0.0°$ to obtain exact parallel wave-number vector. We have to fix ϕ_e carefully also to determined the crystal face and to set (k_x, k_y) to the axis of symmetry. The incidence direction of the photons is specified in Fig. 1.15(b) by the angles θ_p and ϕ_p. These angles define the polarization of the incidence beam when it is linearly polarized. The polarization is called s- and p-polarized, respectively, when the electric vector is perpendicular and parallel to the plane of incidence. Changing the polarization, we can obtain the information about the symmetry of the electron orbit.

In this thesis, I will talk about the surface state of the Si(111)3×1-K surface studied by ARUPS (chapter 4). The important point of the surface state is that the character of its structure reflects that of the surface geometric structure, in other words it has the same two-dimensional period. There are three criteria to identify the electron emission as the surface states or surface resonances.

1. The energy of the surface state lies within a band gap of the projection of the bulk band structure onto the SBZ.

2. The measured dispersion is independent of photon energy.

3. The state is sensitive to chemisorption of atoms or molecules, that is sensitive to the contamination of the surface.

But, we have to pay attention about these criteria. That is, it is difficult to determine the positions of the edge of the bulk band projection, and so when emission from the band edge can be considered as a possibility to explain a feature, neither of the criterion 1 and 2 are conclusive. The use of chemisorption systems is very valuable for the identification

of surface states and surface resonances. But, the use of the third criterion must be done with great care since also bulk features are affected by adsorption of atoms or molecules, due to increased scattering of the emitted electrons.

In this thesis, the object of study was the surface which is a two dimensional system and I used only the principle of the two-dimensional system (eq. (1.13)). But I will give a short guidance about the perpendicular component of the wave-number vector. The perpendicular component of the wave-number vector ($\vec{k}_\perp$) is obtained by considering the effect of refraction by the inner potential V_0 when the photoelectron is emitted to the vacuum. V_0 has no dependence with the photon energy $h\nu$. $\vec{k}_\perp$ will be expressed as

$$k_\perp = \frac{2\pi\sqrt{2m}}{h}[h\nu - \Phi - E_\mathrm{i} + V_0]^{1/2}\cos\theta_e. \tag{1.14}$$

So, by using the synchrotron radiation and changing the energy of the photon, we can obtain the perpendicular component of the wave-number vector. But we have to pay attention that the final state is supposed to be the plane wave in this formula.

1.6 Two-dimensional display-type spherical mirror analyzer

In this section I will explain about the two-dimensional display-type spherical mirror analyzer [57]-[59] which I used for the measurement of ESD on the O_2/Si(111) and NO/Si(111) surfaces. This analyzer was used for the time of flight (TOF), kinetic energy distribution and angular distribution measurements for desorbed ions, LEED and Auger measurements. Figure 1.16 shows the schematic cross-sectional view of this analyzer. There is a hemispherical grid made of stainless wire into the hemispherical outer-sphere made of aluminum. Both hemispheres are concentric. The sample is set inside the hemispherical grid. A small aperture is set at the symmetry point of the sample position with respect to the center. A small hole is opened in the outer-sphere at above the sample, to introduce an excitation light

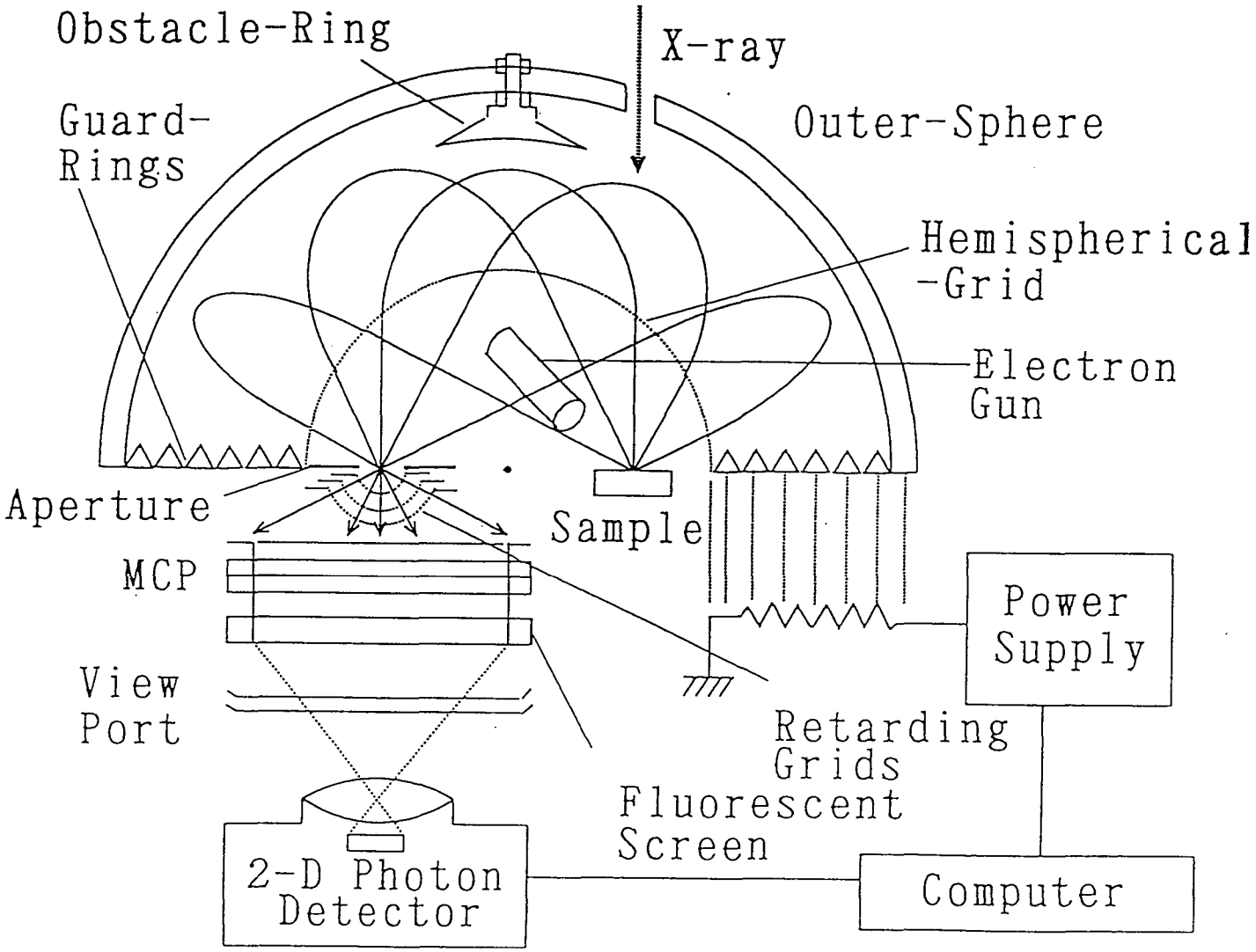

Figure 1.16: Schematic cross-sectional view of the two-dimensional display-type spherical mirror analyzer.

(synchrotron radiation, X-ray or VUV light) onto the sample. During measurements, some voltage is applied to the outer-sphere and the grid is grounded, and so there is a spherical electric field between the grid and outer-sphere, and no electric field inside the grid. In other words, there is a free space inside the grid. The guard rings are set to correct the distortion of the spherical electric field at the edge of the analyzer.

Only charged particles which are ejected from the surface by electron or light and having the kinetic energy which correspond to the potential between the grid and the outer-sphere, follow the loci drawn in Fig. 1.16 and converge to the small exit aperture. The detail will be explain at subsection 1.6.1 . The emitted angle from the sample and incident angle to the aperture of the charged particle are strictly the same. So, the two-dimensional angular distribution above the sample conserves on the fluorescent screen with no distortion. This is the main feature of this analyzer.

The features of this analyzer are summarized as follows;

1. The image has no distortion,

2. the acceptance cone is large, and

3. the structure is comparatively simple.

1.6.1 Charged particle orbit

In this subsection, I will explain the orbit of a charged particle as shown in Fig. 1.17 . The spherical grid G of radius a is grounded and the spherical electrode (outer-sphere) E of radius $2a$ is applied $-V$ (V). The central point of G and E is marked O. Now we consider the orbit of an electron P(r,θ) which is emitted from the sample (S), with an emission angle α from the OS direction. The distance of O and S is expressed as s. There is no electric field inside the grid G. Therefore, the electron moves on a beeline SL, since it is free space in this area. The electric field between G and E (region B) is a spherical electric field and

the Coulomb force is given as

$$2aV/r^2, \tag{1.15}$$

where r is the distance between P and O. Therefore, the electron feel a central force which is in inverse proportion to r^2 in this region. According to the Kepler's first law, the orbit of the charged particle is an elliptical orbit, of which O is one of the focus point, like LMN in the region B. The point M is the farthest point of this orbit from O. The elliptical orbit LMN is symmetric about the line OM. So, the incident angle (denoted by β) on the grid at the point L is equal to that at the point N . Considering the symmetry with respect to the line OM, we get that $\angle$LOM is equal to $\angle$NOM (denoted by ϵ).

Now we consider the orbit P(r,θ) in the region B. The solution of the equation of motion for the electron with a kinetic energy $E_{\rm k}$ and a velocity v is obtained by the classical mechanics as

$$r = \frac{a\eta \sin^2\beta}{1-\cos\Delta-\eta\sin\beta\sin(\Delta-\beta)} \tag{1.16}$$

$$\beta = \alpha-\theta_0 = \sin^{-1}[(s/a)\sin\alpha] \tag{1.17}$$

$$\Delta = \theta-\theta_0 \tag{1.18}$$

$$\eta = v^2/v_0^2 = E_k/E_0. \tag{1.19}$$

Here, θ_0=$\angle$SOL, E_0 is the energy of the electron which moves on a circular orbit of radius a with the velocity v_0 when the grid G is removed and the spherical Coulomb field is extend until the place where G was. If the electric field is unchanged at the outside of E like eq. (1.14), eqs. (1.15)-(1.18) are valid in this area too.

Considering that the radius of the outer-sphere E is equal to $2a$ and $E_0 = -eV$, the length of OM is expressed as

$$r_{\rm max} = \frac{a\eta \sin^2\beta}{1-\cos\epsilon-\eta\sin\beta\sin(\epsilon-\beta)} \tag{1.20}$$

$$\epsilon = \tan^{-1}\frac{\sin\beta}{\frac{(1-\eta)}{(\eta\cos\beta)}+\cos\beta}. \tag{1.21}$$

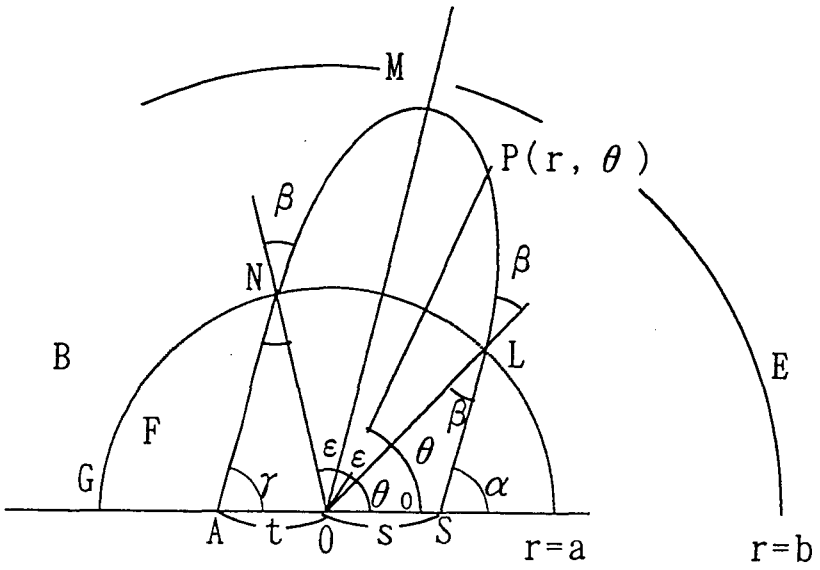

Figure 1.17: The orbit of a charged particle emitted from the sample (S). The region F inside the grid (G) is a free space. The region B between the spherical electrode (E) and G is a spherical electric field.

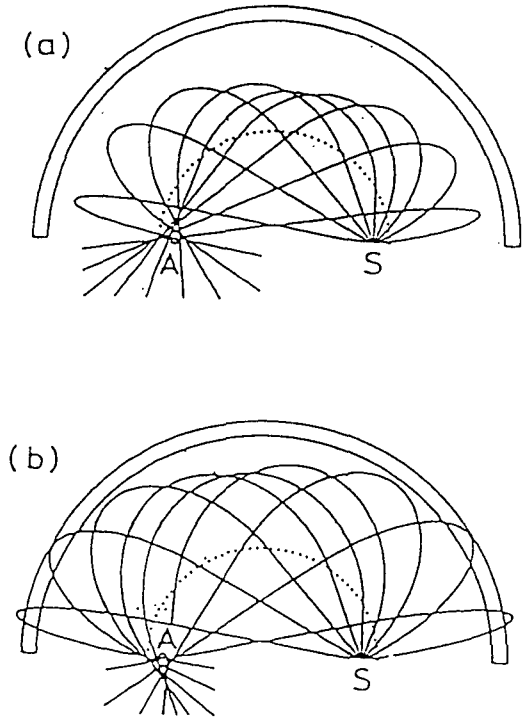

Figure 1.18: The orbits of electrons whose kinetic energies are (a) E_k=0.9E_0 and (b) E_k=1.1E_0. (from ref.[57])

After the reenter of the electron into the region F, the electron takes a beeline NT. The length of OT (denoted by t) is expressed as

$$t = \frac{s \sin\alpha}{\sin\gamma} = \frac{a \sin\beta}{\sin\gamma} \tag{1.22}$$

$$\gamma = \alpha + 2\epsilon - 2\beta \tag{1.23}$$

When $E_k = E_0$, that is η=1, equations (1.19)-(1.21) become as

$$\epsilon = \beta \quad and \quad \mathrm{SL} \parallel \mathrm{TN} \tag{1.24}$$

$$r_{max} = a(1 + \cos\beta) \tag{1.25}$$

$$t = s \tag{1.26}$$

Hence, when $E_k = E_0$, all electrons converge at the aperture T independent to the value of α.

Figure 1.18 shows the orbits of the electrons whose kinetic energies are (a) E_k=0.9E_0 and (b) E_k=1.1E_0. The orbits of neither (a) nor (b) converge at the aperture A. Now, I have explained only about the orbits of electrons, but it is easy to appreciate that the positive-ions also pass the same orbits as those of electrons when the voltage of the outer-sphere is positive.

1.6.2 Energy resolution

As I have explained in the previous subsection, charged particles whose kinetic energies are not equal the correct energy, do not focus at the aperture. The energy analysis depends on this focus-defocus effect. The obstacle ring and the set of retarding grids are added to improve the energy resolution. The obstacle ring and the retarding grids are set to cut the higher- and lower-energy particles, respectively. Their positions are already shown in Fig. 1.16.

As shown in Fig. 1.19, some higher-energy particles which are emitted nearly perpendicularly from the surface return to the aperture. According to eq. (1.24) we recognize

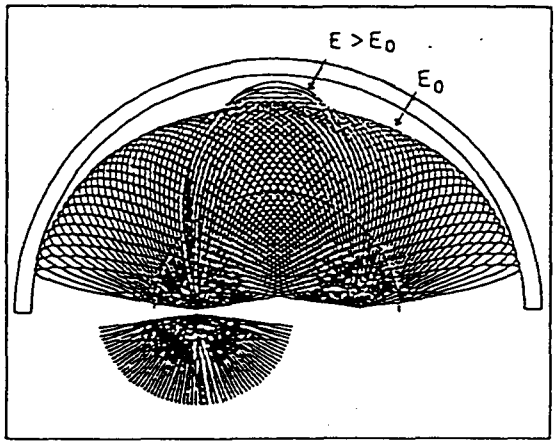

Figure 1.19: The orbits of electrons which can pass the aperture having correct energy E_0 and higher energies $E > E_0$.

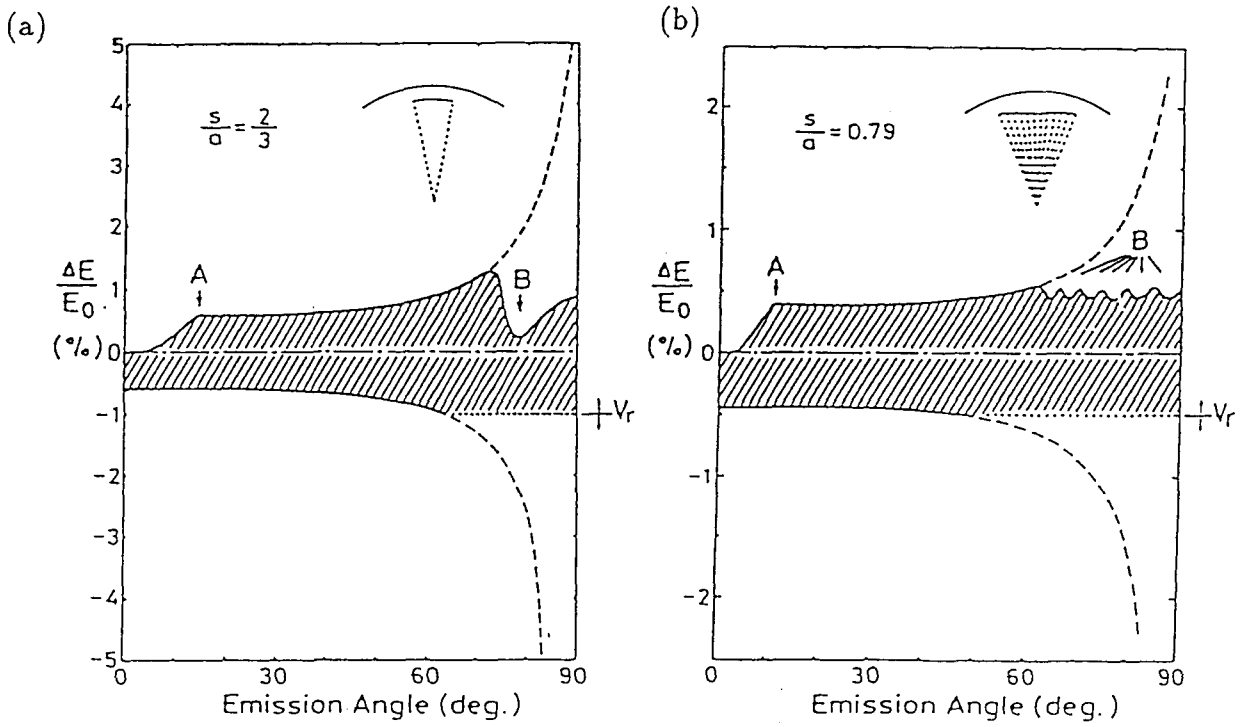

Figure 1.20: The angular dependence of the estimated resolution for (a) the "a-type" analyzer when s/a=2/3 and (b) the "b-type" analyzer when s/a=0.79. The solid and dotted lines show th resolution including the retarding grids and the obstacle ring, and the broken line shows that without them. (from ref.[59])

that the envelop surface made by all M points is not a sphere. Because the electric field act along the normal direction of the grid, the larger the emission angle is, the longer the r_{max} is. Therefore, we can cut the higher-energy particle setting an obstacle ring inside the analyzer as shown in Fig. 1.16. It is necessary to make the under surface of the obstacle ring as a part of sphere and set its voltage equal to the circumference electric potential to not distort the concentric electric field.

Figure 1.20(a) shows the angular dependence of the estimated resolution for the analyzer shown in Fig. 1.16, where s/a=2/3 and the opening angle of the obstacle ring from the central point O is about 10.9 ° and the aperture size is $0.01a$. The broken lines show the resolution without the obstacle ring and retarding grids, and the solid and dotted ones show the resolution with them. We can note that this obstacle ring can cut the tail of higher-energy particles which are emitted nearly perpendicular from the surface. But this higher-energy-cutting produces a pair of patches in the two-dimensional patterns observed at the screen. That is, the part of the pattern corresponding to the B point of Fig. 1.20(a) is darker than the other part of the screen. This is the shortcoming of this analyzer. To improve this weak point, a new-type was developed. Now, I call the analyzer before the improvement as "a-type" and that after improvement as "b-type". The schematic cross-sectional view of "b-type" analyzer is shown in Fig. 1.21. The improvement points are;

1. The sample and aperture moved closer to the edge of the grid (s/a=0.79).
2. Twelve pairs of obstacle rings are set just outside the envelop surface of the particles orbits to remove the patches and get a nearly uniform resolution all over the two-dimensional image.

From these improvement point, the energy resolution of ±0.54% is obtained. Figure 1.20(b) shows the angular dependence of the estimated resolution for the "b-type" analyzer when s/a=0.79. The meaning of the broken, solid and the dotted lines are the same as Fig.

1.20(a). We can know that the two-dimensional image become more uniform from this figure.

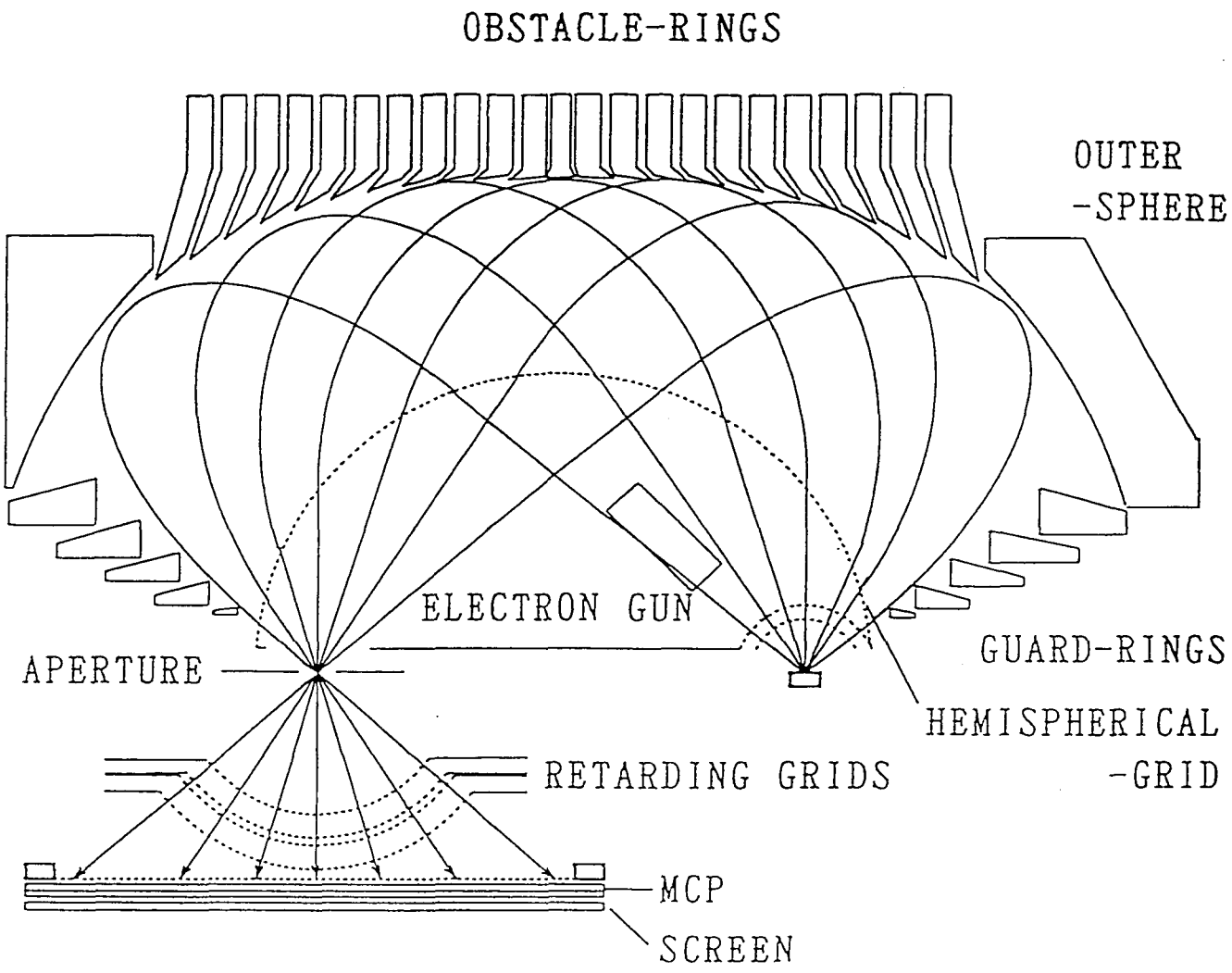

Figure 1.21: The schematic cross-sectional view of "b-type" two-dimensional display-type spherical mirror analyzer.

Chapter 2

ESD studies of the O_2/Si(111) surface

2.1 Preface

An understanding of the oxidation of Si surfaces is important from not only the scientific but also the technological viewpoint for silicon oxide. A large number of studies of the O_2/Si(111) surface have been done both experimentally [60]-[65] and theoretically [66][67]. The energy distributions and the species of desorbed ions were studied at room temperature, by means of ESD by Nishijima *et al.*[60], who reported that the species of desorbed ions were only O^+, and O_2^+ was not observed. The ion kinetic energy distribution curve of O^+, lying in a narrow energy range 3−7 eV, had a peak at about 4 eV. Edamoto *et al.*[61] and Nishijima *et al.*[62] observed the changes in EELS spectra at different oxygen exposures and temperatures (Fig. 2.1), and found that at the initial stage of O_2 adsorption, most of oxygen is dissociated and the O atoms adsorb at the on-top sites (Si−O, 96 meV, Fig. 2.2(d)) as well as at the bridge sites (Si−O−Si, 108 and 123 meV, Fig. 2.2(e)), and a small amount of molecular species also coexists (O−O, 155 meV). With the increase in coverage and by some heat treatment, the molecular species on the surface disappeared. Assuming that the energy shift is attributable predominantly to the Si−O−Si bonding angle variation and using the valence-force field model [68], they indicated that the Si−O−Si bonding angle increased towards that of vitreous SiO_2. Using XPS, Höfer *et al.*[63] found a precursor state

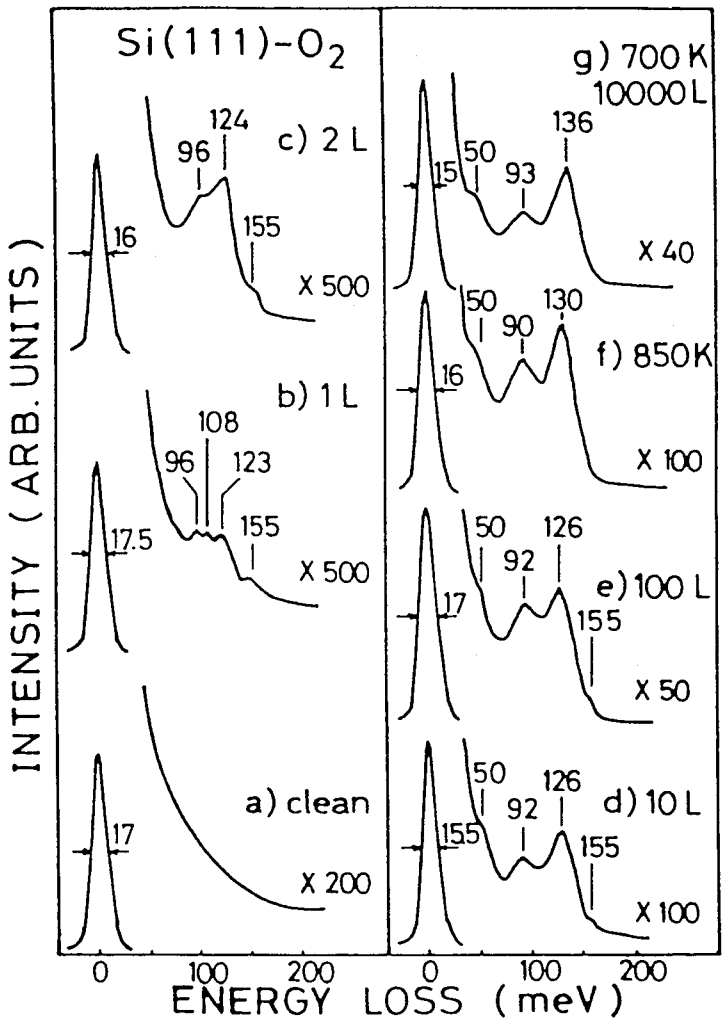

Figure 2.1: EELS spectra of (a) the Si(111)7×7 clean surface at room temperature, (b) after 1 L exposure of oxygen, (c) after 2 L exposure of oxygen, (d) after 10 L exposure of oxygen, (e) after 100 L exposure of oxygen, (f) after heating the 100 L exposed surface at 850K and (g) after 10000 L exposure of oxygen at 700K. (ref.[62])

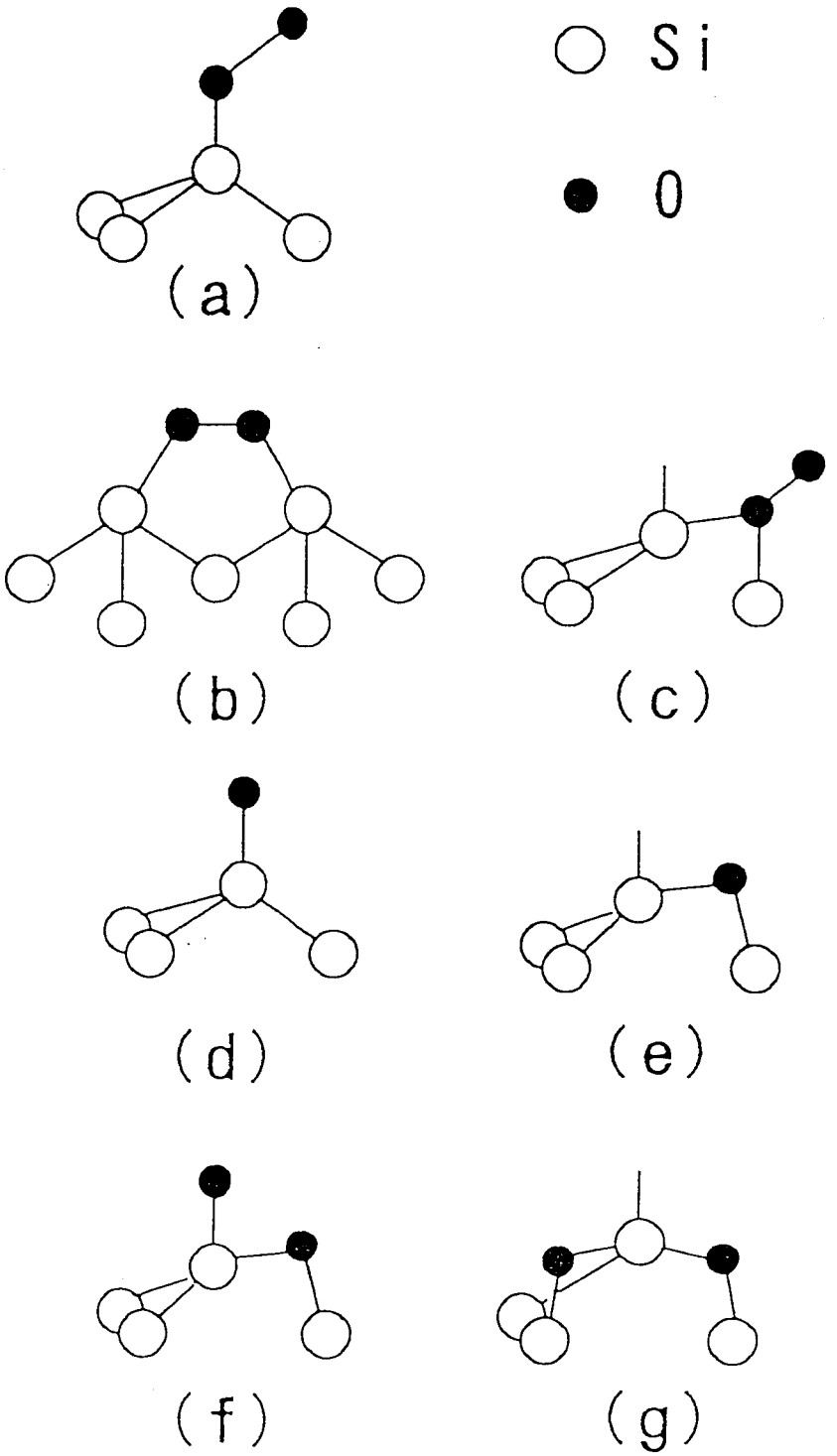

Figure 2.2: Schematic representation of the adsorption sites of molecular and atomic oxygen on the Si(111)7×7 clean surface. Open circles indicate Si atoms while closed circles indicate O atoms.

as a superoxide-like bridging molecule attached to the surface via two dangling bonds (Fig. 2.2(b)), and estimated its lifetime as 14 minutes at 300 K and 60 minutes at 150 K. The XPS spectra is shown in Fig. 2.3(a). The spectra on the right-hand side, in Fig. 2.3(a), are the results of deconvolution of the instrument function. The spectra demonstrate the decay and conversion of the precursor (peak at 530.5 eV). These precursor's intensities are plotted vs time in Fig. 2.3(b), under different conditions. Avouris *et al.*[64] observed the initial stage of oxidation using STM and UPS, and found two types of adsorption states, that is the dark and the bright site in the STM images. Figures 2.4(a), (b) and (c) show their STM image and UPS spectra, and the tight-binding calculations of the local density of states at the adatom site for various oxygen adsorption configuration which are calculated by Lyo *et al.*[69], respectively. According to their results, they proposed that the bright site of the STM image is the Si−O−Si state in which the dangling bond remains (Fig. 2.2(e)) and the dark site the state which the dangling bond reacts with the O atom (Fig. 2.2(f)). Pelz *et al.*[65] also found two types of adsorption states by means of STM, but their interpretation was different from that of Avouris *et al.* They interpreted these two states as the Si−O−Si state in Fig. 2.2(e) and the state which has a pair of Si−O−Si (Fig. 2.2(g)). Thus the initial stage of oxidation on the O_2/Si(111) surface is still a controversial problem.

Here, I report on the desorbed ion species, their kinetic energy distribution and angular distribution, when an electron beam is incident on the O_2/Si(111) surface. From the results, I comment on the above argument.

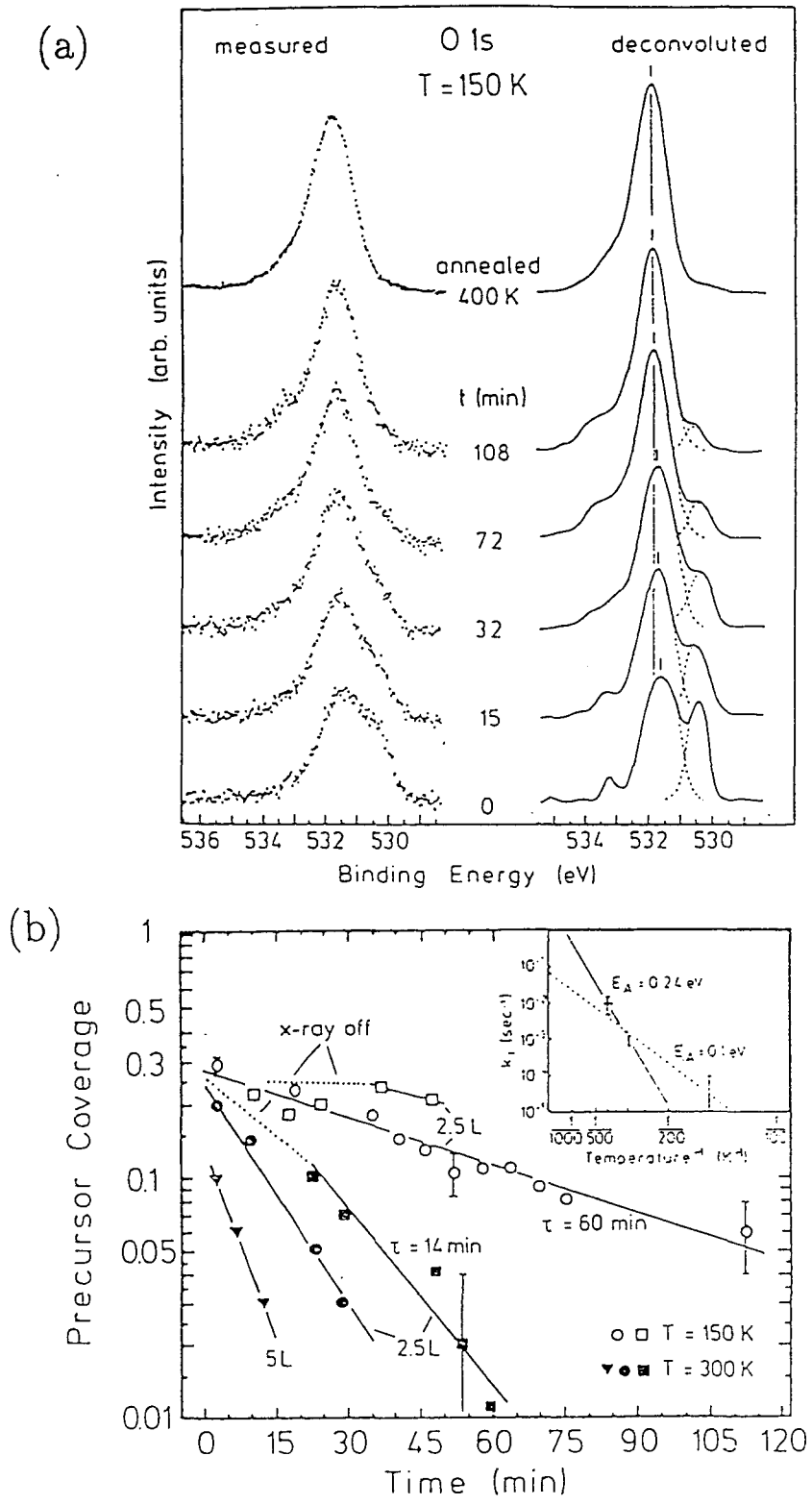

Figure 2.3: (a) O 1*s* core-level spectra of the oxygen exposed (2.5L) Si(111) surface at 150K. The spectra on the right-hand side are the results of deconvolution of the instrument function. (b) Semilogarithmic plot of relative precursor intensity vs time at 150K and 300K. The dotted line indicate the x-ray source was off. The inset shows an estimate of the thermal activation energy. (ref.[63])

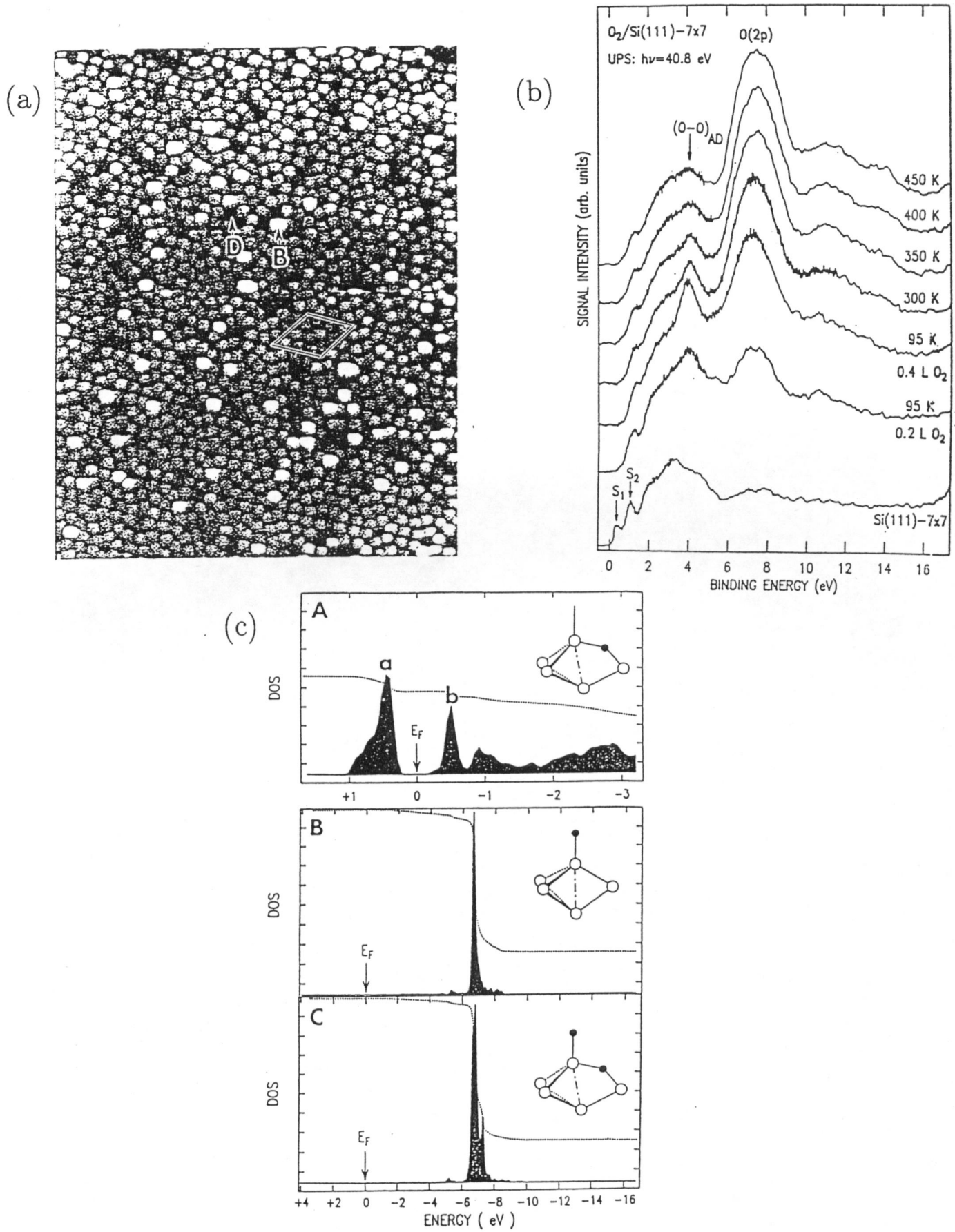

Figure 2.4: (a) The STM image of the oxygen exposed Si(111) surface and its tunneling spectra obtain over the labeled sites. (b) UPS spectra of the clean and oxygen exposed Si(111) surface. (c) Tight-binding calculations of the local density of states at the adatom adsorption configuration. The configurations are shown in the insets. (ref.[64])

2.2 Experimental

The base pressure of the experimental chamber was less than 1×10^{-10} Torr. The sample was a P-doped Si wafer with the electrical resistivity of 2.4-4.0 Ω·cm and a size of $4\times20\times0.6$ mm^3. The clean surface was obtained by direct-current heating up to ~1250°C (3 sec.×5−10 times) in the UHV chamber. The surface quality and cleanliness were checked by observing the 7×7 pattern of the LEED and by the lack of the O KLL and C KLL Auger signals.

The Si wafer was spontaneously cooled down for several minutes after flashing up to 1250°C and then exposed to O_2 gas filling the whole chamber. The pressure during the O_2 gas exposure was 1.0×10^{-8} Torr. We monitored the adsorption of the oxygen by the change in the LEED pattern.

A two-dimensional spherical mirror analyzer [57]-[59], which is already explained at section 1.6, was used for all measurements such as the kinetic energy distribution, time-of-flight spectra (TOF) for the mass analysis and the ESDIAD of the desorbed ions as well as LEED and Auger observations. The schematic diagram of the equipments are shown in Fig. 2.5. The incident electron energy and the sample bias were set to 350 eV and +15 V when we measured the kinetic energy distribution and the TOF spectra. In the TOF measurement, the pulse width of the incident electron was 400 nsec, the current was ~1 μA and the pulse frequency was ~1000 pulses/sec. The acceptance cone of the analyzer for ESDIAD was ±50 ° from the surface normal. These measurements were made at 1−4 L exposure of O_2 at room temperature.

2.3 Results and discussion

The TOF spectra of the desorbed ions with kinetic energies of 2 and 4 eV, are shown in Figs. 2.6(a) and (b), respectively, for the O_2/Si(111) surface with an oxygen exposure of

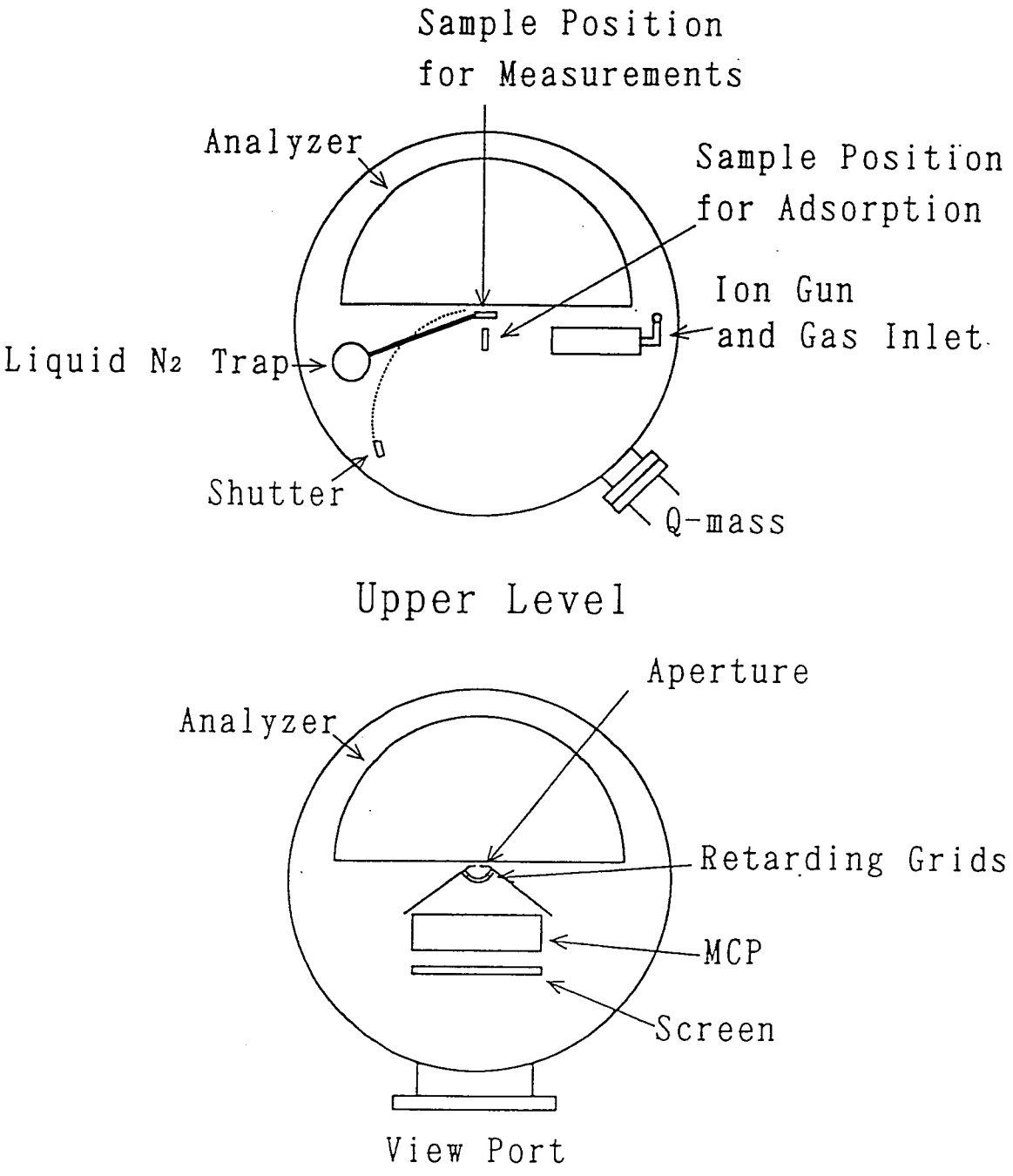

Figure 2.5: Schematic diagram of the equipments. The sample, the gas inlet and the quadruple mass analyzer are installed at the upper level. At the lower level, there are the micro-channel-plate and the fluorescence plate.

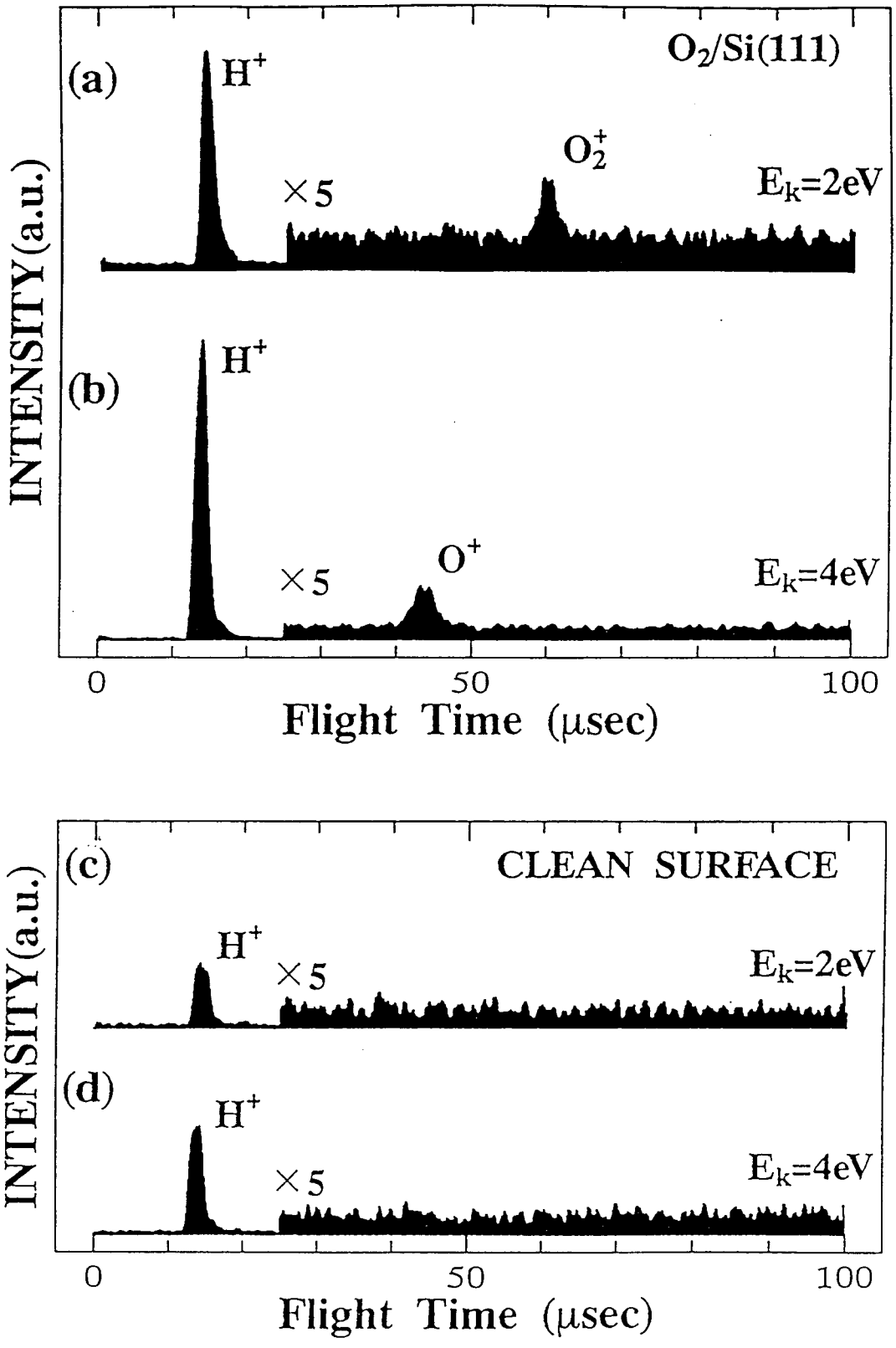

Figure 2.6: Time-of-flight spectra of the O_2/Si(111) surface ((a) and (b)) and the Si(111)7×7 clean surface ((c) and (d)).

1L . The kinetic energies of the ions in each spectrum were originally 2 eV and 4 eV but the sample bias voltage (+15 V) accelerated them to 17 eV and 19 eV, respectively. Figures 2.6(c) and (d) show the corresponding spectra on the Si(111)7×7 clean surface. Three peaks can be observed in Figs. 2.6(a) and (b), corresponding to H^+, O^+ and O_2^+. This result for desorbed ion species is different from that of Nishijima *et al.*[60], who observed only O^+. The discrepancy can be understood from the difference in the O_2 exposures: the exposure O_2 in their experiment was higher than ours making the molecular surface species no more appreciable. The peak of H^+ was also observed on the Si(111)7×7 clean surface, which showed no other structure than H^+. In Figs. 2.6(a) and (b), the intensity of H^+ is much larger than other peaks. But, this intensity ratio does not represent the coverage ratio because the desorption probability of H^+ is considered to be much higher than those of O^+ or O_2^+. H^+ can be observed even on the clean surface at 10^{-11} Torr range, which is a condition that the coverage of H is less than about 10^{-3} monolayer (ML). Though not clear at present, the origin of H^+ is supposed to be due to the movement of the H atoms to the surface which were contained in the Si wafer [70] or due to the adsorption of the residual H_2O or H_2 gas in the UHV chamber onto the Si surface. In the adsorption experiment of H_2O, H^+ was strongly observed but O^+ was not detected. Judging from the above results, we conclude that the O^+ and O_2^+ ions are generated by the O_2 adsorption and not by the H_2O adsorption, and that the H^+ is generated by a small amount (less than 10^{-2} ML) of H_2O which may be the impurity of the O_2 gas or from the replacement of O_2 and H_2O at the UHV chamber wall.

The kinetic energy distributions of total desorbed ions (H^+, O^+ and O_2^+) are summarized in Fig. 2.7 (clean surface and oxygen exposures of 1 and 300 L). The threshold of the kinetic energy distribution stays at around 0 eV for any exposure. This result is different from that for NO/Si(111) [71] (chapter 3), in which the threshold stays at about -1.0 eV (not only for the exposure of 300 L at room temperature where no molecular NO exists, but also for

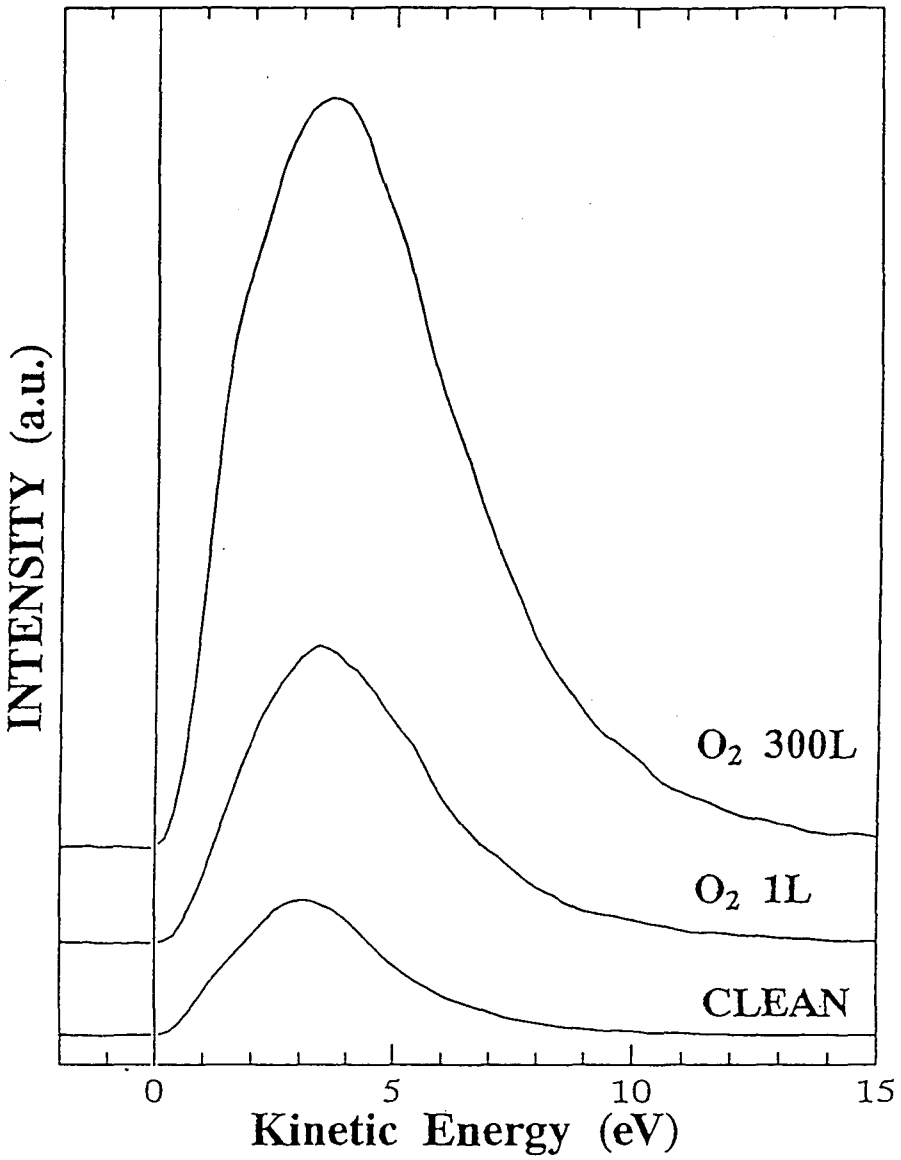

Figure 2.7: Kinetic energy distributions of desorbed ions for the Si(111)7×7 clean surface and O_2 exposed surface for 1 L and 300 L.

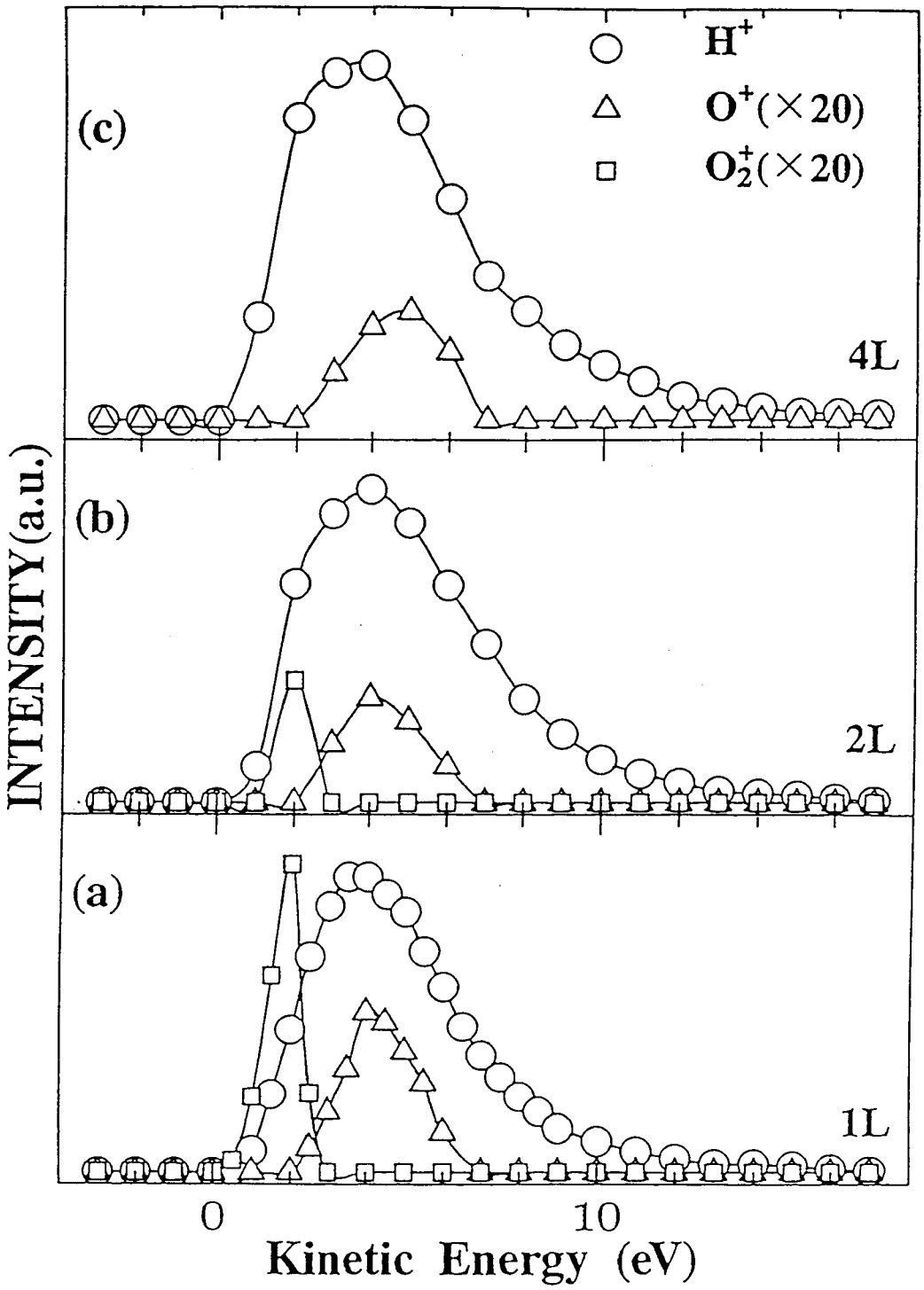

Figure 2.8: Kinetic energy distributions of desorbed H^+, O^+ and O_2^+ at 1 L (a), 2 L (b) and 4 L (c) O_2 exposures.

the exposure of 3 L at 190 K where molecular NO does exist). The result of NO/Si(111) surface will be shown in chapter 3. The negative kinetic energy is caused by the definition of zero kinetic energy at the vacuum level of the analyzer and not of that of the sample. This difference may be caused by the different degrees of reduction of the barrier height of the potential-energy curves in the ion desorption process, induced by the difference of the surface dipole moments [72]. That is, the barrier height becomes 1 eV lower during the desorption process of NO adsorbed surface, but scarcely changes at the O_2/Si(111) surface. This means that the negative surface dipole moment induced by the adsorption of oxygen on Si(111) is small compared with that of NO.

Taking into account the intensity ratio of the peaks in the TOF spectra, we can obtain the kinetic energy distribution of each ion. Figures 2.8(a), (b) and (c) show the kinetic energy distributions of the desorbed ions of O_2 exposures at 1, 2 and 4 L, respectively. The LEED patterns remained almost 7×7 at 1 L, but only the 1×1 spots were observed at 4 L. We could see desorbed O_2^+ ions at 1 and 2 L, but O_2^+ became unobservable for exposures above 3 L. We therefore conclude that the molecular surface species dissociate at high exposures. In spite of the increase in exposure, the quantity of the desorbed O^+ did not increase. It can be imagined that the O^+ can desorb less easily from the bridge site if the Si−O−Si bonding angle becomes larger. The kinetic energy distribution of H^+ has a peak at 4 eV with a halfwidth of about 4.0 eV and that of O^+ has a peak at 4 eV with a halfwidth of about 3.0 eV. These results are very similar to those of Nishijima *et al.*[60]. The kinetic energy distribution of O_2^+ has been observed for the first time; it has a narrow peak at 2 eV with a halfwidth of about 1.0 eV, which is quite different from that of other desorbed ions.

Figures 2.9 (a)-(c) show the angular distribution patterns of desorbed ions. The pattern of O_2^+ at the kinetic energy of 2 eV for an exposure of 1 L is shown in Fig. 2.9(a). Figures 2.9(b) and (c) show the patterns of O^+ at 4 eV for the exposure of 1 L (b) and 4 L (c),

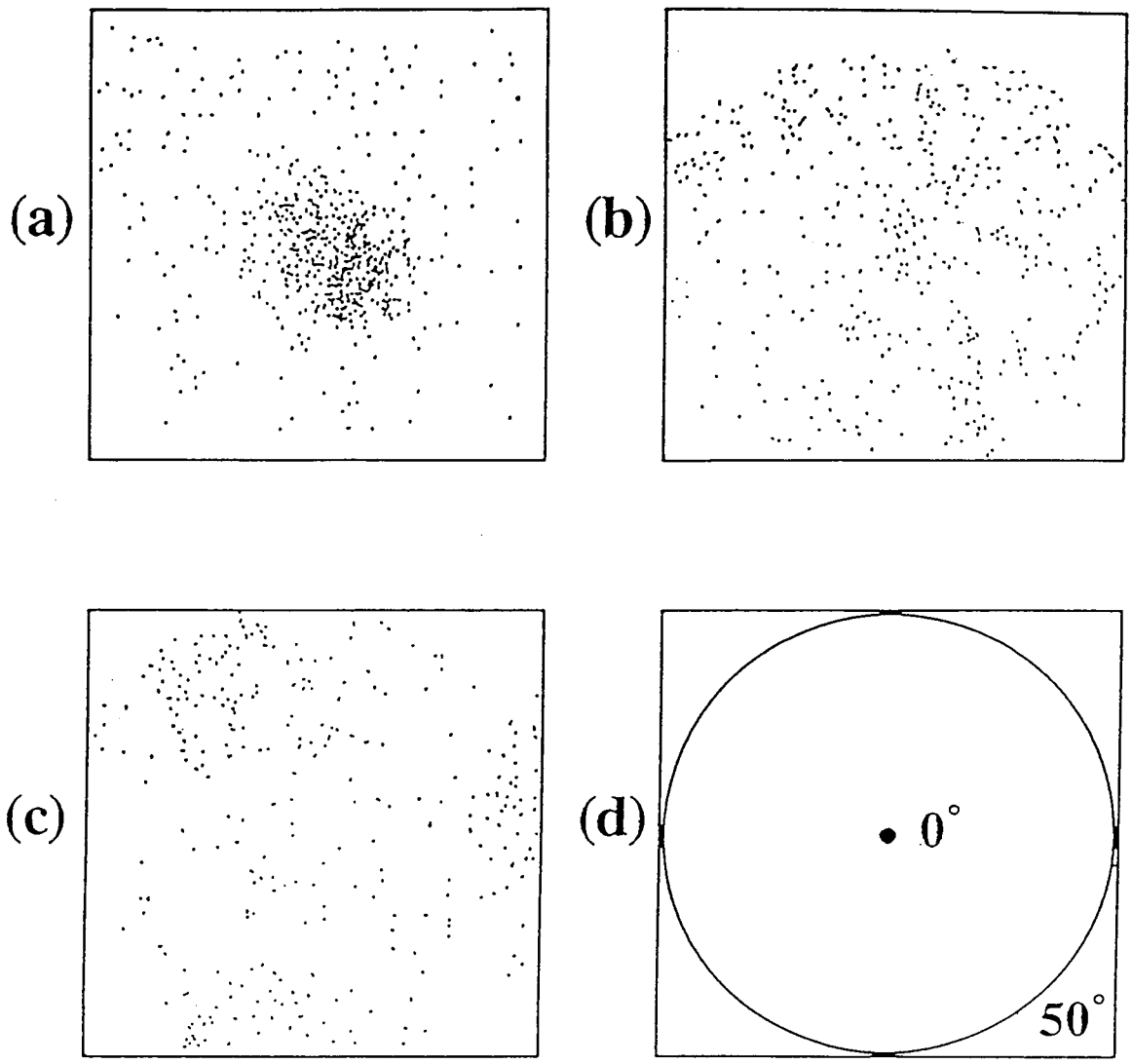

Figure 2.9: Angular distribution patterns of (a) O_2^+ at the kinetic energy of 2 eV for the exposure of 1 L and O^+ at 4 eV for the exposure of (b) 1 and (c) 4 L. The corresponding polar angles are shown in (d) (the surface normal is taken to be 0°).

respectively. The pattern of O_2^+ (Fig. 2.9(a)) is concentrated near the center of the screen, which corresponds to the surface normal direction. In the pattern of O^+, the intensity at the center is slightly stronger for low exposures (Fig. 2.9(b)) but that at the circumference of the screen becomes stronger for high exposures (Fig. 2.9(c)). It is generally thought that the angular distribution approximately represents the bonding direction of the desorbed species. So, the molecular O_2 is considered to be adsorbed at the on-top site and not at the bridge site (Fig. 2.2(c)). On the contrary, the dissociated O atoms are thought to be adsorbed both at the bridge site and at the on-top site for low exposures, but adsorbed mostly at the bridge site for high exposures. We consider that the adsorption site of the molecular surface species observed in this experiment will be as shown in Fig. 2.2(a) and (b). The adsorption site of the dissociated oxygen is considered to be as shown in Fig. 2.2(d) and (e), and or (f) for low exposures and Fig. 2.2(e) and (g) for high exposures, judging from the angular distribution pattern of O^+ and the results of EELS [61].

The lifetimes of the molecular surface species have been discussed only in terms of the superoxolike bridging molecule (Fig. 2.2(b)) by Höfer *et al.*[63]. The relation of the intensity of the O_2^+ peak and the time after oxygen adsorption at room temperature is shown in Fig. 2.1, in a semilogarithmic plot for exposures of 1 L (filled circles) and 2 L (crossed points). Within experimental accuracy, each data set lies on a straight line, indicating the exponential decay of one molecular surface species. The lifetimes estimated for these lines are about 8 hours for 1 L and 2.5 hours for 2 L. Since the lifetime of the species of Fig. 2.2(b) has been reported to be 14 min [63], the molecular surface species observed in our ESDIAD is not the one of Fig. 2.2(b) but another species like that of Fig. 2.2(a).

From the temperature dependence of the rate constant k_T, which is the inverse of the lifetime, we can estimate the thermal activation energy (E) with the relation $k_T = k_0 exp(-E/k_B T)$. The rate constants k_T for 300, 420 and 470K are shown in the inset of Fig. 2.10 for 1 L exposure. The fitted line gives E = 0.55 eV and k_0=5.5×10^4 sec^{-1}.

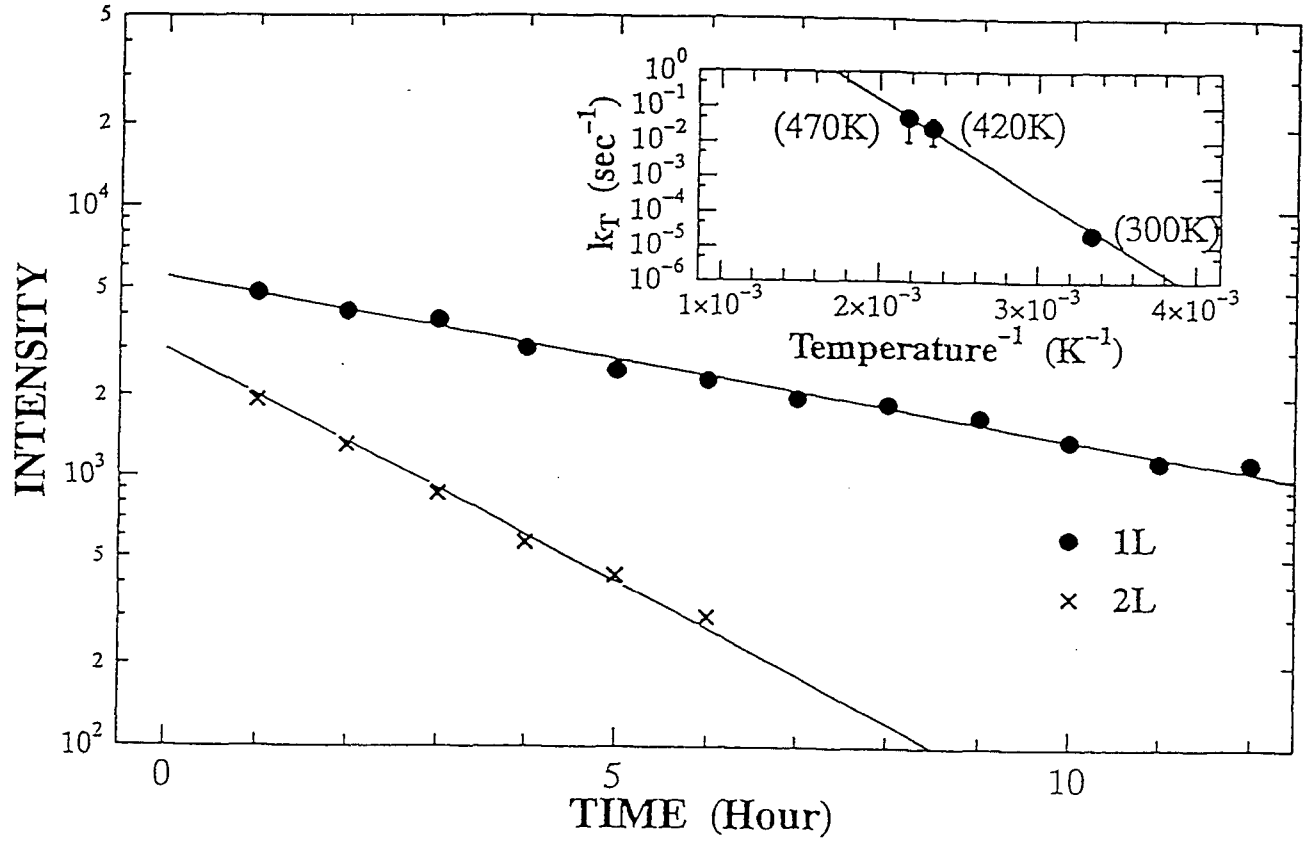

Figure 2.10: Semilogarithmic plot of the TOF intensity of O_2^+ versus the time at 1 L (filled circles) and 2 L (crossed points). The solid line is a fitted line of $y = y_0 exp(-x/\tau)$, where y_0 is the intensity at 0 hour and τ is the lifetime of the molecular surface species. The inset shows the temperature dependence of k_T for the estimation of the thermal activation energy.

We note that this value of E =0.55 eV is quite different from the value of 0.24 eV reported by Höfer *et al.*[63]. Since the peak of O_2^+ to 2 L exposure was too weak for high temperature, we cannot discuss either the rate constant or the activation energy for this coverage. The difference in the lifetimes for different coverages was also reported by Höfer *et al.*[63]. Although our experimental conditions were somewhat different (we could not observe the desorbed O_2^+ species soon after the adsorption because of the electric discharge of the micro-channel plate), we can say that we have observed another species than that of Höfer *et al.*[63]. Hence, there may be two types of molecular surface species like those shown in Figs. 2.2(a) and (b) on the Si(111) surface, which have different lifetimes. The reason why we could not detect two types of molecular surface species is considered to be the experimental problem described above. To discuss the desorption of species reported by Höfer *et al.*[63], we require a long lifetimes, but unfortunately it was impossible with our experimental setup to cool down the sample to low enough temperatures to obtain long lifetimes.

2.4 Summary

The adsorption states of the O_2/Si(111) surface were studied at room temperature by means of ESD. For low exposures (< 2 L), we observed H^+, O^+ and O_2^+ as desorbed ion species. At high exposures (> 4 L), we observed only H^+ and O^+. We found that O_2^+ is observable at low exposure in the ESD experiments. The peaks of the kinetic energy distribution of the desorbed ions, H^+, O^+ and O_2^+, were observed at 4.0, 4.0 and 2.0 eV, respectively. For O^+, the position of the peak in the kinetic energy distribution and its halfwidth were almost the same as those reported by Nishijima *et al.*[60]. From these results, it is concluded that the oxygen adsorbs only dissociatively under high exposures. As for the O^+ desorption, it is found that the angular distribution changes with increas-

ing coverage. Under low exposure, the angular distribution is rather uniform whereas the pattern becomes relatively stronger at the circumference with increasing the coverage. It was also found that the intensity of the O^+ signal did not increase in proportion to the coverage; that is, the adsorbed atomic oxygen can less easily desorbs from the surface at high coverage. From these results and those of EELS [61], we propose that the adsorption site of the molecular surface species is that shown in Fig. 2.2(a), and the adsorption site of the dissociated oxygen is represented by the models in Figs. 2.2(d) and (e), or (f) for low exposures, and in Figs. 2.2(e) and (g) for high exposures, with the angle of Si−O−Si larger at high exposures. With the results of the time dependence of the TOF spectra, we estimated the lifetime of the Fig. 2.2(a)-type molecular surface species as about 8 hours for 1 L and 2.5 hours for 2 L. From the temperature dependence of the lifetimes, the thermal activation energy of the Fig. 2.2(a)-type molecular surface species was estimated to be 0.55 eV.

Chapter 3

ESD and PSD studies of the NO/Si(111) surface

3.1 Preface

The study of reactions of nitric oxide on solid surfaces is interesting from both technological and scientific points of view. From the technological view point, NO is one of the harmful combustion exhaust gases. So it is desirable to find efficient catalysis and methods to convert NO into harmless gases. From the scientific view point, NO molecule is very interesting because it has one unpaired electron in the antibonding ($2\pi^*$) orbital. Many studies of NO/Si(111) surface have been done by means of EELS [62][73][74], UPS [75], ESD [60], PSD [76], TPD [74] and thermal nitridation [77][78]. Ying *et al.*[74] suggested that NO adsorbs on Si(111)7×7 at 90 K as physisorbed N_2O as well as chemisorbed NO molecules at the bridge and on-top sites. Figure 3.1(A) shows their HREELS spectra measured at different exposures of NO. The peaks at 57 and 65 meV indicate the vibrational modes of NO−Si of the on-top and the bridge sites NO, and those at 187 and 225 meV indicate the vibrational modes of the N−O of the NO adsorbed at the bridge and on-top sites, respectively. The peaks observed at 155 and 276 meV indicate the existence of N_2O since they correspond to the vibrational modes of N−O and N−N in N_2O, respectively. Figures 3.1(B) and (C) show the TD spectra for saturation exposure of NO on Si(111)7×7 surface, and the HREELS spectra at different temperatures. We can see two peaks (110

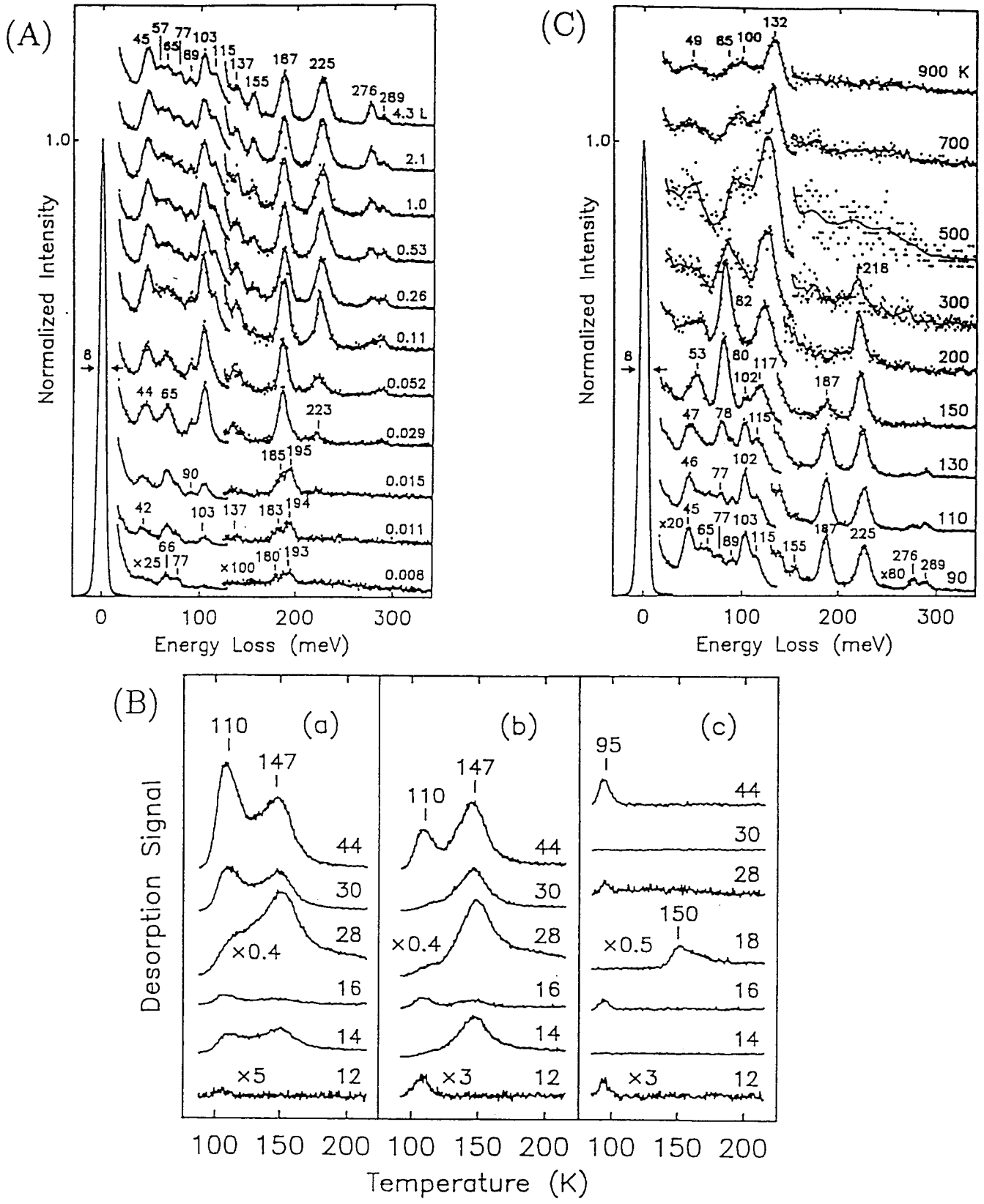

Figure 3.1: (A): A series of HREELS spectra for various exposures of NO on Si(111)7×7 surface. (B): TD spectra for saturation coverage of NO on Si(111)7×7 surface. (a) without preheating, (b) after flashing at 130 K and (c) 900 K. (C): HREELS spectra recorded at 90 K after the surface has been flashed to various elevated temperature. (from ref.[73])

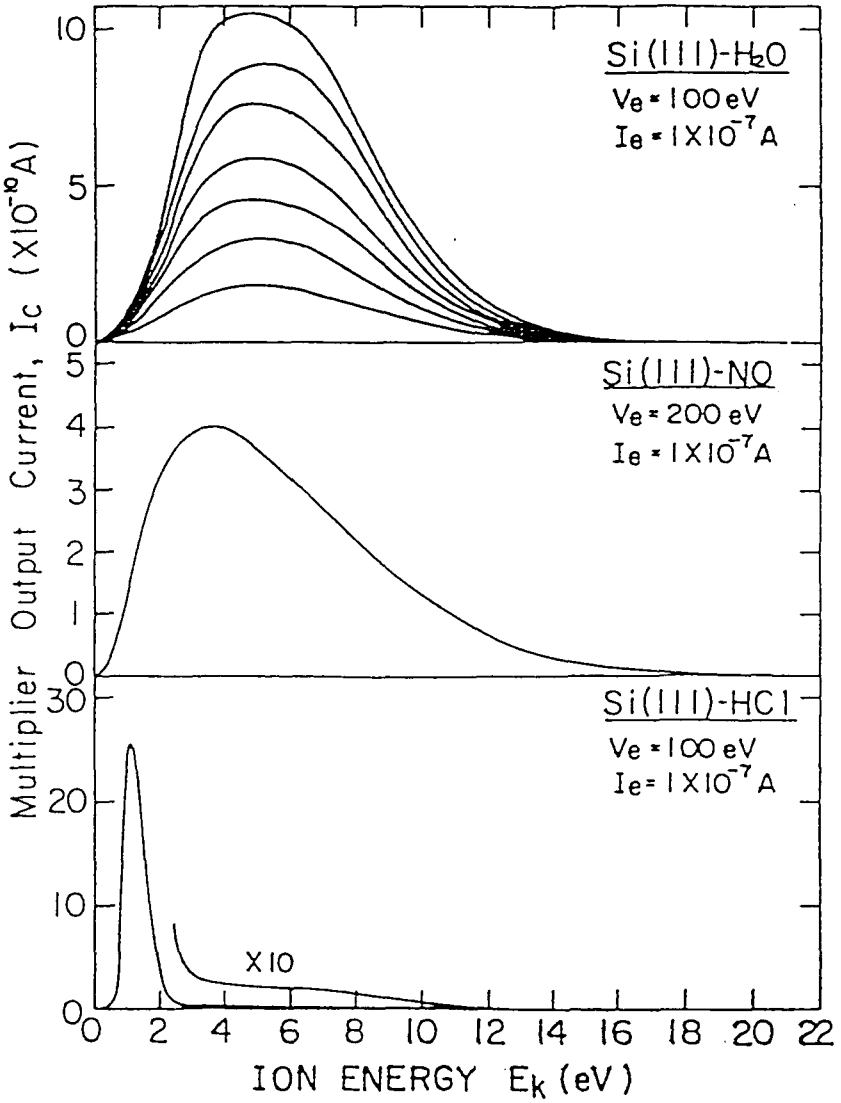

Figure 3.2: Kinetic energy distribution of the O^+ from the NO/Si(111) surface. The adsorption and measurement were done at room temperature. Spectra for the Si(111)-H_2O and Si(111)-HCl surfaces are irrelevant here. (from ref.[60])

and 147 K) at the spectrum, which the mass is 30, in Fig. 3.1(B). According this result and the result of Fig. 3.1(C), that is the peak at neither 187 and 225 meV didn't become weak after flashing at 130 K. So, we can recognize that NO desorb at 147 K and not at 110 K. Above 150 K, the peak at 187 K became weak immediately but that at 218 didn't change until 200 K. Hence, they concluded that the NO molecules adsorbed at the bridge site desorbed at 147 K and those at the on-top site did not desorb but dissociated into atomic species between 200 and 300 K. As for N_2O, they observed two stages of desorption at 110 and 147 K. From these results and that of HREELS, they have suggested that the formation of N_2O occurs via two separate processes on Si(111)7×7 surface. First, N_2O is chemically formed on the Si surface during NO exposure at 90 K and becomes physisorbed. Second, N_2O is formed during either thermal heating or photon irradiation. Nishijima *et al.*[60] observed the ESD ions from NO/Si(111) surface at room temperature and found O^+ for desorbed species which had the kinetic energy distribution with a maximum at 3.6 eV and a halfwidth of 7.2 eV (Fig. 3.2). Ying *et al.*[76] studied the photon-energy dependence of the PSD over a wavelength range of 325-440 nm with using a Xe lamp and observed an enhancement above the transition energy of the first direct band-gap of Si at 3.37 eV (370nm).

In this chapter, we first report on the desorbed ion species in ESD at 190 K and at room temperature (R.T.). In addition, we report on PSD at 90 K and their photon-energy dependence. From these results, we discuss the adsorption sites and desorption processes of ions.

3.2 Experimental

The ESD experiments were done in our laboratory and the PSD experiments were done at Photon Factory of the National Laboratory for High Energy Physics (KEK) by using the synchrotron radiation.

3.2.1 ESD

The base pressure of the experimental chamber was 8×10^{-11} $\sim1\times10^{-10}$Torr. The sample was a P-doped Si wafer with the electric resistivity of 2.4-4.0 Ω·cm and a size of $8\times15\times0.6$mm^3. The clean surface was obtained by electron-bombardment heating up to $\sim$1250°C (3 sec.×5-10 times) in the UHV chamber. The surface quality and the cleanliness were checked by the observation of the 7×7 pattern of the LEED and by the lack of the O KLL and C KLL Auger signals.

The Si wafer was spontaneously cooled down for several minutes after flashing up to 1250°C and then exposed to NO for the R.T. adsorption. For the adsorption at 190 K, liquid N_2 was used for cooling down the Si wafer. The NO gas exposure was 1.0×10^{-8} Torr× 300sec (3 L) for the adsorption at 190 K and 1.0×10^{-6} Torr× 300sec (300 L) for the R.T. adsorption. The measurement was done at the temperature of adsorption. We monitored the adsorption of NO through the change of the LEED pattern. The LEED pattern was almost 7×7 (δ7×7 [79]) for the adsorption at 190 K, whereas weak 1×1 spots were observed for the R.T. adsorption with 3 L exposure. For the R.T. adsorption, we report only the results of 300 L exposure in this thesis because we could clearly see the desorbed ions under this exposure. The NO gas nozzle was set at a distance of about 5 cm from the sample in order to avoid the dissociation of NO on the Ti surface of the Getter pump before adsorbing onto the Si surface. The equipments set up was the same as that shown in Fig. 2.5.

A two-dimensional spherical mirror analyzer [57]-[59], which is already explained at section 1.6, was used for all the measurements of: 1) the kinetic energy distribution, 2) TOF for the mass analysis, 3) the ESDIAD of the desorbed ions, 4) LEED and 5) Auger observations. The acceptance cone of the analyzer for ESDIAD was $\pm50^\circ$ from the surface normal. When we measured the kinetic energy distribution and the TOF spectra, the incident electron energy and the sample bias were set to 350 eV and 15 V, respectively. For

the TOF measurement, the incident electron beam was shaped to pulses, with the width of 400 nsec, the current of ~20 nA and the frequency of ~1000 pulses/sec.

3.2.2 PSD

This experiment was performed at the beam line BL-7B [80] of Photon Factory installed by the Faculty of Science of the University of Tokyo in collaboration with KEK. This beam line is equipped with a 1m Seya-Namioka monochromator. The analyzer chamber was equipped with a double-pass cylindrical mirror analyzer (DCMA), LEED system and a TOF tube. The schematic diagram of the equipments is shown in Fig. 3.3. The pulse of the synchrotron radiation had a width of 0.13 nsec with an interval of 624 nsec in the single bunch operation.

The sample used in the PSD experiment was cut from the same Si wafer as in the ESD experiment (P-doped, 2.4-4.0 Ω·cm) and the size was $7\times25\times0.6mm^3$. The clean surface was obtained by direct-current heating up to 1250°C (3sec.×5times) in the UHV chamber. The surface cleanliness was checked by the same way as that in the ESD experiment.

The Si wafer was cooled down to 90 K using liquid N_2 for about 20 min after flashing up to 1250°C and then exposed to NO gas. The pressure during the NO gas exposure was 1.0×10^{-6} Torr, and the exposure was 100 L. The saturation coverage was obtained at this exposure [74]. The NO gas nozzle was set in the similar way as in the ESD experiment.

The TOF drift tube was used for the mass analysis and for the measurement of the photon-energy dependence of the desorbed ions. This TOF drift tube has four grids, which had the same voltage. The acceleration was done between the sample and the first grid. We used the DCMA for the UPS and Auger measurements.

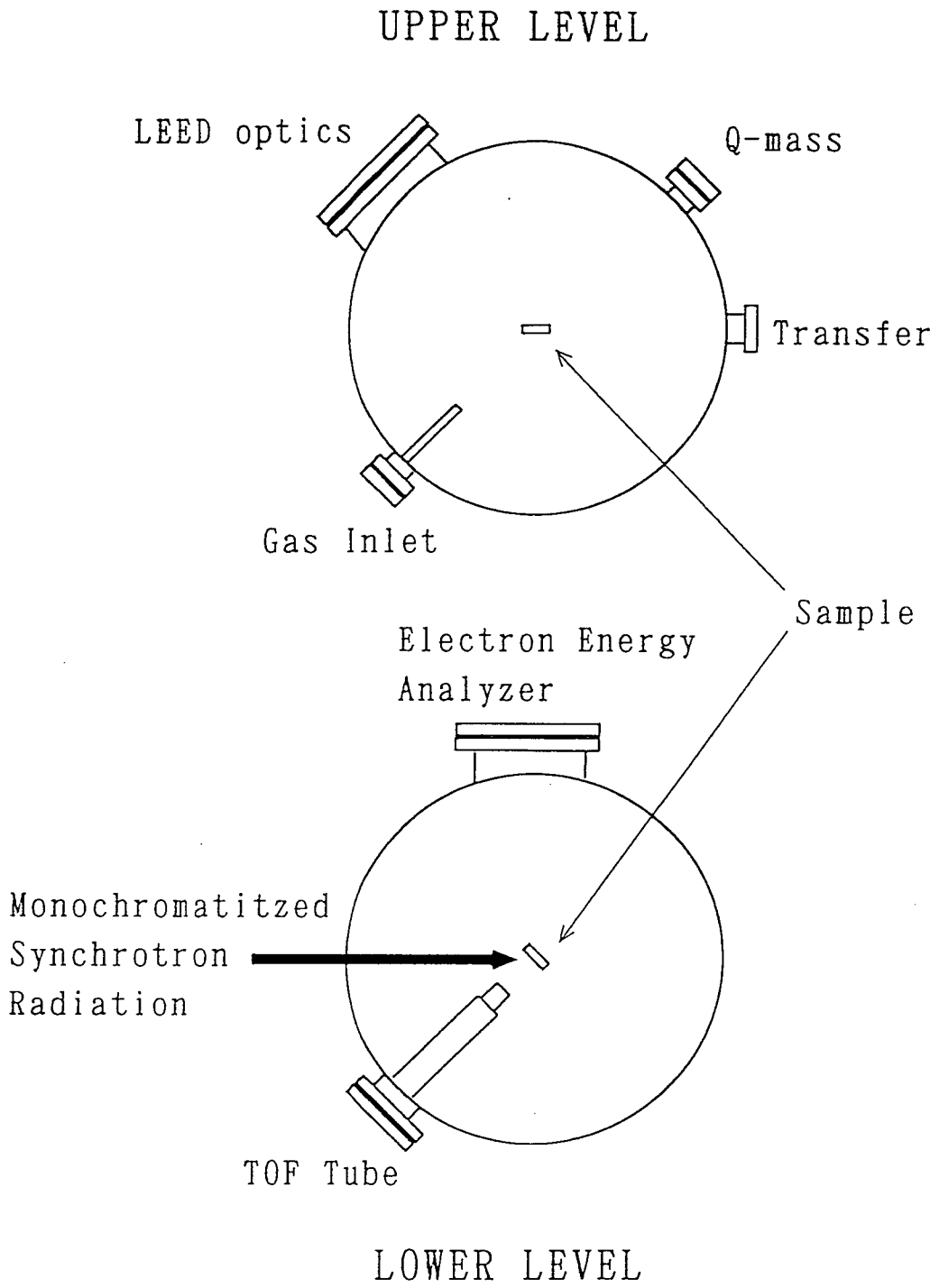

Figure 3.3: Schematic diagram of the equipments. The gas inlet, the quadruple-mass analyzer and the LEED optics are installed at the upper level. At the lower level, there are the TOF tube and the electron energy analyzer, and the synchrotron radiation through the monochromator is focussed on the sample.

3.3 Results and discussion

3.3.1 ESD

Figures 3.4(a), (b) and (c) show the TOF spectra from the 3 L NO exposed Si(111) surface at 190 K, the 300 L NO exposed surface at room temperature and the clean surface, respectively. The kinetic energy of the ions in each spectrum was originally 2 eV but the sample bias voltage (15 V) accelerated them to 17 eV. We can recognize three peaks in Fig. 3.4(a) which correspond to H^+, N^+ and O^+, whereas we can see only H^+ and O^+ peaks in Fig. 3.4(b) revealing the absence of N^+. This result on desorbed ion species from the NO/Si(111) surface at room temperature is the same as that of Nishijima *et al.*[60], who observed O^+ but no N^+. We observed the N^+ desorption from the NO/Si(111) surface for the first time at low temperature by means of ESD. At room temperature it is commonly considered that NO adsorbs only dissociatively, and the N^+ will no longer desorb because the angle of Si−N−Si bond is approximately 180° . Hence the detection of N^+ in Fig. 3.4(a) means that NO adsorbs as a molecule at 190 K. In Fig. 3.4(a) and (b), the intensity of H^+ is much larger than other peaks (O^+ or N^+). These intensity ratios do not represent the real coverage ratio because the desorption probability of H^+ is known to be much higher than O^+ or N^+. H^+ can be observed even on the clean surface kept in 10^{-11} Torr range (Fig. 3.4(c)), which is the condition that the coverage of H is less than about 10^{-3} ML within the present time scale for the measurement. The origin of H^+ is already explained at page 54. In our ESD experiment of H_2O/Si(111), H^+ was strongly observed but O^+ was not detected (not shown here). Judging from this result, we conclude that the O^+ ions are generated by the NO adsorption and not by the H_2O adsorption.

Figures 3.5(a), (b) and (c) show the kinetic energy distribution of total desorbed ions (H^+, N^+ and O^+) for the same surface as Figs. 3.4(a), (b) and (c), respectively. The threshold of the kinetic energy distribution is at about −1.0 eV for the two NO exposed surfaces ((a) and (b)) in contrast to that of the clean surface (c) (about 0 eV as shown in (c)). The

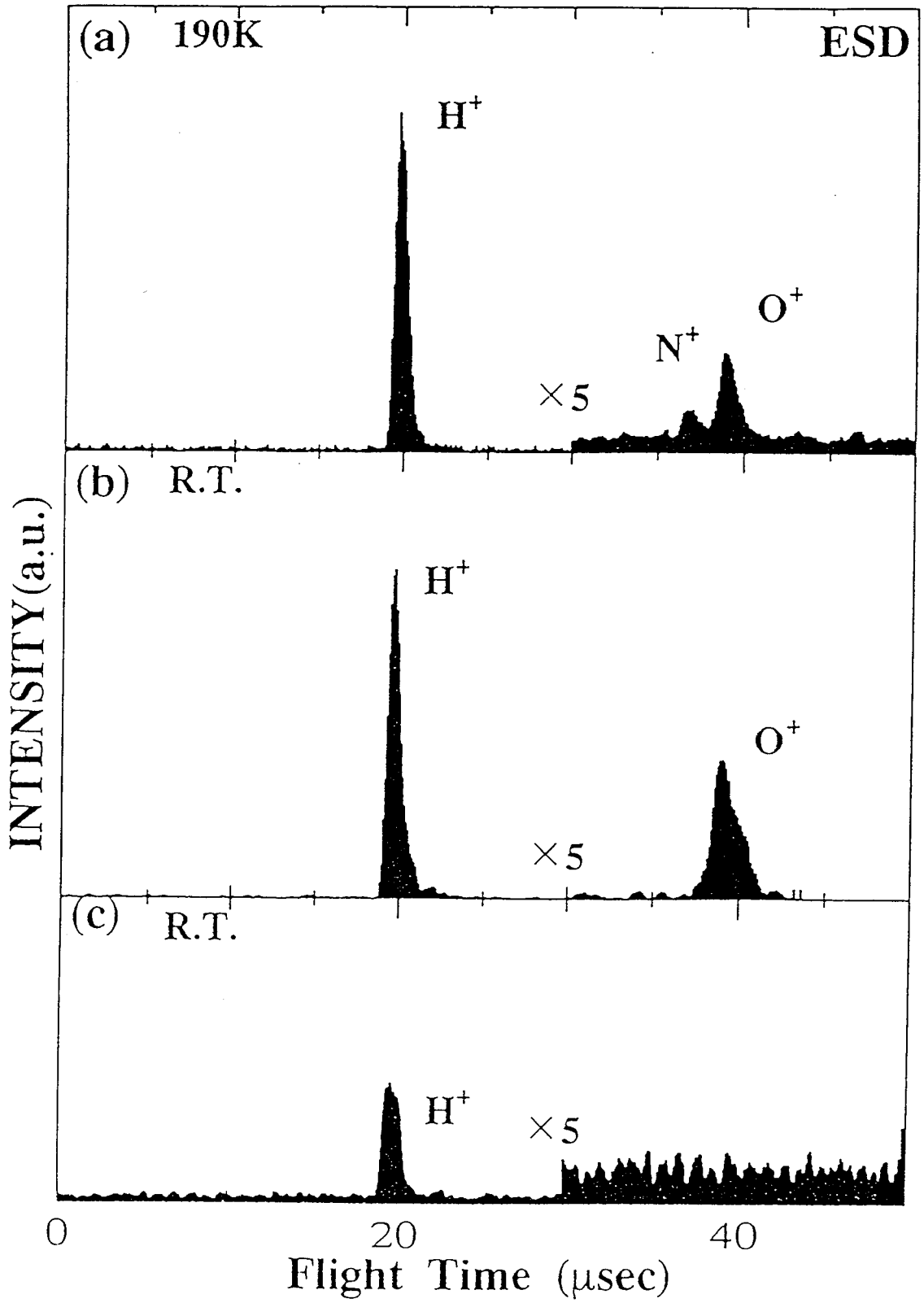

Figure 3.4: Time-of-flight spectra from the NO/Si(111) surface for (a) 3 L exposure at 190K, (b) 300 L at room temperature, and (c) the Si(111)7×7 clean surface. The original kinetic energy of the ions is set to 2 eV.

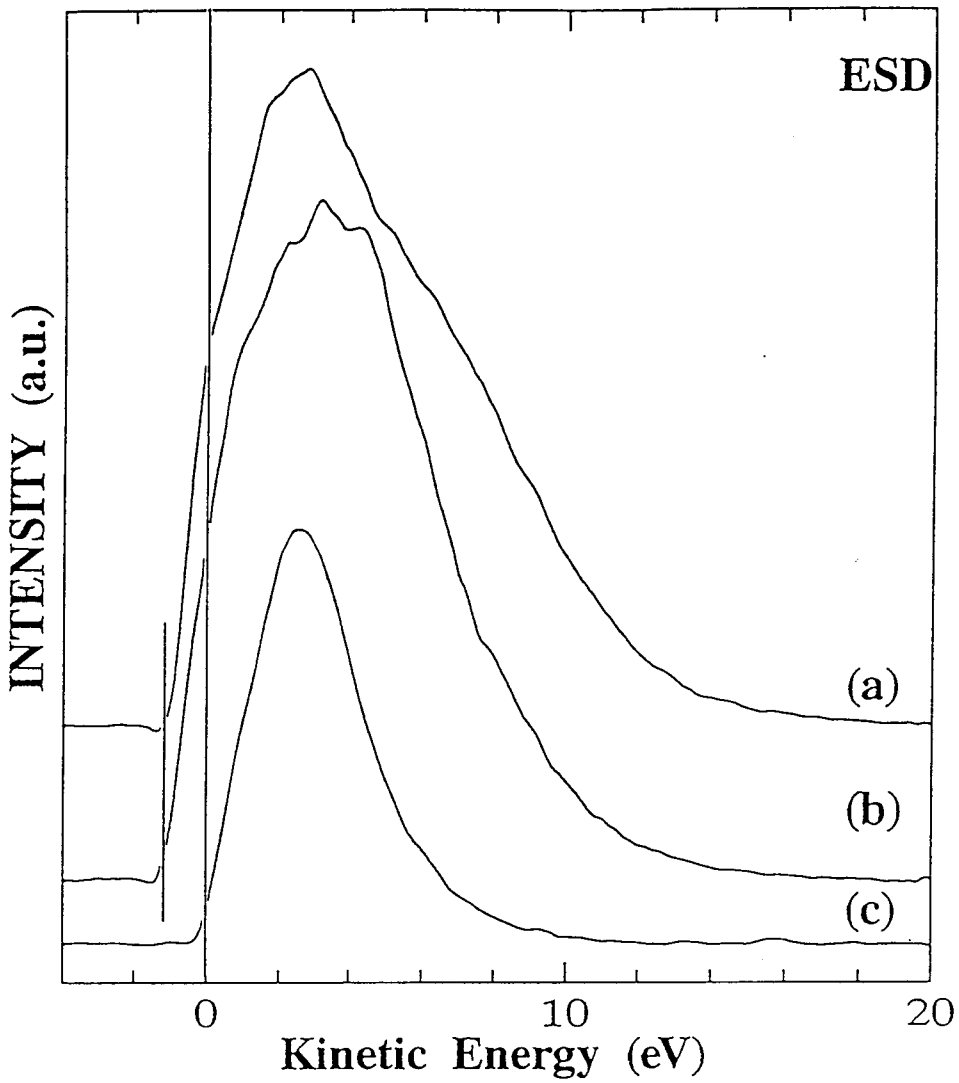

Figure 3.5: ESD ion kinetic energy distribution spectra of total desorbed ions for the (a) NO exposed surface for 3 L at 190 K, (b) 300 L at room temperature and (c) the clean surface.

nominally negative kinetic energy is caused by the definition of zero kinetic energy at the vacuum level of the analyzer and not at that of the sample. Compared with NO/Si(111), the threshold for the O_2/Si(111) surface [81] (chapter 2, Fig .2.7) stayed around 0 eV for any exposure. The difference in these two systems may be caused by the different degree of reduction of the barrier height of the potential curves in both ion desorption processes [72]. That is, the barrier height is lowered by about 1 eV in the ion desorption process on the NO adsorbed surface, whereas it is hardly changed on the O_2/Si(111) surface. Figure 3.6 shows the potential diagram for the Si(111)7×7 clean surface and the NO/Si(111) surface, to explain this argument. E_S, E_A, E_{S-A}, E_a and E'_a are the vacuum level of the sample, that of the analyzer, the difference of the vacuum level between the sample and the analyzer (which have relation to the bias voltage), the acceleration energy at the Si(111)7×7 surface and that at the NO/Si(111) surface. We set the zero kinetic energy in Fig. 3.5 at the desorbing ions which the kinetic energy are E_{S-A}, and so the threshold energy is defined by $E'_a - E_B$. Therefore, we can see that the change of the barrier height gives an explanation of the negative kinetic energy.

Taking into account the relative intensities of the observed peaks in the TOF spectra such as Fig. 3.4 for many different kinetic energies covered in Fig. 3.5, we can obtain the kinetic energy distribution of the H^+, N^+ and O^+ ions. Figures 3.7(a) and (b) are thus obtained kinetic energy distribution curves of the desorbed ions from the surface with 3L NO exposure at 190 K and 300 L NO exposure at room temperature. We can see only one peak for each H^+ and O^+ spectrum. The kinetic energy distribution of O^+ at room temperature has a peak at 2 eV with a half width of about 1.5 eV. This result is different from that of Nishijima *et al.*[60], in which the peak position was at 3.6 eV with a halfwidth of 7.2 eV. The present result is much different from that of O_2/Si(111) surface [81] (Fig. 2.8), which has a peak at 4 eV with a halfwidth of about 3.0 eV. The peak intensity ratio of O^+ for the NO/Si(111) surface to that for the O_2/Si(111) surface was about 10:1 for 300L

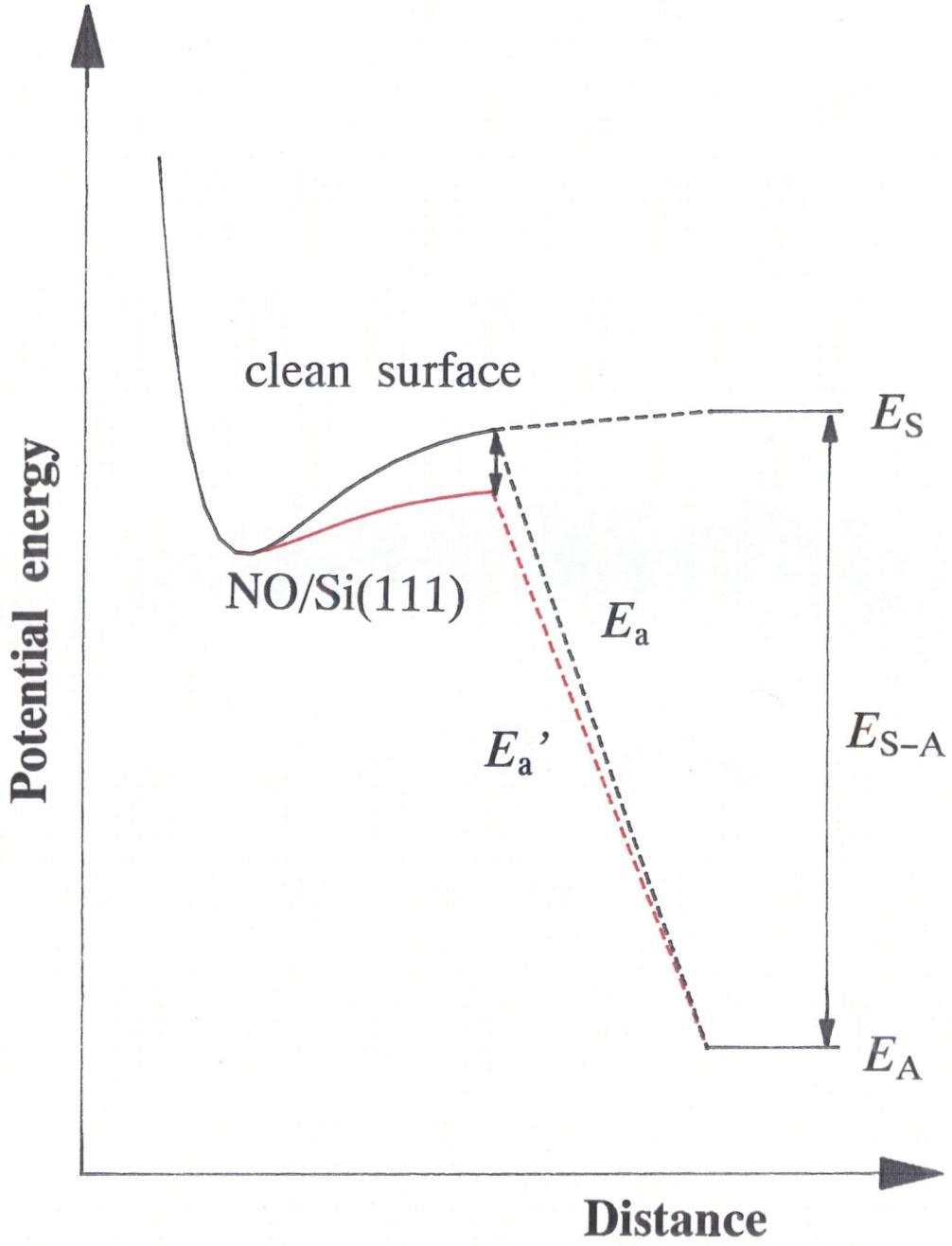

Figure 3.6: Potential diagram for the Si(111)7×7 surface and the NO/Si(111) surface. E_S, E_A, E_{S-A}, E_a and E'_a are the vacuum level of the sample, that of the analyzer, the difference of the vacuum level between the sample and the analyzer (which have relation to the bias voltage), the acceleration energy at the Si(111)7×7 surface and that at the NO/Si(111) surface.

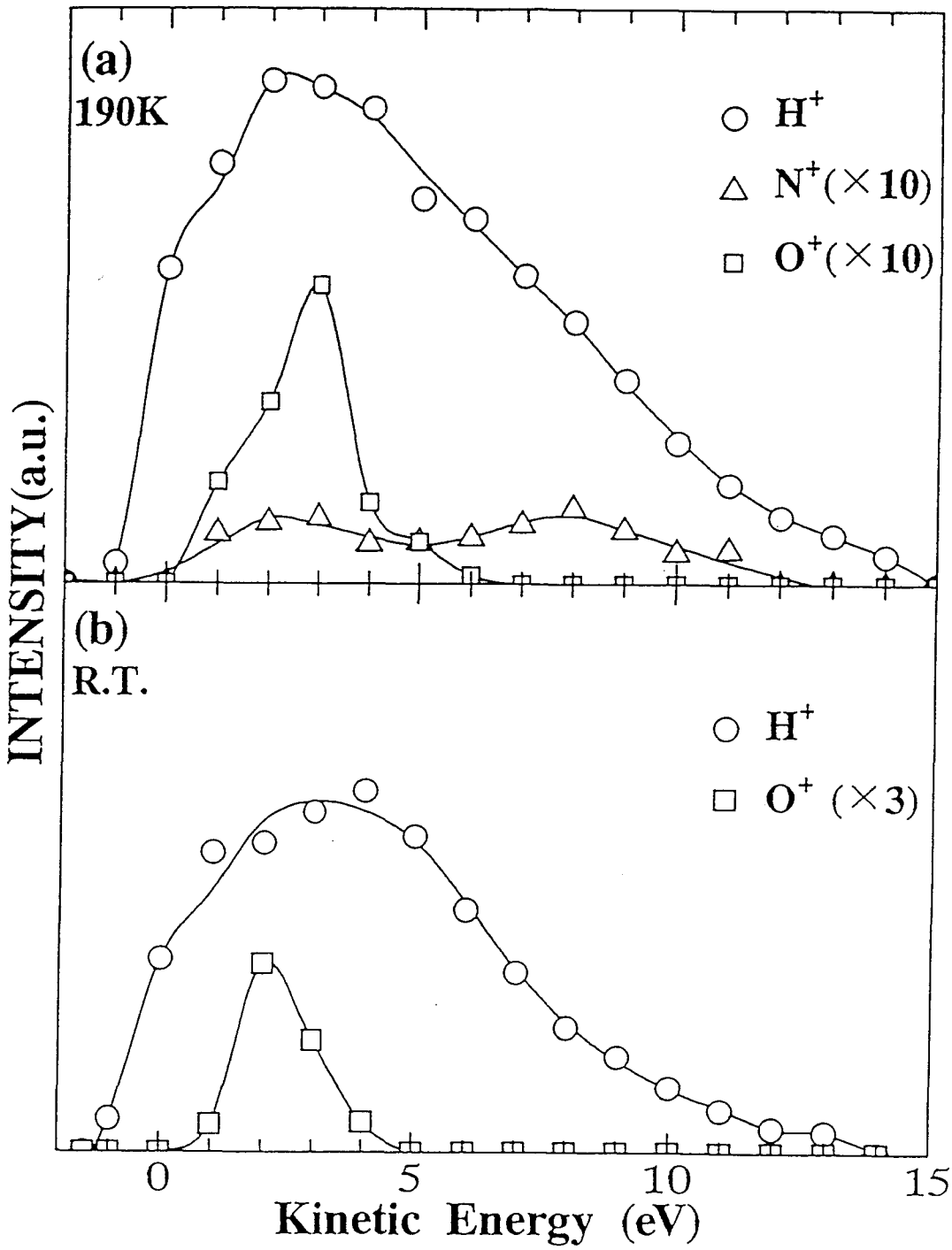

Figure 3.7: ESD individual kinetic energy distributions of H^+, N^+ and O^+ for (a) 3 L at 190 K and (b) 300 L at room temperature.

exposure at R.T. One reason for the difference of O^+ yield may be the different oxidation condition. That is, the angle of the Si−O−Si bond of the O_2/Si(111) surface may be larger than that of the NO/Si(111) surface making the desorption of O^+ more difficult.

The angular distribution patterns of the desorbed ions are shown in Fig. 3.8 . Figures 3.8(a) and (b) show the patterns of N^+ at 190 K for the kinetic energies of 2 and 8 eV, respectively. The patterns of O^+ at 190 K and R.T. are shown in Fig. 3.8(c) and (d) for the respective kinetic energies of 3 and 2 eV. The pattern of N^+ at 2 eV shows that the ion distribution is stronger at the circumference. On the contrary, the pattern at 8 eV is concentrated near the center. The patterns of O^+ shown in the figures (c) and (d) reveal that the ion distribution is much stronger at the circumference. It is generally thought that the angular distribution approximately represents the bonding direction of the desorbed species. According to the two desorption patterns of N^+, we consider that there are two adsorption sites at 190 K, that is the bridge site and the on-top site corresponding to Fig. 3.8(a) and (b), respectively. From the pattern of O^+ at R.T., we consider that the adsorption site of dissociated O atoms is not the on-top site but the bridge site.

3.3.2 PSD

The TOF spectra measured at 90 K using the 0th order light from the monochromator at BL-7B of Photon Factory are shown in Fig. 3.9. The x-axis abscissa corresponds to the time passed from the preceding light pulses to the ion detection, and so it does not always indicate the real flight time. Figures 3.9(a), (b) and (c) are the spectra when the acceleration voltages are set to 1500, 1430 and 1355 V, respectively. The spectra in the inset (a)', (b)' and (c)' are the overview spectra of (a), (b) and (c), respectively. We can see two big peaks ((D) and (H)) and two small peaks ((G) and (I)) in each spectrum, (a)', (b)' and (c)'. The peak at 0 nsec of (a), (b) and (c) did not move with the change of the acceleration voltage, suggesting that it is due to the noise from the light pulse. From these results, we can recognize that there are at least nine kinds of desorbed ions species, which

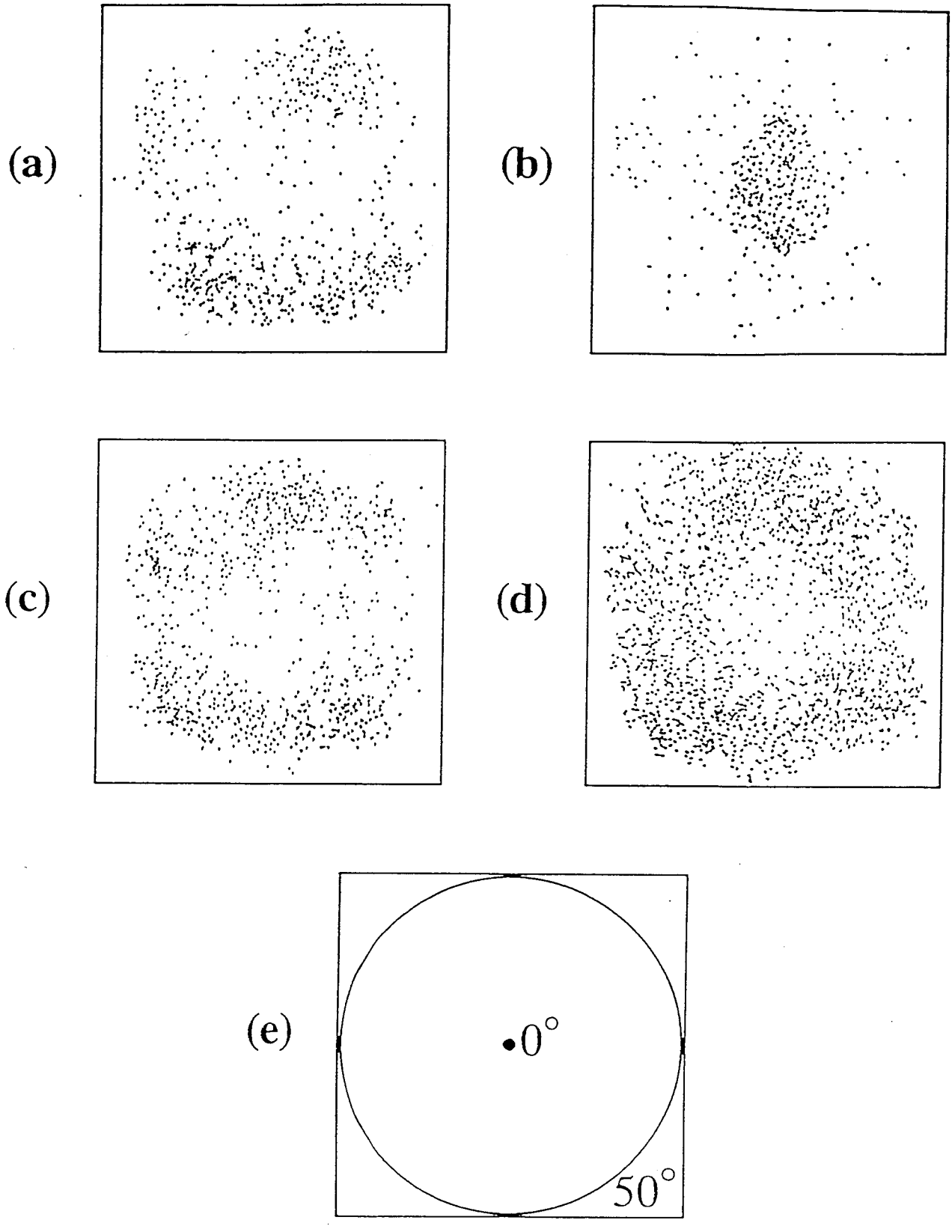

Figure 3.8: Angular distribution patterns of N^+ at 190 K from the surface with 3 L exposure measured at the kinetic energies of (a) 2 and (b) 8 eV, (c) that of O^+ at 3 eV at 190 K and (d) that of O^+ at 2 eV for the exposure of 300 L at room temperature. The corresponding polar angles are shown in (e) (the surface normal is taken as 0 °).

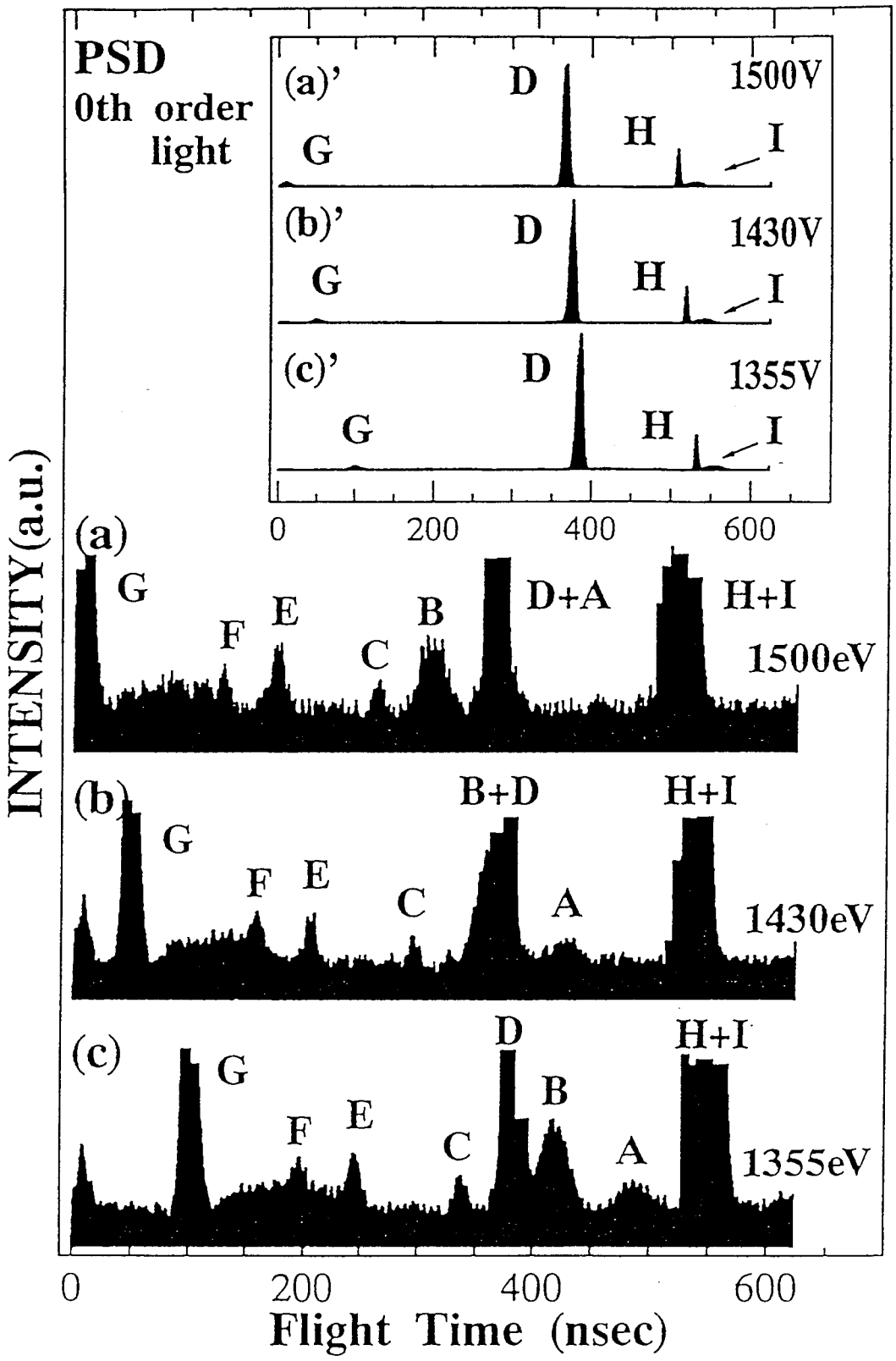

Figure 3.9: TOF spectra for the 0th order light excitation at different acceleration voltages (a) 1500 V, (b) 1430 V and (c) 1355 V. (a)', (b)' and (c)' are the magnified figures of (a), (b) and (c), respectively.

have different mass or different kinetic energies or originated from different desorption processes. Figure 3.10 shows their peak positions for different acceleration voltages. The size of the circles (both open and closed) represents the intensity of the peaks. To simplify the relation between the flight time (y-axis) and the acceleration voltage, we take $100/\sqrt{V}$ for the x-axis, where V is the acceleration voltage in volts. Hence, the x-axis corresponds to the inverse of the velocities of the charged particles. The relation between the flight time and the acceleration voltage can be described as

$$\begin{aligned} x &= \frac{100}{\sqrt{V}} \\ y &= A\frac{\sqrt{M}}{\sqrt{V+E_{\mathrm{k}}}} + B\frac{\sqrt{M}}{\sqrt{E_{\mathrm{k}}}+\sqrt{V+E_{\mathrm{k}}}} - 865n + C \qquad (3.1) \\ &= (A+B)\sqrt{\frac{M}{V}} - 865n + C, (for E_{\mathrm{k}} = 0) \qquad (3.2) \end{aligned}$$

A is a parameter which corresponds to the length of the TOF drift tube. E_{k} represents the initial kinetic energy of the desorbed ion represented by eV. Hence, the first term of this equation indicates the time spent in the TOF drift tube. The parameter B corresponds to the length of the acceleration area between the sample and the first grid, and so the second term represents the time spent in this area. A and B are common for each ion. The parameter n indicate the number of the light pulses between the ion desorption and the ion detection. So n is equal to zero if the ion is detected before the next light pulse is incident on the sample. C is a constant corresponding to the time delay in the electrical circuit. Considering that the kinetic energy (E_{k}) of the desorbed ion is much smaller than the acceleration voltage (V), eq. (3.1) is approximated by to eq. (3.2). Hence, we can determine the mass M of the ion species from the slope of the fitted line. The solid lines in Fig. 3.10 are the fitted lines by eq. (3.1) with (A) M=32, E_{k}=0 (B) M=30, E_{k}=0 (C) M=16, E_{k}=3 (D) M=1, E_{k}=5 (E) M=14, E_{k}=2 (F) M=14, E_{k}=8.5 and (G) M=22, E_{k}=0. The lines (A'), (B') and (G') are the extended lines of (A), (B) and (G), respectively. The nine lines ((A)-(I)) correspond to the nine peaks of Fig. 3.8, respectively.

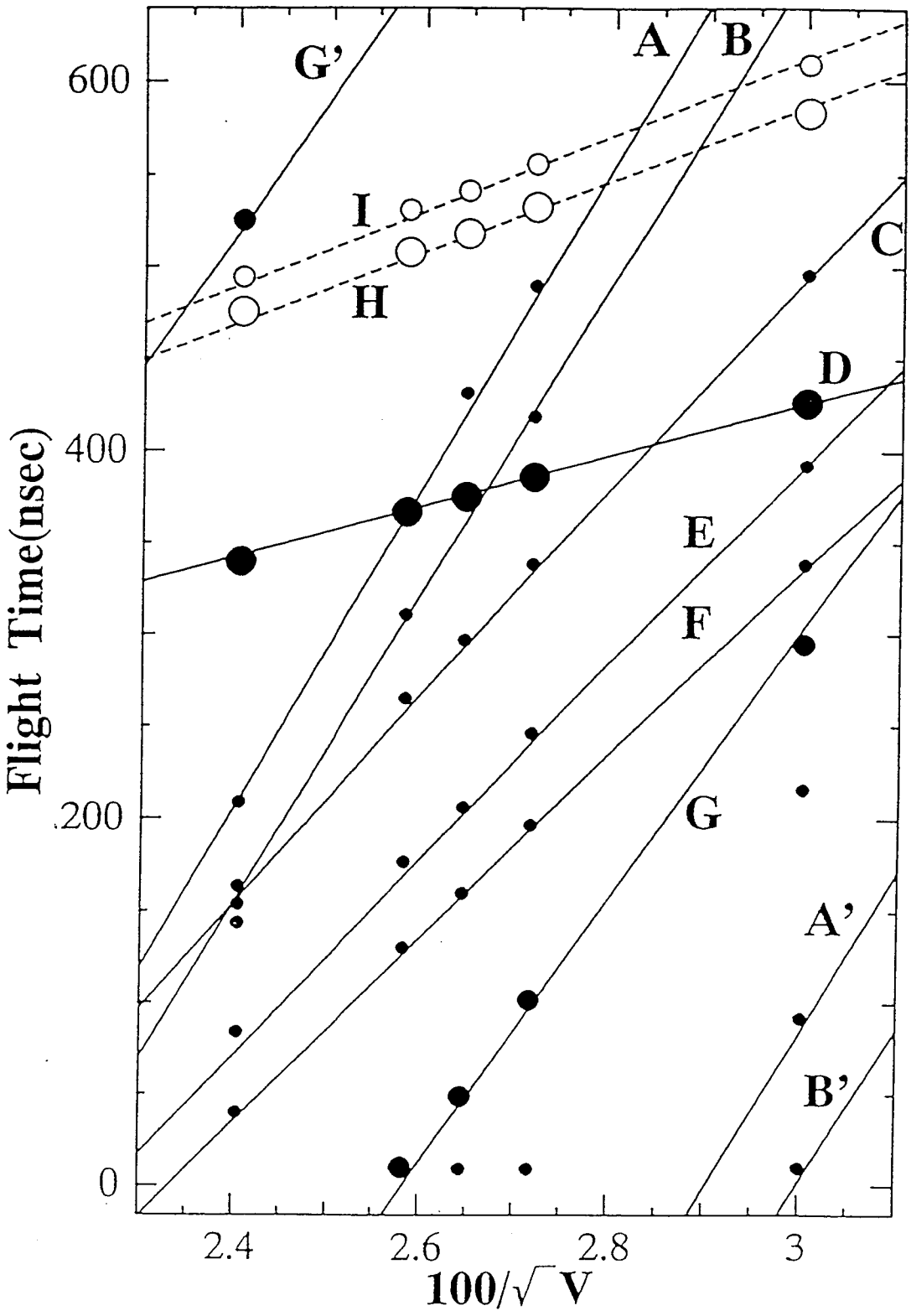

Figure 3.10: Acceleration voltage dependence of the TOF's peaks. The solid and broken lines are calculated by the eq. (3.1) and (3.2).

So, the species of the desorbed ions are (A) O_2^+, (B) NO^+, (C) O^+, (D) H^+, (E) N^+ and (F) N^+. No atom with the mass 22 exists, so we considered (G) as N_2O^{2+} whose mass is 44. The acceleration energy of the di-valent ion is twice as that of the monovalent ion, but the slopes of both ions are the same since both x and y contain the term proportional to $1/\sqrt{V}$. The difference of the ordinate between (E) N^+ and (F) N^+ came from the different kinetic energies (E_k) of eq. (3.1). In our ESD studies at 190 K, we have already found two peaks of the kinetic energy distribution of the N^+ ion (2 and 8 eV (Fig. 3.7(a))). Hence, the TOF result of PSD agrees well with the ESD result. According to our results of the ESD ion angular distribution, (E) is ascribed to the N^+ desorbed from the bridge site and (F) is ascribed to that from the on-top site.

We have detected not only NO^+, O_2^+ but also N_2O^{2+} in our PSD experiments for the first time. Ying *et al.*[74] have reported that physisorbed N_2O desorbs thermally above 110K. So, the ion species (O_2^+, NO^+ and N_2O^{2+}) detected by PSD at 90 K, which we have not observed in our ESD experiment at 190 K or R.T., might be created from the physisorbed N_2O at 90 K. It is clearly seen in Fig. 3.9 that the intensity of H^+ is much larger than other peaks. But, by the same reason as we have adopted in explaining in the ESD results and in the result of the O_2/si(111) surface, this intensity ratio does not represent the coverage ratio.

If we fit the open circles of Fig. 3.10((H) and (I)) in the same way as before, their masses become (H) M=1.7 and (I) M=1.8, respectively, when E_k= 0eV for both (H) and (I). There is no atom of such a mass. Hence we suspect that these peaks originate from different processes. Then we suppose that the neutral atoms are desorbed and ionized between the sample and the first acceleration grid. In this case the effective acceleration energy becomes smaller than the first grid voltage, and the length of the acceleration area becomes shortened. The broken lines for (H) and (I) in Fig. 3.10 are the fitted lines by eq. (3.2) with V and B multiplied by 0.45 (H) and 0.4 (I), respectively for M=1 and E_k=0eV.

But we cannot still determine the origin of these H^+ in detail from this experiment.

Figure 3.11 shows the UPS spectra of the Si(111)7×7 clean surface and the NO adsorbed surface at 90 K measured at the photon energy hν=35 eV. We can see three prominent peaks and one small shoulder in the spectrum of the adsorbed surface. These structures are assigned to the 2π (the binding energy E_B=4.4 eV), 1π+5σ (9.0 eV), 4σ (13.8 eV) and 3σ (19.0 eV) molecular orbitals.

The 0-th order light excited PSD was already shown in Figs. 3.9 and 3.10. Then we measured the photon-energy dependence of the ion desorption yield around 20 eV, which corresponds to the 3σ molecular orbital excitation. Figure 3.12 shows the TOF spectra at the photon energies of hν = 18.0, 19.0, 19.5, 20.5 and 22 eV for the acceleration voltage of 1430 V. The species of desorbed ions in this photon energy range were identified as H^+, N^+ (for both adsorption sites) and N_2O^{2+} in comparison with Fig. 3.9, and no other peak was observed. From this photon energy dependence in Fig. 3.12, we estimated the threshold of the N^+ desorption from the bridge site (bridge-N^+) as 19.0 eV. The peak shape of N^+ from the on-top site (on-top-N^+))is rather obscured compared with that of bridge-N^+, but its threshold energy is nearly the same as that of bridge-N^+. This result suggests that the desorption process occurs with the mechanism of the KF model [39], since N^+ desorbed after the excitation of the 2s core of the O atoms. Because the excitation of the 3σ molecular orbital (mainly O 2s derived state) causes the desorption of the N^+ from both the bridge- and on-top site NO, NO is thought to be adsorbed molecularly with the N atoms up and the O atoms down on the Si(111) surface, that is the O atoms are bonding with the Si atoms (Fig. 3.13). It has been generally thought that the N atoms are directly bonding with the Si atoms. But the N^+ desorption results in Fig. 3.12 suggest that the N atoms are not directly bonding with the Si atoms since N^+ is desorbed by the excitation of the O atoms. The intensity of the N_2O^{2+} was strong even at hν =18eV. Considering the intensity ratio of the N^+ desorption from the bridge site and N_2O^{2+} in

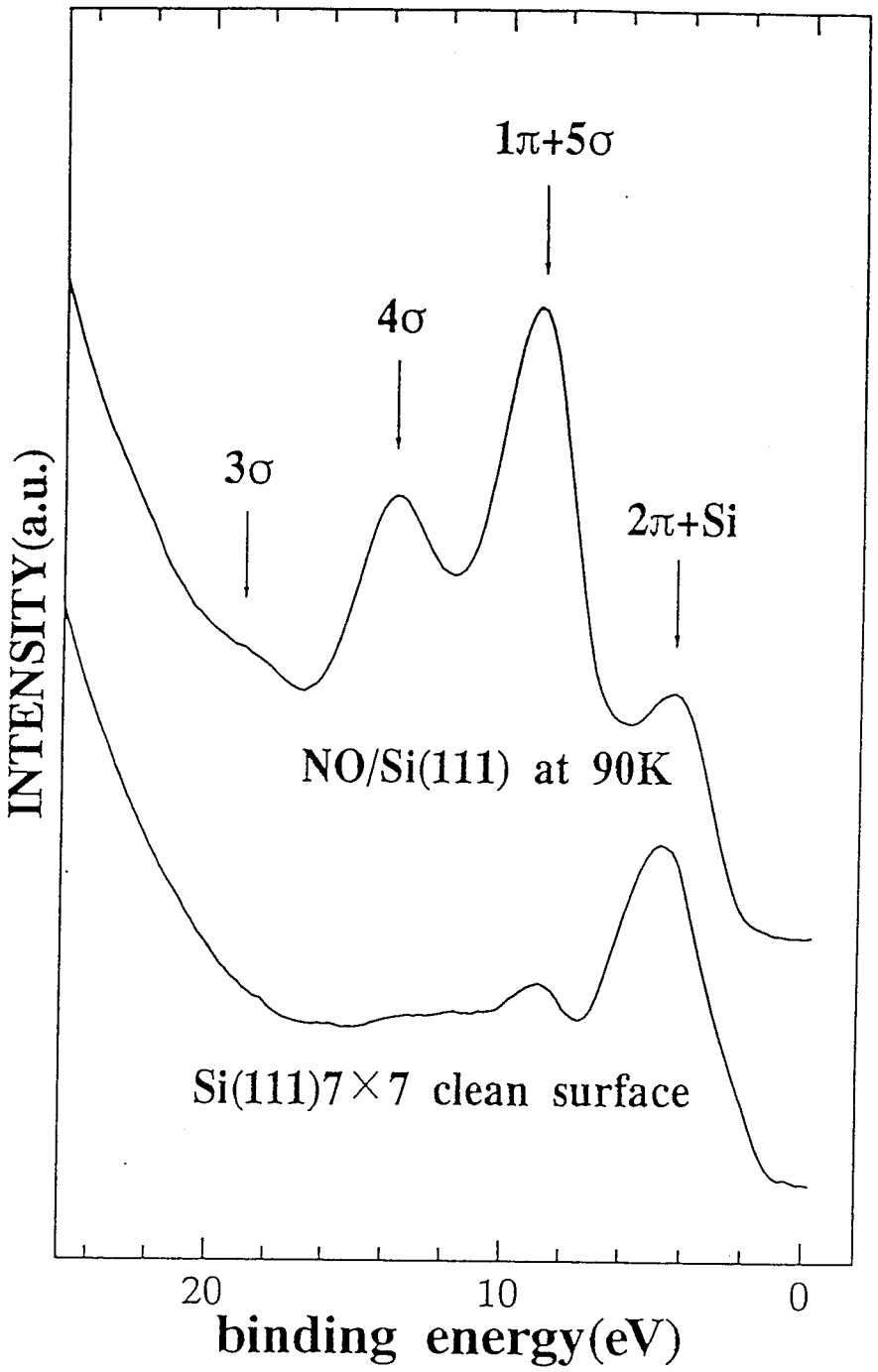

Figure 3.11: UPS spectra of the Si(111)7×7 clean surface and NO/Si(111) surface (90 K).

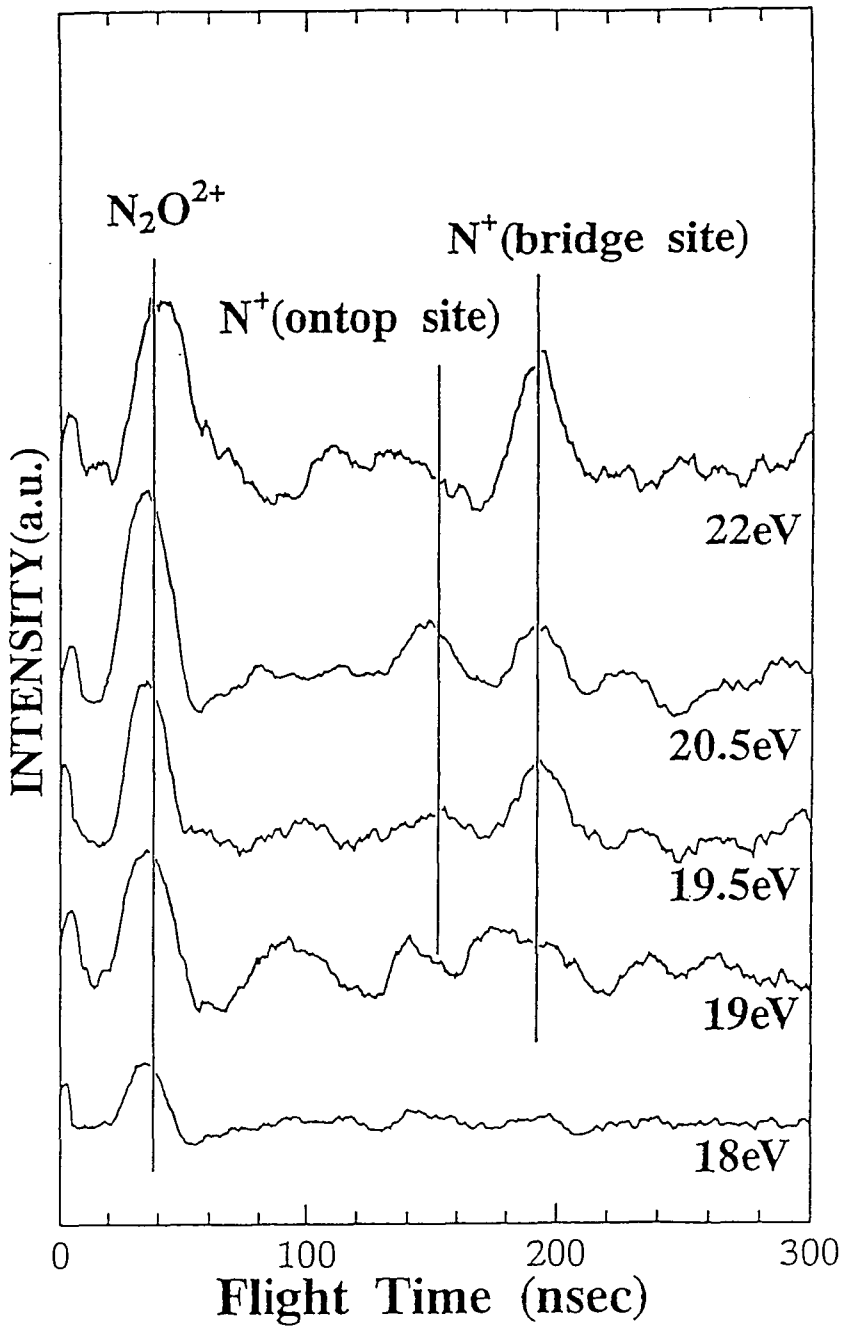

Figure 3.12: TOF spectra at different photon energies. The acceleration voltage was 1430V.

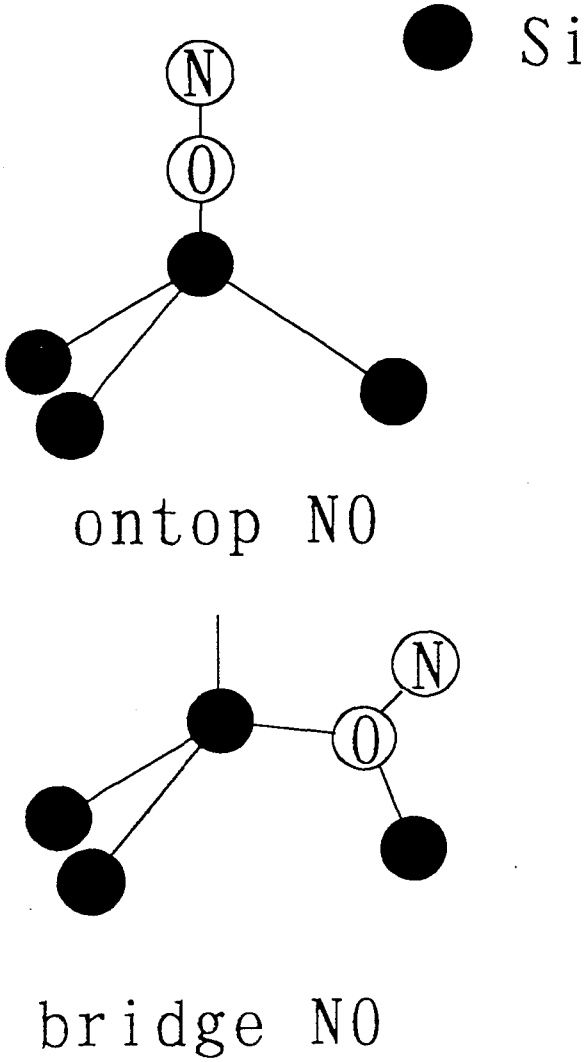

Figure 3.13: Schematic representation of the adsorbed site of NO on the Si(111)7×7 clean surface.

Fig. 3.9 (0th order light excitation) and Fig. 3.12 (monochromatic light excitation), we have found that the ratio is much larger in Fig. 3.12 for the excitation above 19 eV. Consequently, the desorption of N_2O^{2+} at 18eV in Fig. 3.12 may be caused not by the 1st order monochromatic light but by the higher order light.

3.4 Summary

We studied the desorption process on the NO adsorbed Si(111) surface at 190 K and at room temperature by means of ESD and at 90 K by PSD. For ESD, the desorbed ion species were H^+ and O^+ at R.T. whereas N^+ was observed for the first time at 190 K. In addition to these species, NO^+, O_2^+ and N_2O^{2+} were observed for the first time in our PSD experiment at 90 K. In the ESD experiment, we observed two types of N^+ which have different kinetic energies. By taking the ESDIAD patterns into account, we conclude that these two types correspond to the two adsorption sites of NO, that is the bridge (low kinetic-energy species) and on-top sites (high kinetic-energy ones). From the results of the photon energy dependence of PSD, we propose that the desorption process occurs with the mechanism of the KF model [39], since N^+ desorbed after the excitation of the 2s core of the O atoms. Because the desorption of N^+ occurs with the excitation of the 3σ molecular orbital, NO will be adsorbed molecularly with the N atoms up and O atoms down on the Si(111) surface with O atoms bonding with the Si atoms.

Chapter 4

Photoemission studies of the Si(111)3×1-K surface

In this chapter, we report on the detailed dispersion of electronic states and the saturation coverage of the Si(111)3×1-K determined by means of ARUPS as well as XPS.

4.1 Preface

Studies of alkali metal adsorption on semiconductor surfaces are very interesting subjects with respect to the changes of the geometrical and the electronic structures. Among these, the Si(001)-K and Si(111)-K systems have been studied most extensively [79][82]-[87]. The structural changes of the Si(111)7×7 surface by alkali metal adsorption have been observed by means of RHEED [79][88], LEED [89]-[91], AES [91], STM [86][92][93], STS [93], ISS [87] and core-level shift [94]. Daimon *et al.*[79] found a new 7×7 structure at room temperature, named δ7×7, and a 3×1 structure at high temperature for all alkali metals (Li, Na, K, Rb and Cs) using RHEED, and proposed the saturation coverage of the 3×1 surface as 2/3ML. Mizuno *et al.*[88] heated the Si(111)1×1-Li surface and found 4×4, $\sqrt{3} \times \sqrt{3}$ and 3×1 RHEED patterns with increasing temperature, which corresponds to the decreasing of the coverage. LEED studies [89][90] have pointed out that these LEED data of the 3×1 phases show very similar intensity-voltage ($I - V$) curves suggesting that the 3×1 phase is made of Si reconstruction only being stabilized by small amount of alkali metals. Fan

et al.[91] studied the Li and Na covered Si(111) surfaces and found the 3×1 reconstructed surface at 0.01 ML. Hashizume *et al.*[86] observed the Si(111)3×1-K structure at 300°C using field ion-STM (FI-STM), and proposed a structure model, which has two K atoms in the 3×1 unit mesh. Figure 4.1 show their STM image and their model of the Si(111)3×1-K surface structure. Wan *et al.*[92] studied the 3×1 reconstruction of the Si(111) surface induced by adsorption of Li using STM, and proposed a missing-top-layer (MTL) model which has parallel "π-bond like" chains of which the Si atoms are terminated by the Li atoms, and one dangling bond per unit cell remains (Fig. 4.2). The number of Li atoms in the 3×1 unit mesh is two in this model. Recently, Hashizume*et al.*[87] measured the absolute K coverage of the ideal Si(111)3×1-K surface by ISS as 1/3 ML. Okuda *et al.*[94] also suggested the saturation coverage of the Si(111)3×1-Na surface as 1/3 ML. In this way, the structural model and the saturation coverage of these alkali metal adsorbed 3×1 surfaces are still controversial problems.

The electronic structure of alkali-metal-adsorbed Si(111) surfaces at room temperature (δ7×7 surfaces) has been studied experimentally using UPS [95][96], ARUPS [97] and IPES [96]. Magnusson *et al.*[96] have observed the changes of the occupied surface states S_1, S_2 and S_3, and the unoccupied surface state U_1 (0.5 eV above the Fermi level) which is the adatom-derived empty surface state, upon evaporation of K. Figure 4.3 shows their result. We can see that the S_1 state shifted to larger E_B from the Fermi level with increasing intensity in the initial stage of the K adsorption, and the Fermi level crossing disappeared. S_2 and S_3 states also shifted to larger E_B. But after a certain evaporation time, the intensity of the S_3 state became weak and the S_2 structure merged with the S_1 structure. (The same results are independently confirmed by Tezuka *et al.*[97].) Although the intensity of the empty surface state U_1 drastically decreased and vanished after a certain evaporation time, a new empty surface state U_1' appeared at 1.0 eV above the Fermi level. This state shifted to 0.4 eV for the saturation coverage. According to these results, they concluded that the K

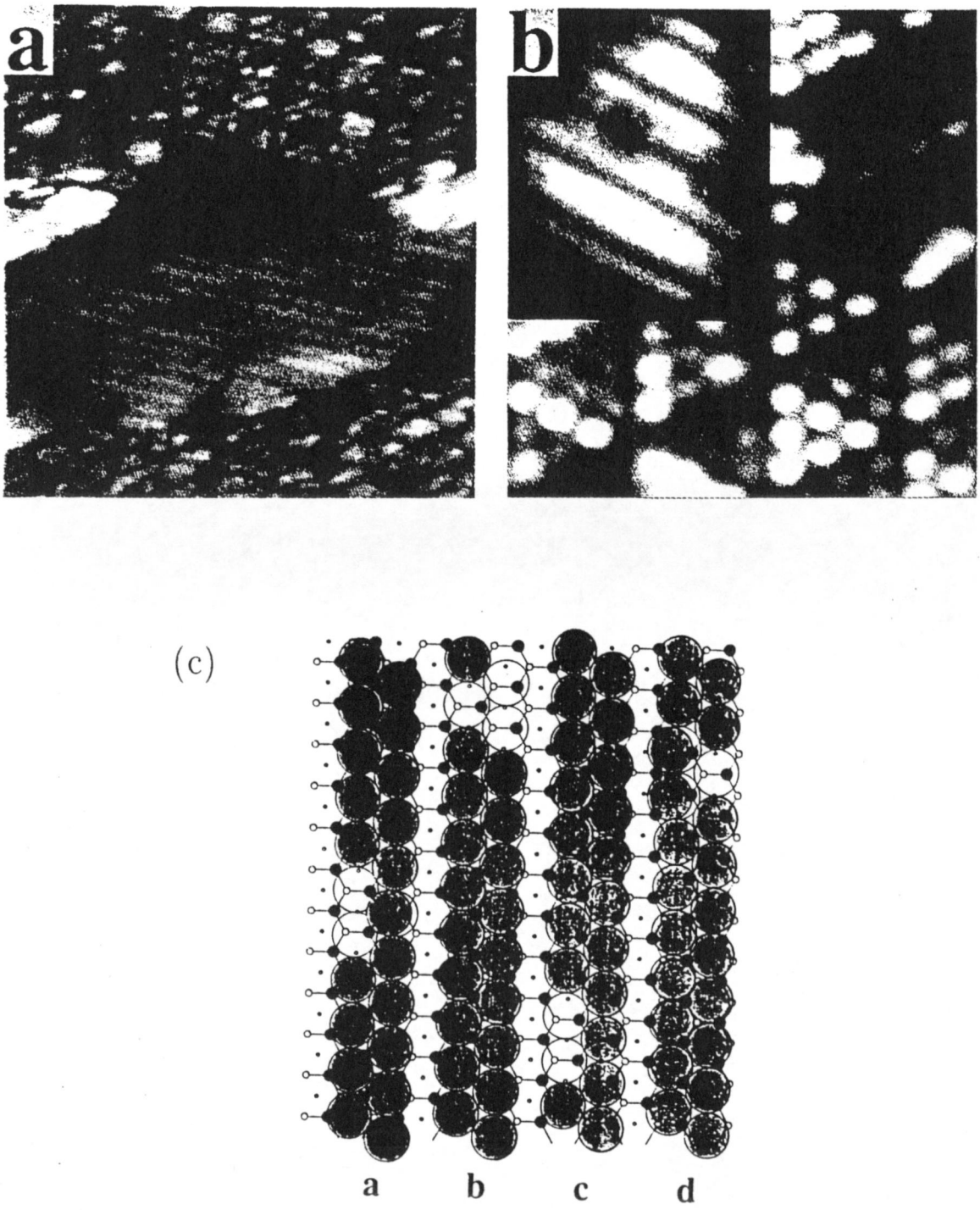

Figure 4.1: STM image of the Si(111)3×1-K surface. Both the 3×1 phase (lines) and δ7×7 phase (triangles) are observed. The sample biases are (a) −1.6 V and (b) −2.0V. (c) The top view of the surface structure model. The dots and small open circles show the 1×1 substrate. The small filled and large open circles represent the first and second Si layer. The large filled circles are the K atoms. (from ref.[86])

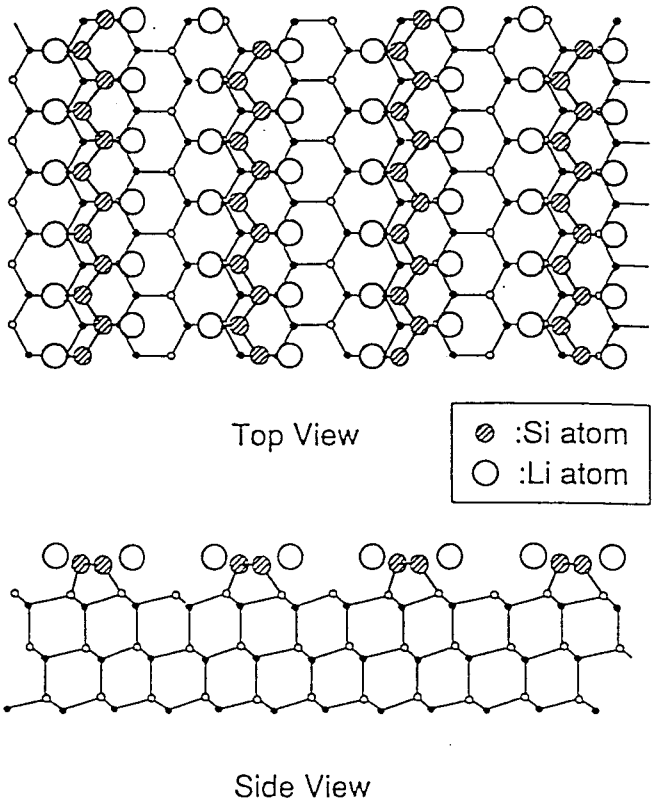

Figure 4.2: The top view and side view of the missing-top-layer model for the 3×1 structure. parallel "π-bonded like" chains of Si atoms are spaced $3a$ apart, and the dangling bonds in each chain are terminated by Li atoms. (from ref.[92])

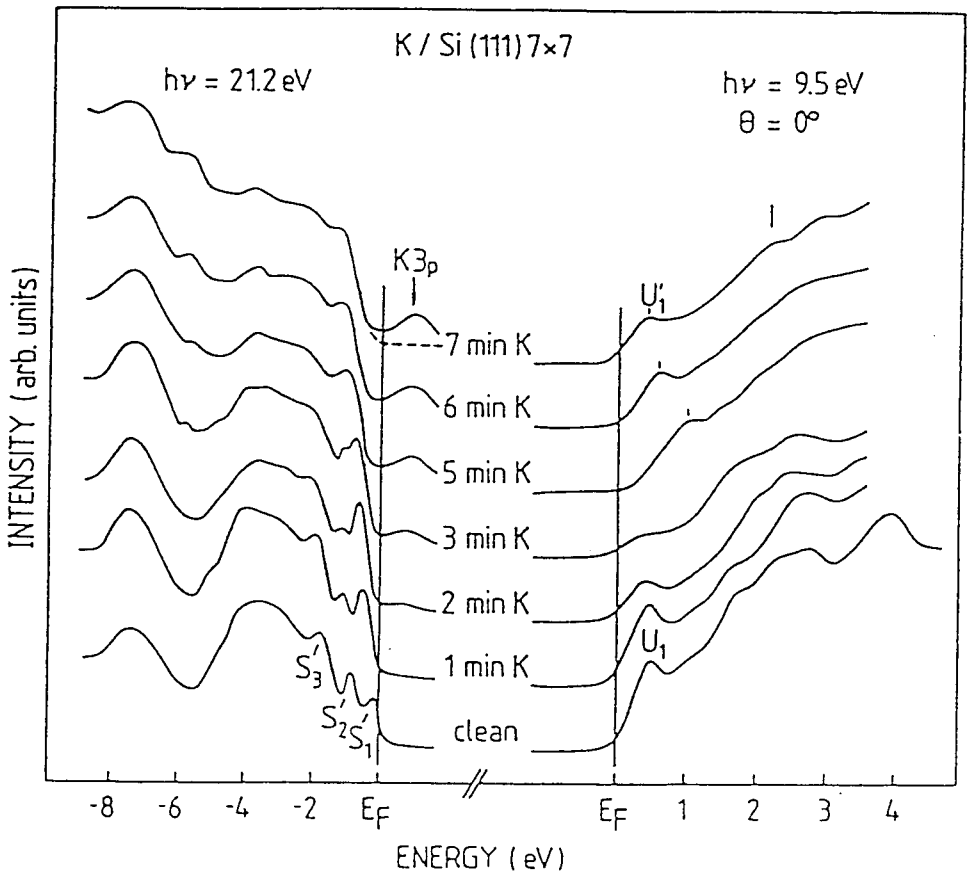

Figure 4.3: UPS and IPES spectra of the K/Si(111)7×7 surface at different deposition times. The dashed line of the 7min spectrum represents the He I UPS curve with the He II emission suppressed. (from ref.[96])

atoms adsorbed on the dangling bonds of the Si(111)7×7 surface make the Si(111)δ7×7-K surface semiconducting. Base on their result, the saturation coverage of the Si(111)δ7×7-K surface will be more than 19/49, when all dangling bonds are terminated with one or more K atoms, like the Si(111)δ7×7-H surface. Jeon *et al.*[93] measured the $I-V$ curves of the Si(111)3×1-Na surface in STS, and found the surface state band gap of about 1 eV (Fig. 4.4).

4.2 Experimental

The experiments were performed at the beam line BL-18A of Photon Factory installed by the Institute for Solid State Physics (ISSP) of the University of Tokyo in collaboration with the National Laboratory for High Energy Physics (KEK). This beam line is equipped with a constant-deviation-angle grazing-incidence monochromator and an angle-resolved photoelectron spectrometer (VG ADES 500). The overall instrumental angular and energy resolutions were ~1° and ~150 meV, respectively, at hν=21.2 eV. The analyzer chamber was also equipped with a LEED system, a Mg/Al twin anode X-ray source and an electron spectrometer (VG CLAM) for XPS. The schematic diagram of the equipments is shown in Fig. 4.5. The base pressure of this chamber was 2×10^{-11}Torr.

The sample was a P-doped Si wafer with the electrical resistivity of 2.4-4.0 Ω·cm and the size of $4\times20\times0.6$mm^3. The clean surface was obtained by direct-current heating up to ~1250°C (3sec.×5times) in the UHV chamber. The surface quality and the cleanliness was checked by the observation of the 7×7 LEED pattern and the lack of the peak of the O 1s and C 1s signals in the XPS spectra.

In order to make a Si(111)δ7×7-K structure, the Si wafer was spontaneously cooled down for several minutes after flashing up to 1250°C. The K atoms were then deposited using an alkali metal dispenser (from SAES Getters) which was mounted about 3 cm apart from the Si wafer. On the other hand, the Si wafer was kept at 500°C during the deposition in

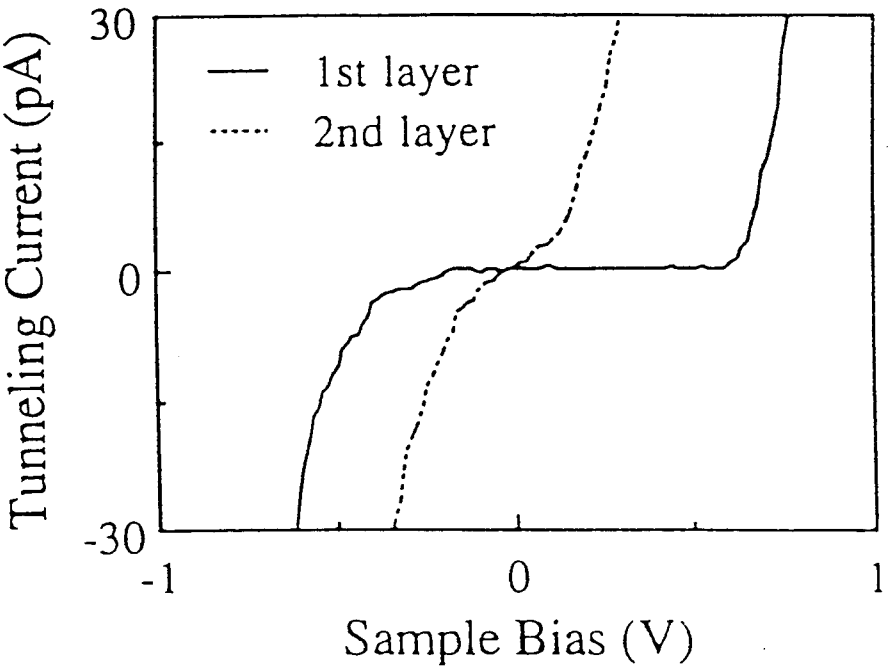

Figure 4.4: Spatially averaged tunneling $I - V$ curves obtained from the first and second layer of Na.(from ref.[93])

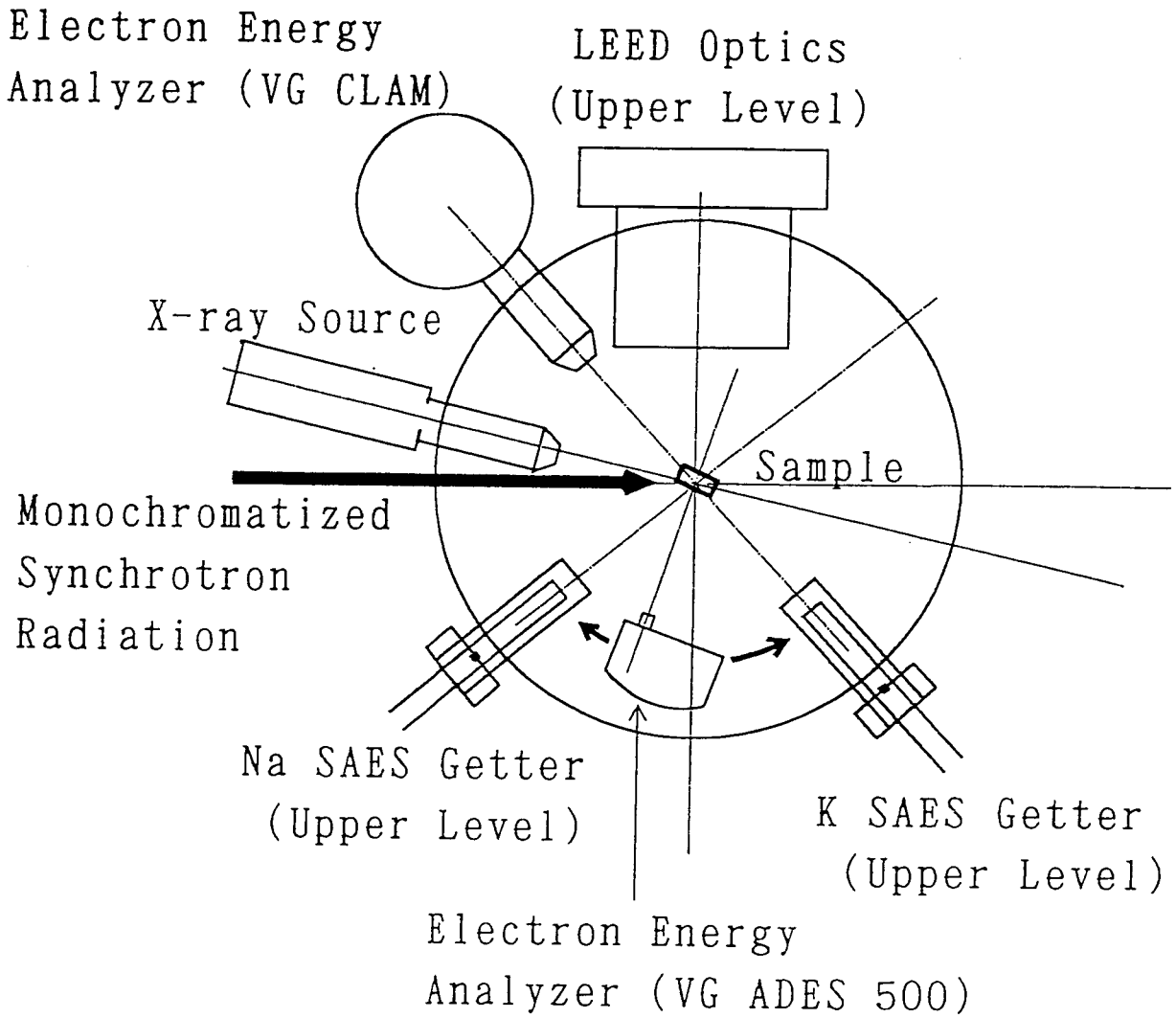

Figure 4.5: Schematic diagram of the equipments. Equipments for sample preparation; SAES alkali metal dispenser and LEED are installed at the upper level. At the lower level, monochromatized synchrotron radiation and X-ray from Al and Mg cathodes are focussed on the sample.

order to make a good Si(111)3×1-K structure [79]. The pressure during the K deposition was close to 1.5×10^{-10}Torr. We checked the amount of adsorption of the K atoms by the change of the LEED pattern and the change of the work function from the value of the clean surface, 4.595 eV. The determination of the saturation coverage was made by measuring the change of work function and the ratio of the XPS intensities of the Si *LVV* Auger peak and the K 2p core XPS peak.

4.3 Results and discussion

The UPS spectra taken for the Si(111)7×7 clean surface and the Si(111)3×1-K surface at the emission angle θ_e=0±0.5° (surface normal) are shown in Fig. 4.6. The incidence angle, θ_i, of the linear polarized light (p-polarized) was 45° from the surface normal. The accurate surface normal direction was determined from the symmetry of the observed dispersion. The Fermi level position in the UPS spectra was determined from the measurement of the metallic Fermi edge of the Ta sample holder. The spectrum of the Si(111)7×7 surface shows the occupied surface states S_1 and S_2 at 0.2 and 0.9 eV, respectively. We can not see the S_3 state clearly because of the projected bulk bands which hide it at this emission angle. The S_1 state seems to be crossing the Fermi level. The spectrum of the Si(111)3×1-K surface shows a shoulder at 0.95 eV (S_2') and a peak at 1.6 eV (S_3'), but it shows no peak at the position of the S_1 state. These results suggest the disappearance of the Fermi level crossing.

The ARUPS spectra of the Si(111)3×1-K surface measured along the $[11\bar{2}]$ and $[10\bar{1}]$ directions are shown in Fig. 4.7. The accurate $[11\bar{2}]$ azimuthal direction was determined by measuring the symmetry of the dispersion around the observed symmetry point $\bar{M}$. The $[10\bar{1}]$ direction was set by rotating the sample azimuth by 30° from the $[11\bar{2}]$ direction. The ARUPS measurements were done at every 2° from θ_e=0° to 18° and at every 3° from θ_e=18° to 69° for the $[11\bar{2}]$ direction. For the $[10\bar{1}]$ direction, we measured the spectra at every 2°

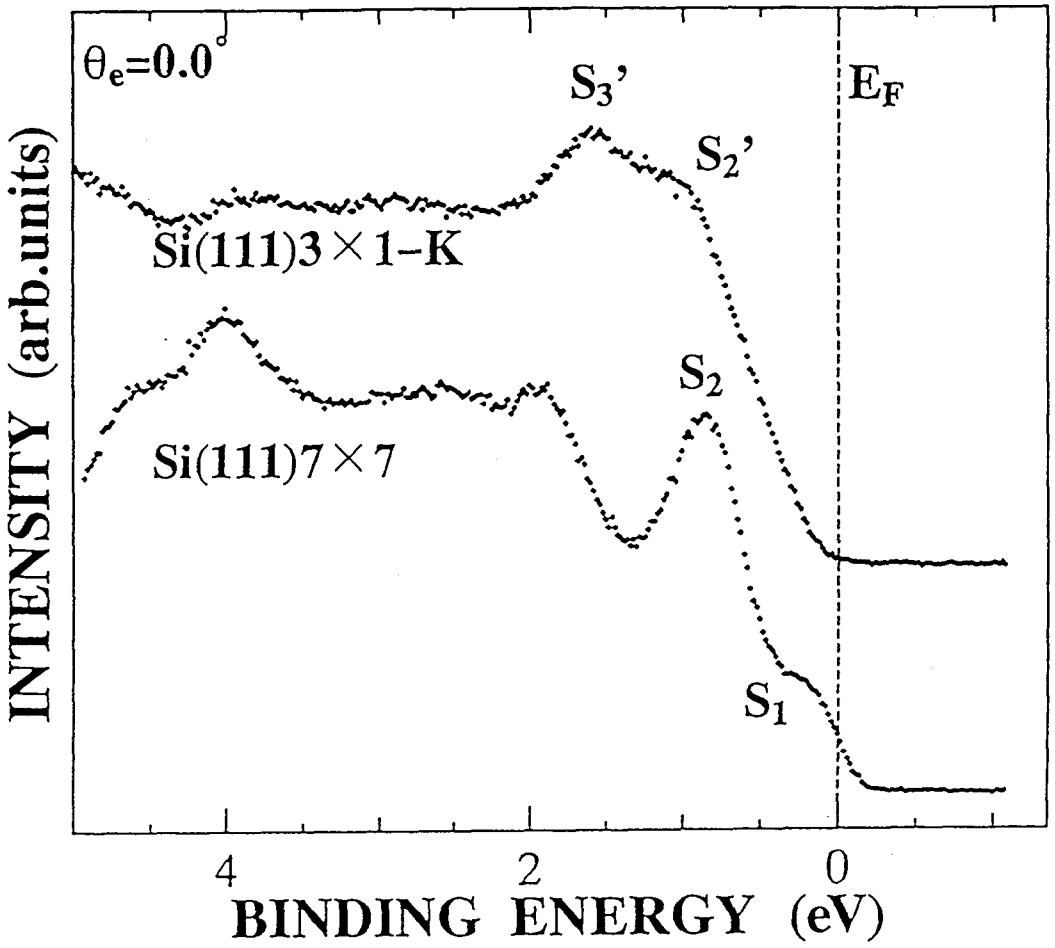

Figure 4.6: Ultraviolet photoemission spectra of the Si(111)7×7 clean surface and the Si(111)3×1-K surface at emission angle θ_e=0° for the photon energy of hν=21.2 eV.

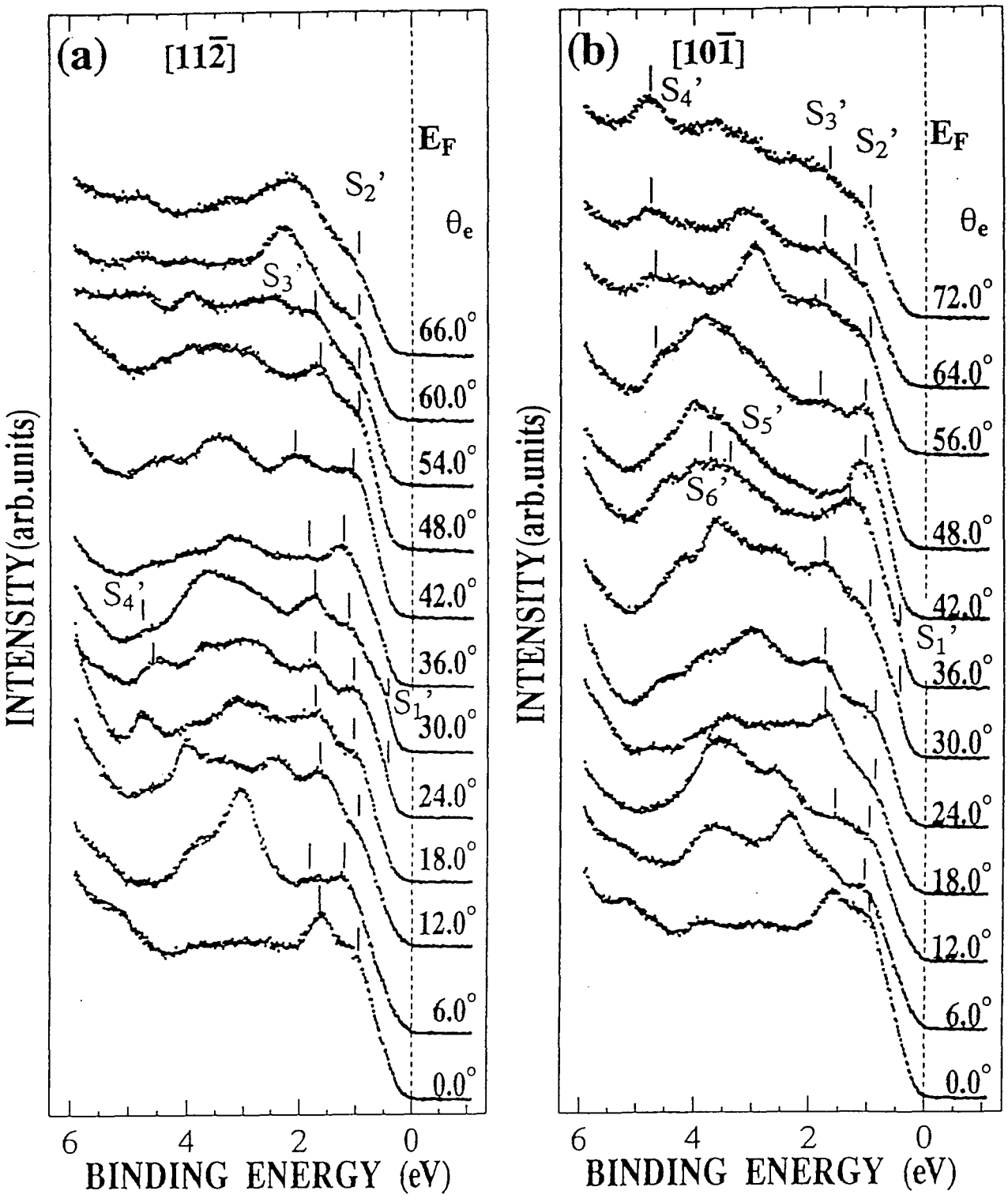

Figure 4.7: ARUPS spectra of the Si(111)3×1-K surface along the (a) [11$\bar{2}$] and (b) [10$\bar{1}$] directions. Tick marks indicate the surface state's peaks.

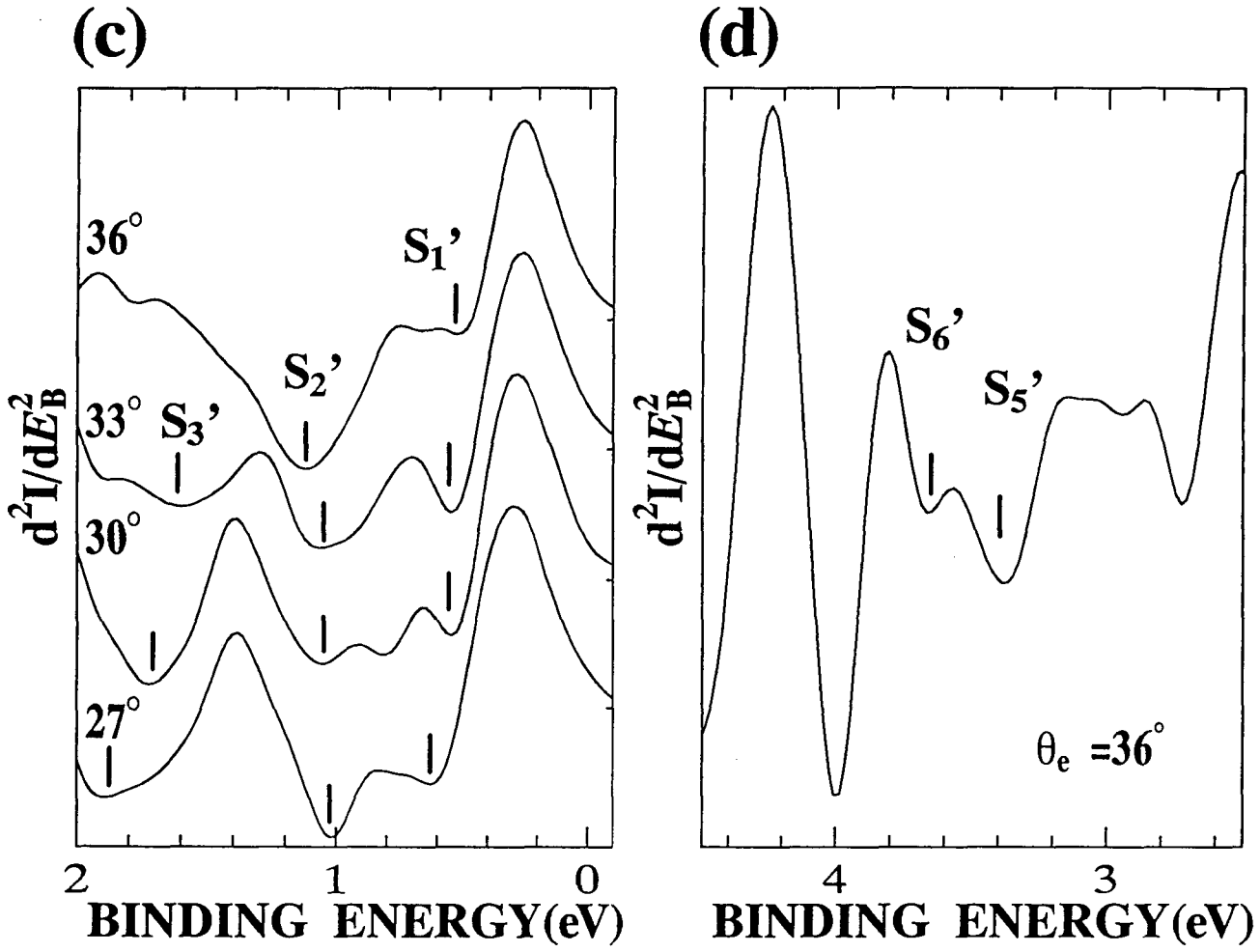

Figure 4.8: The second derivative spectra (a) at $\theta_e = 27°$, 30°, 33° and 36°, and (b) at $\theta_e = 36°$, for the [10$\bar{1}$] direction. Tick marks indicate the position of the minima of the second derivative spectra which correspond to the position of the surface states.

from θ_e=0° to 18° , at every 3° from θ_e=18° to 48° and at every 4° from θ_e=48° to 76° . For both directions, the incidence angle of the photon, θ_i, is 45° from the surface normal for the region of θ_e from 0° to 39° , and θ_i=35° for $\theta_e > 39°$. This change of θ_i was so made to avoid the reflected light to enter the analyzer. Any spectrum in Fig. 4.7 does not show appreciable intensity at the Fermi level. In addition, no structure is observed near the E_B of the S_1 state. From these results, it is concluded that the Si(111)3×1-K surface is no longer metallic but semiconducting, and the Si dangling bonds are completely filled on this surface. With increasing the binding energy, we observed structures S_1' (very weak shoulder), S_2', S_3', S_4', S_5' and S_6' as recognized in Figs. 4.7(a) and (b). These structures are in the band gap region of the projected density of states as shown in Fig. 4.9 later. Figure 4.8(a) shows the second derivative spectra at θ_e=27°, 30°, 33° and 36°, for the [10$\bar{1}$] direction. In this figure, we can see the S_1' state, which is difficult to be confirmed in both Figs. 4.7(a) and (b). Figure 4.8(b) shows the second derivative spectrum at θ_e=36° for the [10$\bar{1}$] direction to clarify the S_5' and S_6' states.

We show in Fig. 4.9(a) the SBZ of the Si(111)1×1 and the Si(111)3×1-K surface. The symbol $\bar{\Gamma}$ is the symmetry point of the 1×1 and the 3×1 surfaces and the symbols $\bar{M}$ and $\bar{K}$ are the symmetry points of the 1×1 surface. The symbols $\bar{A}$, $\bar{B}$, $\bar{C}$, $\bar{D}$, $\bar{E}$, $\bar{F}$, $\bar{G}$, $\bar{H}$ are used tentatively in this thesis for describing the symmetry points shown in Fig. 4.9(a) in the 3×1 SBZ. According to the three-fold symmetry of the Si(111)1×1 surface structure, this 3×1 structure is composed of three sets of domains which differ by 120° in azimuthal direction from each other. Hence, we must consider three types of the SBZ 3×1 structure as shown in Fig. 4.9(b). When we measure the ARUPS along the [11$\bar{2}$] direction, we probe not only the information along the $\bar{\Gamma} \rightarrow \bar{C} \rightarrow \bar{\Gamma} \rightarrow \bar{C} \rightarrow \bar{\Gamma} \rightarrow \bar{C} \rightarrow \bar{\Gamma}$ direction but also that along the $\bar{\Gamma} \rightarrow \bar{E} \rightarrow \bar{F} \rightarrow \bar{E} \rightarrow \bar{\Gamma}$ direction. In the case for the [10$\bar{1}$] direction, we likewise get information along the $\bar{\Gamma} \rightarrow \bar{G} \rightarrow \bar{H} \rightarrow \bar{A}\bar{B} \rightarrow \bar{E} \rightarrow \bar{D} \rightarrow \bar{C} \rightarrow \bar{D} \rightarrow \bar{E} \rightarrow \bar{A}\bar{B} \rightarrow \bar{H} \rightarrow \bar{G} \rightarrow \bar{\Gamma}$ direction in addition to that along the $\bar{\Gamma} \rightarrow \bar{D} \rightarrow \bar{G} \rightarrow \bar{E} \rightarrow \bar{H} \rightarrow \bar{F} \rightarrow \bar{H}$

$\rightarrow \bar{E} \rightarrow \bar{G} \rightarrow \bar{D} \rightarrow \bar{\Gamma}$ direction at the same time.

Figure 4.10 summarizes the dispersion of the electronic states of the Si(111)3×1-K surface estimated from the present experiment. The filled circles represent the positions of the observed peaks and shoulders in the ARUPS spectra, (or the positions of the minima of the secondary differential spectra). Their size represents the intensity of the peaks and shoulders classified visually. The open circles are the data reversed at the symmetry point $\bar{M}$. The projected bulk bands (hatched regions) are from reference [98]. In the [10$\bar{1}$] direction (Fig. 4.10(b)), the symmetry point $\bar{K}$ of the 1×1 SBZ corresponds only to the $\bar{E}$ point of 3×1 SBZ. Regarding this symmetry point, we can see five surface states (S_1', S_2', S_3', S_5' and S_6', at 0.54, 1.07, 1.59, 3.39 and 3.67 eV, respectively) in the band gap. In addition, we can recognize one more surface state near the $\bar{M}$ point, in the gap at about 4.75 eV (S_4'). Therefore, the number of surface states will be six. But we do not discuss the surface states (S_5' and S_6') near the $\bar{K}$-point of the 1×1 SBZ because the numbers of data points were limited. Since we have substantially probed the two directions in the 3×1 SBZ at the same time, we expect seven structure of the surface states for four surface state branches which we can guess from the above discussion. Such seven surface state structures are indicated in Fig. 4.11 by crosses for S_1', solid lines for S_{2A}', S_{3A}' and S_{4A}' and by broken lines for S_{2B}', S_{3B}' and S_{4B}' (where the broken line is hidden by the filled circles). The solid and broken lines correspond to the dispersion of the surface states along the $\bar{\Gamma} \rightarrow \bar{C} \rightarrow \bar{\Gamma} \rightarrow \bar{C} \rightarrow \bar{\Gamma} \rightarrow \bar{C} \rightarrow \bar{\Gamma}$ and $\bar{\Gamma} \rightarrow \bar{E} \rightarrow \bar{F} \rightarrow \bar{E} \rightarrow \bar{\Gamma}$ for the [11$\bar{2}$] direction in Fig. 4.11(a), and along the $\bar{\Gamma} \rightarrow \bar{G} \rightarrow \bar{H} \rightarrow \bar{A}\bar{B} \rightarrow \bar{E} \rightarrow \bar{D} \rightarrow \bar{C} \rightarrow \bar{D} \rightarrow \bar{E} \rightarrow \bar{A}\bar{B} \rightarrow \bar{H} \rightarrow \bar{G} \rightarrow \bar{\Gamma}$ and $\bar{\Gamma} \rightarrow \bar{D} \rightarrow \bar{G} \rightarrow \bar{E} \rightarrow \bar{H} \rightarrow \bar{F} \rightarrow \bar{H} \rightarrow \bar{E} \rightarrow \bar{G} \rightarrow \bar{D} \rightarrow \bar{\Gamma}$ for the [10$\bar{1}$] direction in Fig. 4.11(b). The surface state bands S_{2A}', S_{2B}', S_{3A}', S_{3B}', S_{4A}' and S_{4B}' are traced by considering the equivalence of E_B at each symmetry point. For example, the E_B at one symmetry point $\bar{C}$ is equivalent at another $\bar{C}$ points along each direction. Likewise the E_B at the symmetry point $\bar{G}$ is equivalent at the other $\bar{G}$ point along the $\bar{\Gamma} \rightarrow \bar{G} \rightarrow \bar{H} \rightarrow \bar{A}\bar{B}$

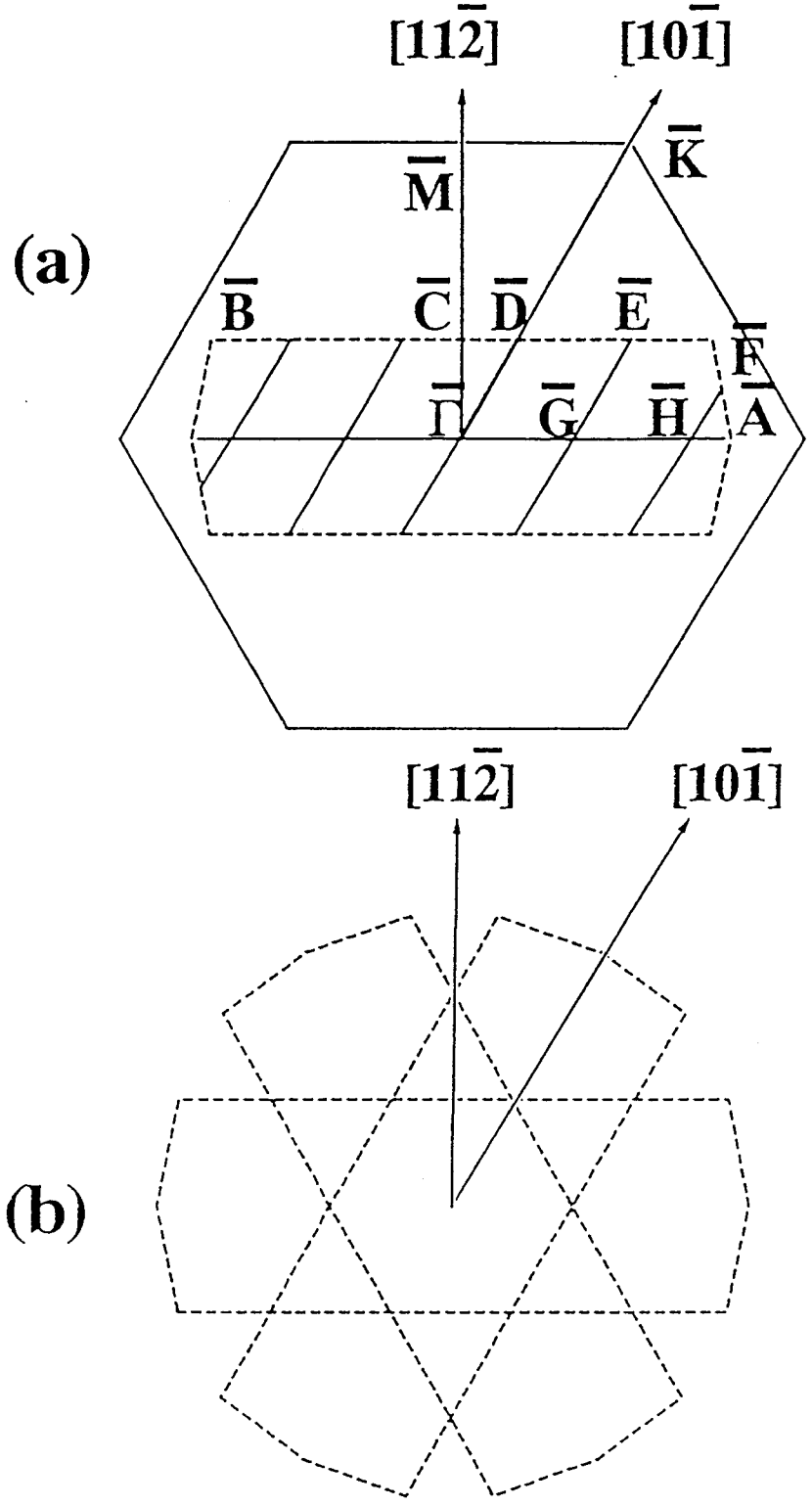

Figure 4.9: (a) The surface Brillouin zones of the Si(111)1×1 and the Si(111)3×1-K surface. (b) The three equivalent 3×1 surface Brillouin zones.

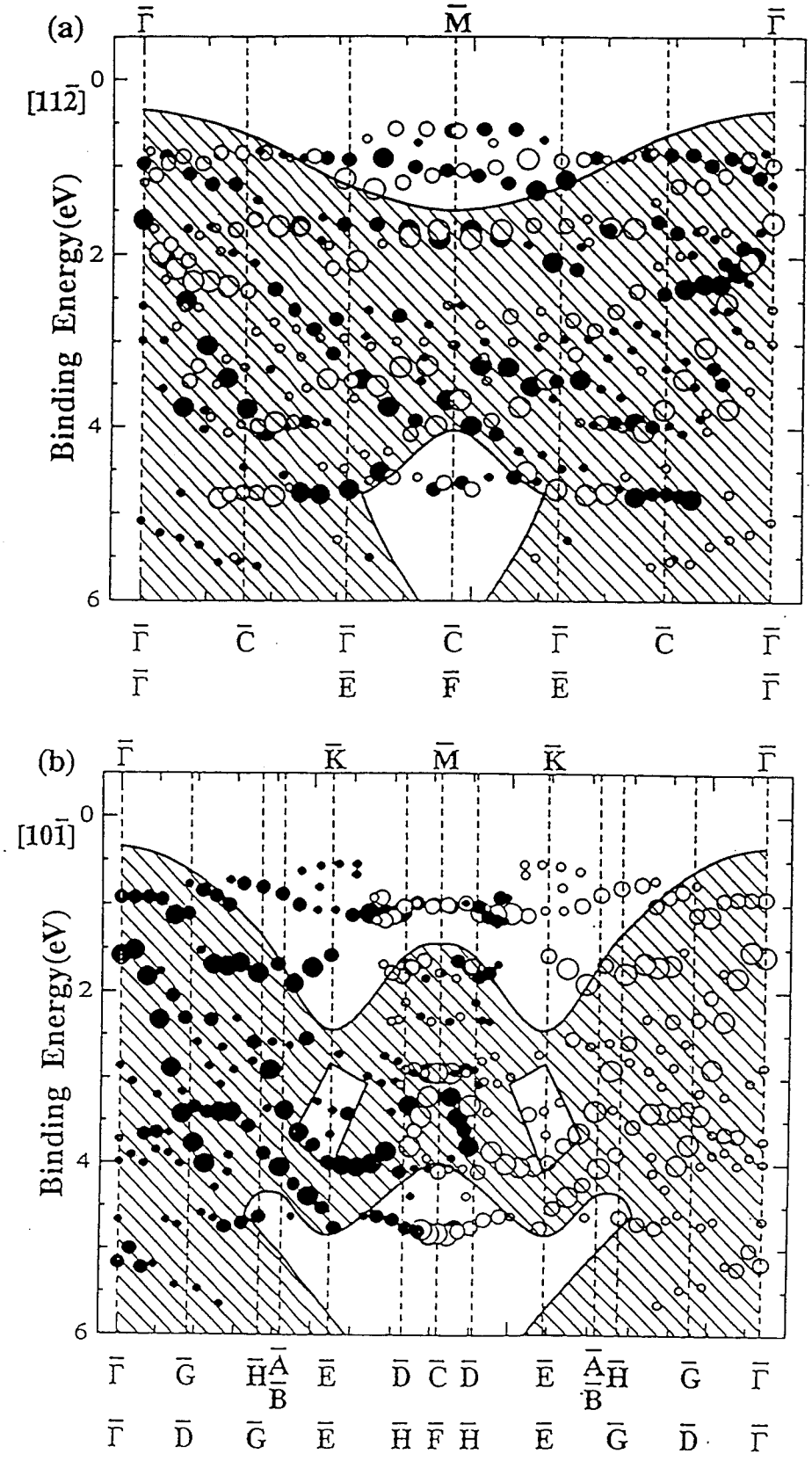

Figure 4.10: Dispersion of the electronic states of the Si(111)3×1-K surface along the (a) [11$\bar{2}$] and (b) [10$\bar{1}$] directions. The hatched area represents the projected bulk states.

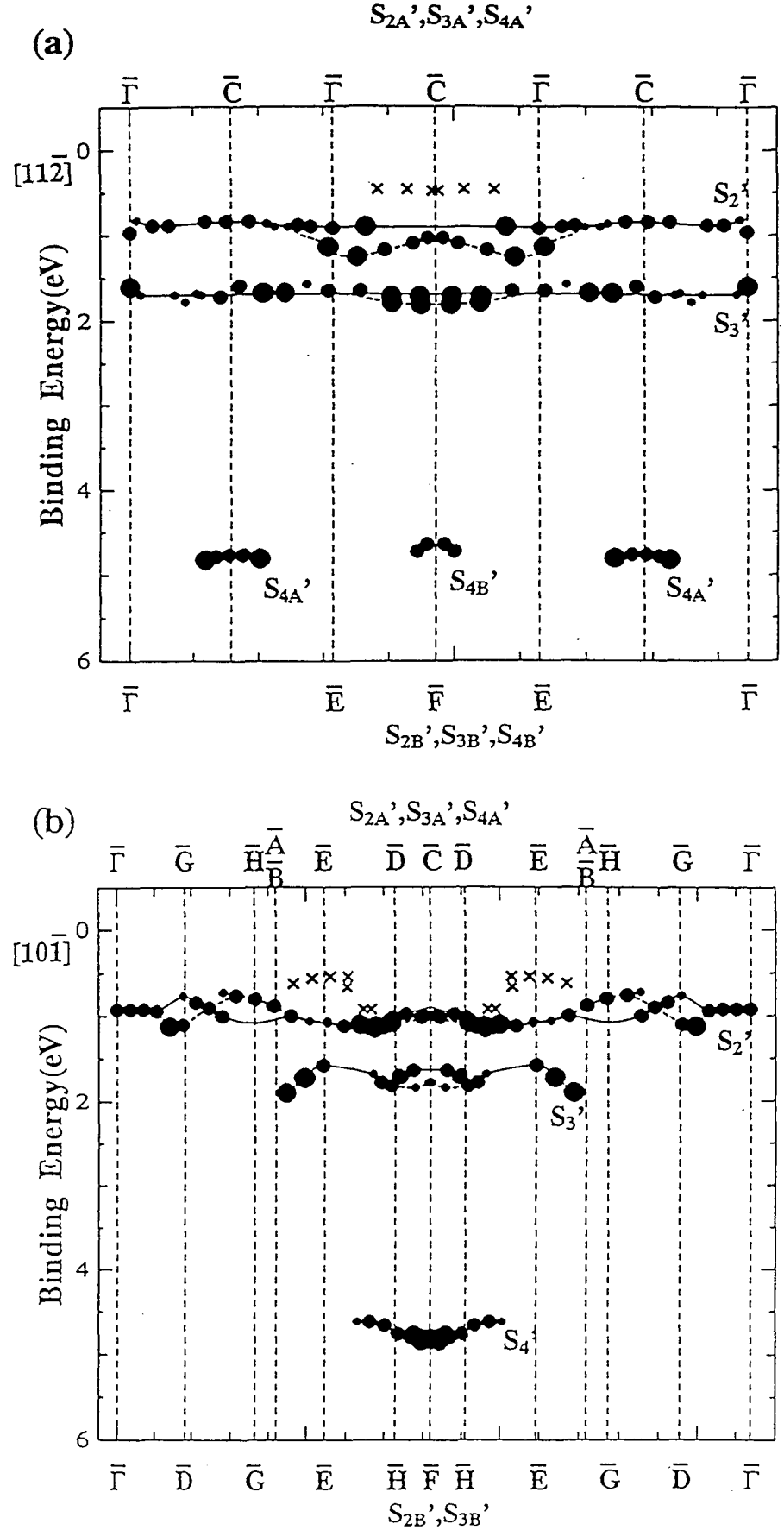

Figure 4.11: Dispersion of the surface states along the (a) [11$\bar{2}$] and (b) [10$\bar{1}$] directions.

$\rightarrow \bar{E} \rightarrow \bar{D} \rightarrow \bar{C} \rightarrow \bar{D} \rightarrow \bar{E} \rightarrow \bar{A}\bar{B} \rightarrow \bar{H} \rightarrow \bar{G} \rightarrow \bar{\Gamma}$ and $\bar{\Gamma} \rightarrow \bar{D} \rightarrow \bar{G} \rightarrow \bar{E} \rightarrow \bar{H} \rightarrow \bar{F} \rightarrow \bar{H} \rightarrow \bar{E} \rightarrow \bar{G} \rightarrow \bar{D} \rightarrow \bar{\Gamma}$, respectively. For S_{2A}', S_{2B}' and S_{3A}' the width of the dispersion is thus ~0 eV, ~0.35 eV and ~0 eV along the $[11\bar{2}]$ direction and ~0.42 eV, ~0.47 eV and ~0.32eV along the $[10\bar{1}]$ direction, respectively. We cannot estimate the width of the dispersion of S_{3B}', S_{4A}' and S_{4B}' because of the scanty number of data as a result of an appreciable overlap with the bulk bands.

We then compare the present result with the surface state of the Si(111)2×1 clean surface. Pandey [7] proposed the π-bonded chain model for this surface and calculated the surface state energy bands. The dispersions of the surface state of the Si(111)2×1 have been measured using ARUPS by Uhrberg *et al.*[12]. The dispersions calculated by Northrup *et al.*[15] are in good agreement with the experimental data of Uhberg *et al.*, but are a little different from those of Pandey. The main difference between these two theoretical results is the existence of an extremum of dispersion between the $\bar{\Gamma}$ and $\bar{J}$ points in the Northrup's model in contrast to no extremum in the Pandey's model. The predicted dispersion of the π-bonded chain along the $\bar{\Gamma}$-$\bar{J}$ and $\bar{J}$-$\bar{K}'$ directions, calculated by Northrup, are ~0.8 eV and ~0.08 eV, with the smallest E_B situated at the $\bar{K}'$ point ($\bar{J}$ and $\bar{K}'$ are the symmetry points of the 2×1 surface) [15]. Ignoring the extremum of the dispersion, that is, considering only the difference of E_B at the $\bar{\Gamma}$ and $\bar{K}'$ points, the difference is 0.57 eV. On the other hand, the width of the dispersion calculated by Pandey is almost the same (0.58 eV). The smallest E_B of the S_1' state is found near the $\bar{F}$ point in Fig. 4.11(a) (this point is not considered to be the $\bar{C}$ point from a comparison with the result on the 3×1-Na surface [99]) or $\bar{E}$ point in Fig. 4.11(b). We consider that the S_1' state is degenerated with the S_2' state at the $\bar{\Gamma}$ point (≈0.9 eV), because there is no other surface peak near this energy. The angular dispersion shown in Fig. 4.8(a) supports this assumption, because E_B of the S_1' state deviates downward with decreasing θ below 30°. Therefore, it is strongly suggested that the Si_1' state has a positive dispersion parallel to the chains, going from $\bar{\Gamma}$ to $\bar{K}$ of the

1×1 SBZ. The difference of E_B between the $\bar{\Gamma}$ point and the $\bar{F}$ point, which is on the way between the $\bar{J}$ and $\bar{K}'$ points in the 2×1 SBZ, becomes to ~0.48 eV in qualitative agreement with the above estimation. In the next place, the results of the dispersion along the $\bar{\Gamma}$-$\bar{J}'$ direction are much different between Pandey and Northrup *et al.*. The width calculated by Pandey is almost 0 eV, whereas the Northrup's result is 0.37 eV with the smallest E_B at the Γ point. We could not see any dispersion along the $\bar{\Gamma}$-$\bar{C}$ direction, which is the direction corresponding to their $\bar{\Gamma}$-$\bar{J}'$ direction. Thus our result is consistent with that of Pandey. Considering the similarity in the width of the dispersion (although we estimated only by the difference of E_B between at the $\bar{\Gamma}$ and $\bar{E}$ points for the [10$\bar{1}$] direction), which reflects the overlap of the involved wave function, as well as in the behavior of the dispersion along the equivalent directions of the 3×1 and 2×1 SBZ, the data points denoted by crosses in Fig. 4.11 is assigned to a part of the surface state derived from the π-bonded chain (S_1' state). It is not unrealistic that the Si(111)3×1-K surface contains reconstructed π-bonded chain.

Since the S_1' state is found at 0.5 eV below the Fermi level, the surface state band gap will be larger than 0.5 eV. On the Si(111)3×1-Na [99] surface the S_1' state is located at about 0.8 eV below the Fermi level and it was shown that the surface state band gap of this Na covered surface is ≈1 by STS [93]. These band gaps are appreciably larger than the value of 0.25 eV calculated by Pandey [7] for the Si(111)2×1 surface. But the experimentally reported values 0.45 eV [100] and 0.47 eV [101], for the Si(111)2×1 surface, are comparable with the present evaluation. The difference between the Si(111)2×1 and Si(111)3×1-K or Na surfaces may be due to the effect of the alkali metal. The difference between the Si(111)2×1 cleaved surface and the Si(111)3×1-(K, Na) surfaces may be due to the effect of the different structural relaxation or distortion.

Figure 4.12 summarizes the results of dispersion along the boundary of the 3×1 SBZ, that is for $\bar{\Gamma} \rightarrow \bar{G} \rightarrow \bar{H} \rightarrow \bar{A} \rightarrow \bar{F} \rightarrow \bar{B} \rightarrow \bar{E} \rightarrow \bar{D} \rightarrow \bar{C} \rightarrow \bar{\Gamma}$, from which the width of the

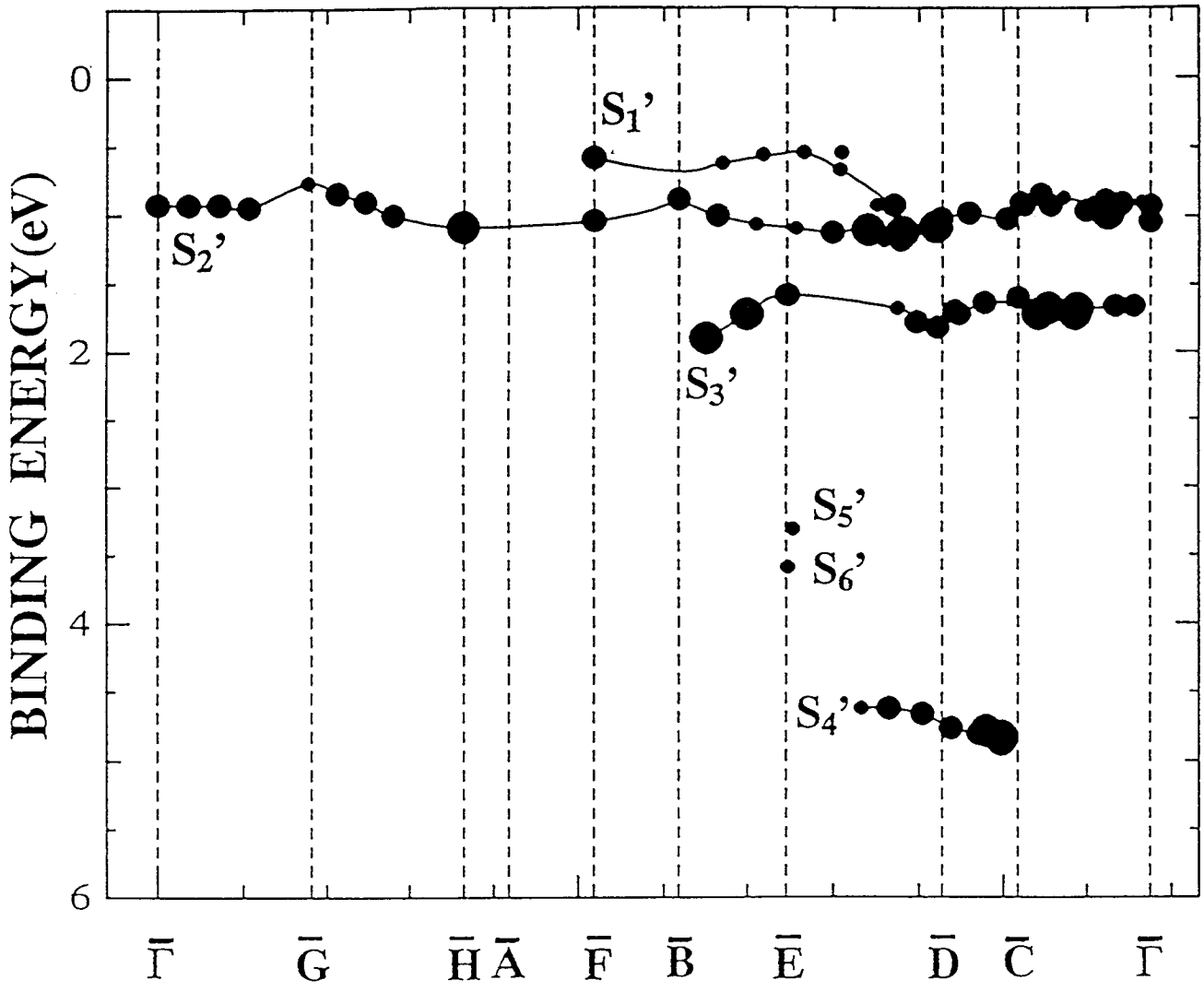

Figure 4.12: Dispersion along the boundary of the 3×1 surface Brillouin zone.

dispersion of the Si(111)3×1-K surface is estimated as ~0.48 eV for the S_1' state, ~0.47 eV for the S_2' state and ~0.32 for the S_3' state. In this figure, we can see clearly four surface state branches and two other surface states.

Table 1. Intensities of Si *LVV* Auger and K 2p and their intensity ratios (K/Si) measured by XPS.

	δ7×7	3×1
Si *LVV* Auger	1470	1640
K 2p	158.6	59
K/Si	0.1079	0.036

XPS results are summarized in Table 1. The peak intensities of the Si *LVV* Auger and the K 2p core emission as well as their ratio for the Si(111)δ7×7-K and the Si(111)3×1-K surfaces are tabulated. It is reminded that these surfaces correspond to the saturation coverage at room temperature and at 500°C. From this table, the saturation coverage of Si(111)3×1-K is determined to be 0.33 times as that of the saturation coverage at room temperature. Daimon *et al.* considered the saturation coverage of Si(111)δ7×7-K as one monolayer [79]. The atomic radius of the adsorbed K atoms (which is partially ionized) is considered to be smaller than that the in metallic phase (2.3Å) and larger than that of K^+ (1.3Å). There is also a fact that K atoms on the Si(001)2×1-K surface stack with the Si-Si distance of 3.84Å[102]. The half of the nearest neighbor distance of the Si atoms (3.84Å=1.92Å) is the same for the (001) and (111) surfaces. The atomic radius of the adsorbed K, which is partly ionized, is comparable to or smaller than this value (1.92Å) and the K saturation coverage of 1 ML on the Si(111)δ7×7-K is not unrealistic. On the other hand, the photoemission data in ref.[96] have suggested one K atom per Si dangling bond, i.e. the saturation coverage as 19/49≈0.4 ML, for the Si(111)δ7×7-K surface. Taking account their result, the saturation coverage of the Si(111)δ7×7-K surface will be more than 19/49, when all dangling bonds are terminated with one or more K atoms, like the

Si(111)δ7×7-H surface [103][104]. Then we think the lower limit of the saturation coverage of the Si(111)3×1-K surface as 0.13 ML (19/49×1/3) and the upper limit as 1/3 ML, and the number of K atom in the 3×1 unit mesh of the 3×1 structure will be between 0.4 and 1. Considering these limits, we prefer the saturation coverage of 1/3 ML, because the number of K atom in the 3×1 unit mesh should naturally be an integer. This result is consistent with the recent ISS result of Hashizume *et al.*[87]. But, this value is much different from that estimated by RHEED [79] or those of STM [86][92][93], which proposed the saturation coverage of 2/3 ML. This difference might be caused if the sample temperature of those experiments was not high enough, and the structures were not completely 3×1 and with mixture of the δ7×7 surface leading to the coverage larger than ours. As for the STM image, we will argue it later. Besides, the value reported by Fan *et al.*[91] (0.01 ML) is much smaller than ours. This difference may be caused by the difference of the sample preparation method of the 3×1 surface. That is, they first exposed the surface to the alkali metal at room temperature and then annealed it at higher temperature ($\approx$800°C) to make a 3×1 structure. In this method, the alkali metal atoms might have partly desorbed and the coverage might have become much less than ours.

From the present results, we propose a new structure model for the Si(111)3×1-K surface as shown in Fig. 4.13 in which (a) shows the side view and (b) shows the top view of this surface. The open red-circles represent the position of the Si atoms, the largest ones those of the first layer of the Si(111)1×1 ideal surface, the next one those of the second layer, etc. The full-red circles represent the Si atoms which constitute the π-bonded chain and the full-blue circles represent the K atoms. The broken line represents the unit mesh of the 3×1 structure and the red line the π-bonded chain. This model is similar to that proposed by Wan *et al.*[92], but there are two different points. First, the number of alkali metal in the unit cell is not two but one, suggesting the clear difference of the saturation coverage. Second, in the model of Wan *et al.*, the dangling bonds of the "π-bond like"

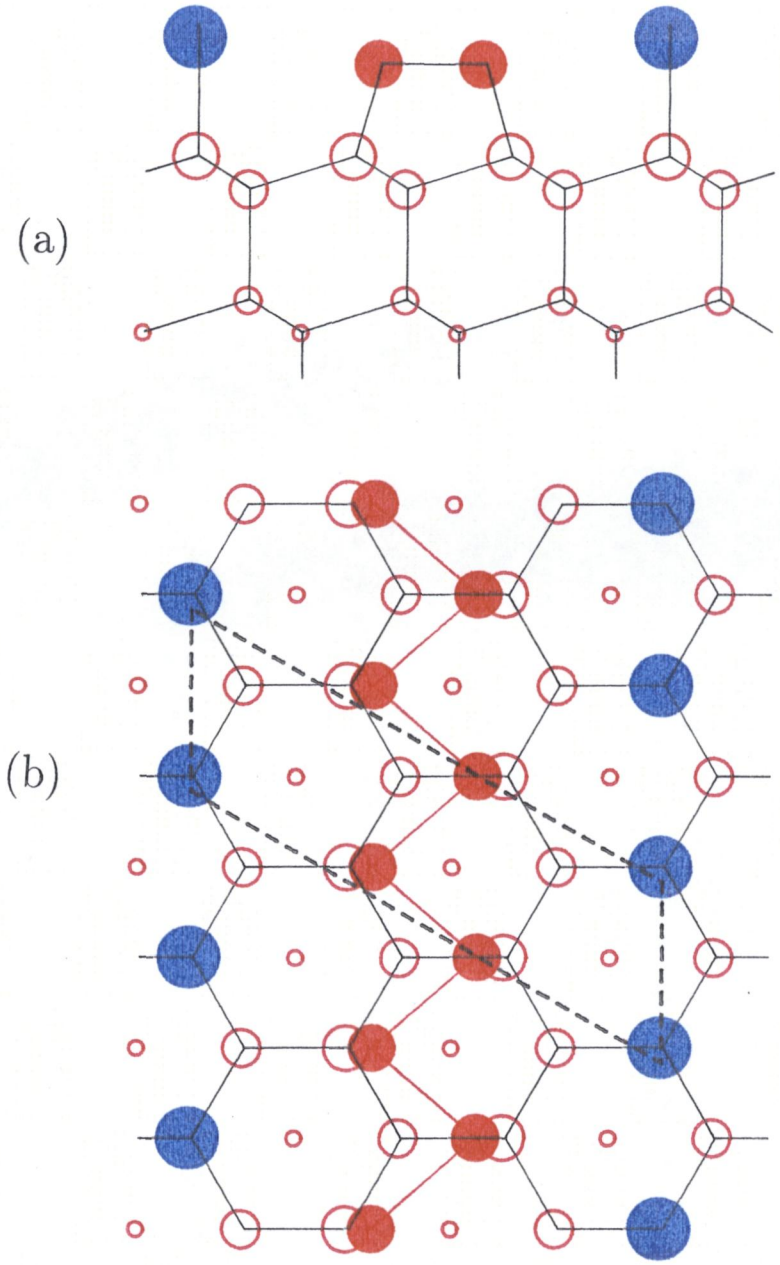

Figure 4.13: New structure model for the Si(111)3×1-K surface (a)side view and (b) top view. The open red-circles represent the position of the Si atoms, the largest ones those of the first layer of the Si(111)1×1 ideal surface, the next one those of the second layer, etc. The full-red circles represent the Si atoms which constitute the π-bonded chain and the full-blue circles represent the K atoms. The broken line represents the unit mesh of the 3×1 structure and the red line the π-bonded chain.

Si atoms are terminated by the Li atoms. But in our model, they are not terminated by alkali metals, and these dangling bonds make the π-bonded chain like the Si(111)2×1 surface. The present model can explain the result of the STM experiment [86][92][93] from a different stand point. Namely, the filled electronic state probed by the STM is not due to the K atoms but due to the dangling bonds of the π-bonded chain Si atoms in accord with the zig-zag image of the STM, and the empty state is not resulting from the Si atoms but from the K atoms. Considering the difference between the direction of the dangling bonds of the 5-fold rings and that of the 7-fold rings, the dispersion of the present π-bond surface state should be much smaller than that of the Si(111)2×1 surface, because the dangling bonds on the 5-fold rings are tilted compared with those of the 7-fold rings in which they are nearly parallel. Although this is an unsolved problem, this model still seems reasonable allowing the previous interpretation of STM data [86][92][93]. But we have to mention that some kind of structural relaxation of distortion is probably needed to open a large band gap. Therefore, we think that this model is only tentative and more structural data and/or theoretical work are needed.

According to this model, the number of the clear surface states will be at least four: (a) surface state of the π-bond, (b) that of the Si-K bonding, (c) that of the σ-bond among the π-bonded chain Si atoms and (d) that of the σ-bond between the first layer Si atoms and the π-bonded chain Si atoms. Judging from the similarity of the dispersion as discussed above, the S_1' state is assigned to (a). The UPS spectra measured by Tezuka *et al.*[97] and Magnusson *et al.*[96] have a surface state at ~1 eV below the Fermi level. Considering the similarity of E_B and the structure of Si-K bonding (on-top site for the Si(111)δ7×7-K surface), the S_2' state is assigned to (b). Himpsel *et al.*[13] observed three surface states on the Si(111)2×1 surface. One will be the surface state of the π-bond and the others the surface states which are caused by the π-bonded chain, that is (c) and (d). We have only few information about the S_3' and S_4' states, but according to the result of Himpsel *et*

al.[5], these surface states could be (c) and (d).

Figure 4.14 shows the change of the work function against the deposition time of K for the Si(111)δ7×7-K surface at room temperature. The work function of the Si(111)3×1-K is also shown by an open circle at its deposition time at 500°C. We have to pay attention to the difference of the sticking coefficient at different temperatures (room temperature and 500°C). The reduction of the work function of the surface for the saturation coverage is 2.95 eV (which is almost the same as that of reference [96]) for the Si(111)δ7×7-K surface and 1.37 eV for the Si(111)3×1-K surface. We conclude that a saturated monolayer for the Si(111)δ7×7-K is formed after 5.5min under this deposition condition. The saturation coverage of the Si(111)3×1-K surface is formed after 3.5min of K deposition. One should also be reminded of the temperature difference of the Si substrate. The deposition time for the saturation coverage of the Si(111)3×1-K surface is not 1/3 of the Si(111)δ7×7-K because the K atoms not only adsorb on the Si surface but also desorb from it at 500°C. It might be simply thought that the change of the work function of the Si(111)3×1-K surface will be 1/3 of that of the Si(111)δ7×7-K surface in contrast to our present result. But, since the work function changes radically in the early stage of adsorption and the change becomes less with increasing the K adsorption due to the dipole-dipole interaction, we have to compare the change of work function for the Si(111)3×1-K surface to that for the Si(111)δ7×7-K surface at 1/3 ML. The work function change of the Si(111)3×1-K surface is smaller than that of the Si(111)δ7×7-K surface at the deposition time corresponding to 1/3 of the saturation value. This small work function change of the 3×1-K surface compared with the 1/3 ML δ7×7-K surface can also be explained by our new model. Looking at the Fig. 4.13(a), we recognize that the interlayer distance between the layer of K atoms and that of π-bonded chain Si atoms is very short. Hence, the dipole moment between the K layer and the Si layer must be small. On the other hand, K atoms are thought to be adsorbed at the on-top site on the Si(111)δ7×7-K surface. So, the work function change

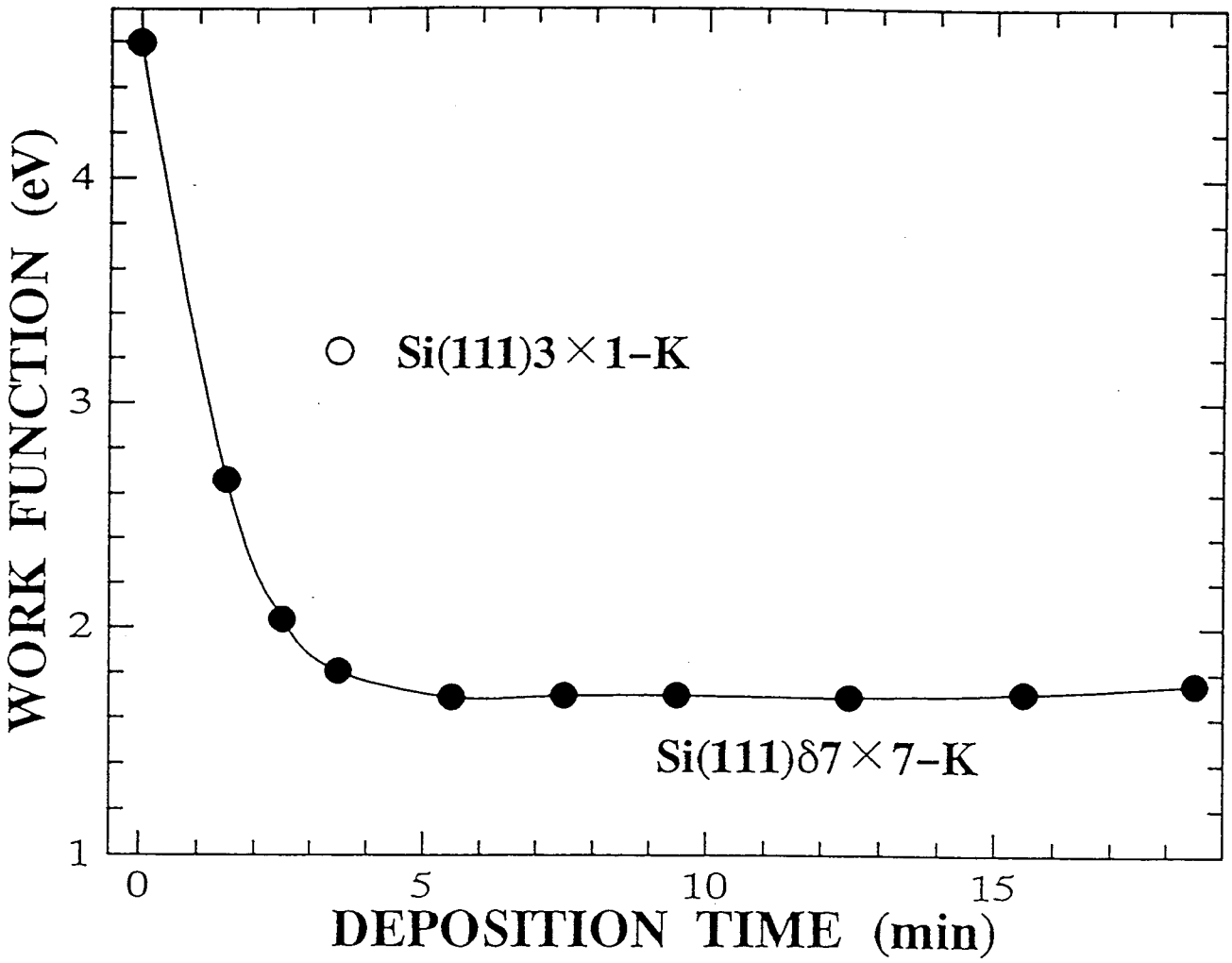

Figure 4.14: Change of the work function against the deposition time for the Si(111)δ7×7-K and the Si(111)3×1-K surface.

should be larger than that of the 3×1-K surface, because of the larger interlayer distance and larger dipole moment.

In this model for the 3×1-K surface, no dangling bond remains and the surface should not be metallic but semiconducting. So, this surface structure model is consistent with the semiconducting surface electronic state. Our results of the Si 2p core level shift for the Si(111)3×1-Na surface [94] also support these results.

4.4 Summary

The surface electronic states and the saturation coverage of the Si(111)3×1-K surface are studied using not only angle-resolved ultraviolet photoelectron spectroscopy but also X-ray photoelectron spectroscopy. It is found for the Si(111)3×1-K that the S_1 state of the Si(111)7×7 clean surface at ~0.2 eV below the Fermi level on the clean surface disappears and new surface states S_2' and S_3' clearly appear at 0.95 eV and 1.6 eV below the Fermi level, with no Fermi level crossing. So, the Si(111)3×1-K surface is no longer a metallic surface as the Si(111)7×7 clean surface but a semiconducting surface. We measured the dispersion along the $[11\bar{2}]$ and $[10\bar{1}]$ directions and found other surface states, S_1' and S_4'. We discussed these surface states in this chapter. The other surface states observed at 3.39 and 3.67 eV below the Fermi level are not discussed here. The magnitudes of the band dispersions are ~0.48 eV for the S_1' state, ~0.47 eV for the S_2' state and ~0.32 eV for the S_3' state. We cannot evaluate the width of the dispersion of the S_4' state because of the scanty number of data. Judging from the dispersion behavior, the S_1' and S_2' states have been assigned to the surface state of the π-bond and that of the Si-K bonding, respectively. Taking into account the results of other experiments the S_3' and S_4' states might be assigned to the σ-bond among the π-bonded chain Si atoms and that of the σ-bond between the first layer Si atoms and the π-bonded chain Si atoms, respectively.

The saturation coverage of the Si(111)3×1-K surface was estimated to be 1/3 ML from

a comparison of the Si Auger and the K 2p photoemission intensity ratio with that of the Si(111)δ7×7-K surface on which the saturation coverage is thought to be 1 ML.

Based on these results we have proposed a new model of the Si(111)3×1-K surface. This model can explain the semiconducting surface electronic state, STM image, the smaller work function change compared with that of the Si(111)δ7×7-K surface as well as the dispersion and the number of surface states.

Chapter 5

Summary

The understanding of oxidation of Si surfaces is important not only from scientific but also technological viewpoint for silicon oxide. A large number of studies have been done both experimentally and theoretically for the O_2/Si(111) surface. We have studied the adsorption states and desorption processes of ions by means of ESD for this surface. The ESD experiment was done at room temperature. By measuring the TOF spectra, we observed H^+, O^+ and O_2^+ as desorbed ions at low exposures (1 and 2 L), whereas only H^+ and O^+ were observed at high exposures (above 4 L). The desorbing species was different from that observed in an early study [60]. It was the first observation of O_2^+ in the ESD experiment. With increasing the coverage, the signal of O_2^+ disappeared. It is considered that O_2^+ desorbs from the molecular surface species. The oxygen adsorbs only dissociatively at high exposure, although molecular surface species survive at low coverage at room temperature.

The ESDIAD pattern of the desorbed O_2^+ was concentrated near the center of the screen, which corresponds to the surface normal direction. This ESDIAD pattern is reconciled with the model that the molecular surface species are adsorbed at the on-top surface site. We measured the lifetime of molecular surface species by means of the decrease of the intensity of the desorbed O_2^+ in the TOF spectra. Its lifetime was measured to be about 8 hours for 1 L exposure. Measuring the lifetime at different temperatures, we obtained the thermal activation energy as 0.56 eV for 1 L exposure. Because both the lifetime and thermal activation energy are different from the value suggested by Höfer *et al.*[63], we think that

we have observed another molecular surface species.

The study of reactions of nitric oxide on solid surfaces is interesting from both technological and scientific points of view. From the technological view point, NO is one of the harmful combustion exhaust gases. So it is desirable to find efficient catalysis and methods to convert NO into harmless gases. From the scientific view point, NO molecule is very interesting because it has one unpaired electron in the antibonding ($2\pi^*$) orbital. We have studied the adsorption sites and desorption mechanism of the NO/Si(111) surface using both ESD and PSD.

The ESD experiments were done at 190 K and room temperature, and the PSD was done at 90 K. In the ESD experiment the desorbing ion species were H^+ and O^+ at room temperature. In addition, N^+ was observed for the first time in the ESD experiment at 190K. Measuring the kinetic energy distribution of the desorbed ions, we found their threshold at about -1.0 eV for the NO/Si(111) surfaces. Compared with NO/Si(111), the threshold for the O_2/Si(111) surface [81] (chapter 2, Fig. 2.7) stayed around 0 eV for any exposure. From the difference in these two systems, we concluded that the barrier height is lowered by about 1 eV in the ion desorption process on the NO adsorbed surface, whereas it is hardly changed on the O_2/Si(111) surface.

We have found two types of N^+ which have different kinetic energies. From the ESDIAD patterns of these two types of N^+, we have found that these two types correspond to the two adsorption sites of NO. In the PSD experiment at 90 K, NO^+, O_2^+ and N_2O^{2+} were observed for the first time in addition to the H^+, O^+ and N^+ ions. From the photon energy dependence of the PSD experiment and the UPS spectra, we have found that N^+ desorbs from the molecularly adsorbed NO through the excitation of the 3σ molecular orbital which is mainly O 2s. This result suggests that N^+ ions desorb from the NO molecules which are bonding to the surface Si atoms with the O atoms, like Si$-$O$-$N, following the mechanism of KF model [39].

Studies of alkali metal adsorption on semiconductor surfaces are very interesting subjects with respect to the changes of the geometrical and electronic structures of the surface. Among these, the Si(001)-K and Si(111)-K systems have been studied most extensively [82]-[87]. The structure of Si(111)3×1-K surface, which was found by Daimon *et al.*[79], was studied by means of STM [86]-[93], and some structural models were proposed. The saturation coverage of this surface was measured using STM [86]-[93], AES [91], ISS [87] and core-level shift [94], but the value is not definite yet. Therefore, the structural model and the saturation coverage of these alkali metal adsorbed 3×1 surfaces are still controversial problems.

We studied the surface electronic states and the saturation coverage of the Si(111)3×1-K surface by means of ARUPS and XPS. The electronic states were measured along the $[11\bar{2}]$ and the $[10\bar{1}]$ directions. Comparing the spectra of the Si(111)7×7 clean surface and that of the Si(111)3×1-K surface, we have found that the S_1 state of the clean surface disappears and new surface states appear. According to the disappearance of the S_1 state of the clean surface and the fact that no spectrum has shown appreciable intensity at the Fermi level, we concluded that the 3×1-K surface is no longer metallic as the 7×7 clean surface but semiconducting. Measuring the dispersion, we found 6 surface states. Judging from the dispersion behavior of one of them (S_1' state), the 3×1-K surface seems to contain π-bonded chains. The saturation coverage of K on the Si(111)3×1-K surface is found to be 1/3 ML from the comparison of the intensity ratio between the Si LVV Auger and K 2p peaks with that of the Si(111)δ7×7-K surface, on which the saturation coverage is considered to be 1 ML. Based on these results, we propose a new surface geometrical structure model for the Si(111)3×1-K surface. This model can explain the semiconducting surface, the STM image, the smaller work function change compared with that of the Si(111)δ7×7-K surface.

Bibliography

[1] T.N.Rhodin and J.W.Gadzuk: In *The Nature of the Surface Chemical Bond* (eds. Rhodin and Ertl), (1979) pp.113-273. Amsterdam, North-Holland.

[2] G.A.Somorjai: *Chemistry in Two Dimensions Surfaces* (1981). Ithaca, Cornell.

[3] D.R.Penn: Phys. Rev. **B13** (1976) 5248.

[4] K.Haneman: Phys. Rev. **121** (1961) 1093.

[5] F.J.Himpsel, P.Heimann and D.E.Eastman: Phys. Rev. **B24** (1981) 2003.

[6] F.J.Himpsel *et al.*: Phys. Rev. Lett. **45** (1980) 1112; S.Brennan *et al.*: Phys. Rev. Lett. **45** (1980) 1414.

[7] K.C.Pandey: Phys. Rev. Lett. **47** (1981) 1913.

[8] K.C.Pandey: Phys. Rev. **B25** (1982) 4338.

[9] D.E.Eastman and G.W.Gobeli: Phys. Rev. Lett. **28** (1972) 1378.

[10] L.F.Wagner and W.E.Spicer: Phys. Rev. Lett. **28** (1972) 1381.

[11] A.W.Parke, A.McKinley and R.H.Williams: J. Phys. **C11** (1978) L993.

[12] R.I.G.Uhrberg, G.V.Hansson, J.M.Nicholls and S.A.Flodström: Phys. Rev. Lett. **48** (1982) 1032.

[13] F.J.Himpsel: Appl. Phys. **A38** (1985) 205.

[14] J.Bokor, R.Storz, R.R.Freeman and P.H.Bucksbaum: Phys. Rev. Lett. **57** (1986) 881.

[15] J.E.Northrup and M.L.Cohen: Phys. Rev. Lett. **49** (1982) 1349.

[16] P.Perfetti, J.M.Nicholls and B.Reihl: Phys. Rev. **B36** (1987) 6160.

[17] K.C.Pandey: Physica **117&118B** (1983) 761.

[18] N.Osakabe, Y.Tanishiro, K.Yagi and G.Honjo: Surf. Sci. **109** (1981) 353.

[19] K.Takayanagi, Y.Tanishiro, M.Takahashi and S.Takahashi: J. Vac. Sci. Technol. **A3** (1985) 1502; K.Takayanagi, Y.Tanishiro, S.Takahashi and M.Takahashi: Surf. Sci. **164** (1985) 367.

[20] T.Yokotsuka, S.Kono, S.Suzuki and T.Sagawa: Solid State Commun. **39** (1981) 1001.

[21] F.J.Himpsel and T.Fauter: J. Vac. Sci. Technol. **A2** (1984) 815.

[22] R.J.Hamers, R.M.Tromp and J.E.Demuth: Phys. Rev. Lett. **56** (1986) 1972.

[23] D.Menzel and R.Gomer: J. Chem. Phys. **40** (1964) 1164.

[24] D.Menzel and R.Gomer: J. Chem. Phys. **41** (1964) 3311.

[25] P.A.Redhead: Canad. J. Chem. Phys. **42** (1964) 886.

[26] Y.Ishikawa: Rev. Phys. Chem. Jpn. **16** (1942) 83 and 117.

[27] Y.Ishikawa: Proc. Imp. Acad. (Tokyo) **18** (1942) 246 and 390.

[28] Y.Ishikawa: Proc. Imp. Acad. (Tokyo) **19** (1943) 380 and 385.

[29] P.R.Antoniewicz: Phys. Rev. **B21** (1980) 3811.

[30] Q.J.Zhang and R.Gomer: Surf. Sci. **109** (1981) 567.

[31] Q.J.Zhang and R.Gomer: Surf. Sci. **129** (1983) 535.

[32] E.R.Moog, J.Unguris and M.B.Webb: Surf. Sci. **134** (1983) 849.

[33] M.L.Yu: Phys. Rev. **B19** (1979) 5995.

[34] P.Feulner, D.Menzel, H.J.Kreuzer and Z.W.Gortel: Phys. Rev. Lett. **53** (1984) 671.

[35] Z.W.Gortel, H.J.kreuzer, P.Feulner and D.Menzel: Phys. Rev. **B35** (1987) 8951.

[36] Z.W.Gortel, H.J.Kreuzer, P.Feulner and D.Menzel: *Desorption Induced by Electronic Transitions* DIET III, p.173, Springer Series in Surface Sciences **13** (Springer-Verlag, Berlin, 1988).

[37] Z.W.Gortel, R.Teshima and H.J.Kreuzer: Phys. Rev. **B37** (1988) 3183.

[38] R.E.Walkup, Ph.Avouris, N.D.Lang and R.Kawai: Phys. Rev. Lett. **63** (1989) 1972.

[39] P.J.Feibelman and M.L.Knotek: Phys. Rev. **B18** (1978) 6531.

[40] R.Francy and D.Menzel: Phys. Rev. Lett. **13** (1979) 865.

[41] D.R.Jennison and D.Emin: J. Vac. Sci. Technol. **A1** (1983) 1154.

[42] D.E.Ramaker, C.T.White and J.S.Murday: J. Vac. Sci. Technol. **18(3)** (1981) 748.

[43] D.Pooley: Solid State Commun. **3** (1965) 241.

[44] D.Pooley: Proc. Phys. Soc. (London) **87** (1966) 245.

[45] D.Pooley: Proc. Phys. Soc. (London) **87** (1966) 257.

[46] H.N.Hersh: Phys. Rev. **148** (1966) 928.

[47] R.Jaeger, J.Stöhr and T.Kendelewicz: Surf. Sci. **134** (1983) 547.

[48] R.Jaeger, J.Stöhr and T.Kendelewicz: Phys. Rev. **B28** (1983) 1145.

[49] D.Purdie, C.A.Muryn, N.S.Prakash, P.L.Wincott, G.Thornton and D.S.-L.Law: Surf. Sci. **251/252** (1991) 546.

[50] J.J.Czyzewski, T.E.Madey and J.T.Yates,Jr.: Phys. Rev. Lett. **32** (1974) 777.

[51] T.E.Madey, J.J.Czyzewski and J.T.Yates,Jr.: Surf. Sci. **49** (1975) 465.

[52] D.P.Woodruff and D.J.Godfrey: Solid State Commun. **34** (1980) 679.

[53] D.P.Woodruff: Surf. Sci. **124** (1983) 320.

[54] W.C.Clinton: Surf. Sci. **112** (1981) L791.

[55] Z.Misković, J.Vukanić and T.E.Madey: Surf. Sci. **169** (1986) 405.

[56] N.V.Smith, M.M.Traum and F.J.DiSalvo: Solid State Commun. **15** (1974) 211.

[57] H.Daimon, Rev. Sci. Instrum. **59** (1988) 545, **61** (1990) 205.

[58] H.Daimon and S.Ino, J. Vac. Soc. Jpn. **31** (1988) 954.

[59] H.Daimon and S.Ino, Rev. Sci. Instrum. **61** (1990) 57.

[60] M.Nishijima, K.Fujiwara and T.Murotani, J. Appl. Phys. **46** (1975) 3089.

[61] K.Edamoto, H.Kobayashi, M.Onchi and M.Nishijima, J. Chem. Phys. **83** (1985) 428.

[62] M.Nishijima, K.Edamoto, Y.Kubota, H.Kobayashi and M.Onchi, Surf. Sci. **158** (1985) 422.

[63] U.Höfer, P.Morgen, W.Wurth and E.Umbach, Phys. Rev. **B40** (1989) 1130.

[64] Ph.Avouris, I.-W.Lyo and F.Bozso, J. Vac. Sci. & Technol. **B9** (1991) 424.

[65] J.P.Pelz and R.H.Koch, Phys. Rev. **B42** (1990) 3761.

[66] S.Ciraci, S.Ellialtioglu and S.Erkoc, Phys. Rev. **B26** (1982) 5716.

[67] I.P.Batra, P.S.Bagus and K.Hermann, Phys. Rev. Lett. **52** (1984) 384.

[68] G.Herzgerg: *Molecular Spectra and Molecular Structure*, vol.1, Van Nastrand, Princeton (1950).

[69] I.-W.Lyo, Ph.Avouris, B.Schubert and R.Hoffmann: J. Phys. Chem. **94** (1990) 4400.

[70] K.Ueda, *private communication.*

[71] K.Sakamoto, K.Nakatsuji, H.Daimon, T.Yonezawa, S.Suga, H.Namba and T.Ohta: submitted to Phys. Rev.

[72] T.Yonezawa, H.Daimon, K.Nakatsuji, K.Sakamoto and S.Suga: to be submitted to Phys. Rev. Lett.

[73] M.Nishijima and K.Fujiwara: Solid State Commun. **24** (1977) 101.

[74] Z.Ying and W.Ho: J. Vac. Sci. Technol. **A7(3)** (1989) 2099 and J. Chem. Phys. **91** (1989) 2689.

[75] T.Isu and K.Fujiwara: Solid State Commun. **42** (1982) 477.

[76] Z.Ying and W.Ho: Phys. Rev. Lett. **60** (1988) 57.

[77] M.D.Wiggins, R.J.Baird and P.Winblatt: J. Vac. Sci. Technol. **18(3)** (1981) 965.

[78] Da-Ren He and F.W. Smith: Surf. Sci. **154** (1985) 347.

[79] H.Daimon and S.Ino, Surf. Sci. **164** (1985) 320.

[80] H.Namba, M.Masuda, H.Kuroda, T.Ohta and H.Noda, Rev. Sci. Instrum. **60** (1989) 1917.

[81] K.Sakamoto, K.Nakatsuji, H.Daimon, T.Yonezawa and S.Suga: accepted in Surf. Sci.

[82] H.Tochihara: Surf. Sci. **126** (1983) 523.

[83] T.Aruga, H.Tochihara and Y.Murata:Phys. Rev. Lett. **33** (1984) 372.

[84] Y.Enta, T.Kinoshita, S.Suzuki and S.Kono: Phys. Rev. **B36** (1987) 9801.

[85] Y.Enta, T.Kinoshita, S.Suzuki and S.Kono: Phys. Rev. **B39** (1989) 1125.

[86] T.Hashizume, Y.Hasegawa, I.Sumita and T.Sakurai: Surf. Sci. **246** (1991) 189.

[87] T.Hashizume, M.Katayama, D.Jeon, M.Aono and T.Sakurai: Jpn. J. Appl. Phys. **32** (1993) L1263.

[88] S.Mizuno and A.Ichimiya: Appl. Surf. Sci. **33/34** (1988) 38.

[89] W.C.Fan and A.Ignatiev: Phys. Rev. **B40** (1989) 5479.

[90] J.Quinn and F.Jona: Surf. Sci. Lett. **249** (1991) L307.

[91] W.C.Fan and A.Ignatiev: Phys. Rev. **B41** (1990) 3592.

[92] K.J.Wan, X.F.Lin and J.Nogami: Phys. Rev. **B46** (1992) 13635.

[93] D.Jeon, T.Hashizume, T.Sakurai and R.F.Willis: Phys. Rev. Lett. **69** (1992) 1416.

[94] T.Okuda, H.Shigeoka, H.Daimon, S.Suga, T.Kinoshita and A.Kakizaki: 1992 Activity Report of Synchrotron Radiation Laboratory, Institute for Solid State Physics, The University of Tokyo, p.66.

[95] U.A.Ditzinger, Ch.Lunau, B.Schieweck, St.Tosch and H.Neddermeyer: Surf. Sci. **211/212** (1989) 707.

[96] K.O.Magnusson and B.Reihl: Phys. Rev. **B41** (1990) 12071.

[97] Y.Tezuka, H.Daimon and S.Ino: Jpn. J. Appl. Phys. **29** (1990) 1773.

[98] K.C.Pandey: Phys. Rev. **B14** (1976) 1557.

[99] T.Okuda, K.Sakamoto, H.Nishimoto, H.Daimon, S.Suga, T.Kinoshita and A.Kakizaki: to be submitted.

[100] Per Mårtensson, A.Cricenti and G.V.Hansson: Phys. Rev. **B32** (1985) 6959.

[101] M.A.Olmstead and N.M.Amer: Phys. Rev. Lett. **52** (1984) 1148.

[102] T.Abukawa and S.Kono: Surf. Sci. **214** (1989) 141.

[103] A.Ichimiya and S.Mizuno: Surf. Sci. **191** (1987) L765.

[104] J.J.Boland: Surf. Sci. **244** (1991) 1.

List of Publications

1. "Electron Stimulated Desorption (ESD) of O_2/Si(111) surface"
   K.Sakamoto, K.Nakatsuji, H.Daimon, T.Yonezawa and S.Suga:
   accepted in Surf. Sci.

2. "Electron- and Photon-Stimulated Desorption of the NO/Si(111) surface"
   K.Sakamoto, K.Nakatsuji, H.Daimon, T.Yonezawa, S.Suga, H.Namba and T.Ohta:
   submitted to Phys. Rev.

3. "Photoemission Study of the Si(111)3×1-K surface."
   K.Sakamoto, T.Okuda, H.Nishimoto, H.Daimon, S.Suga, T.Kinoshita and A.Kakizaki:
   submitted to Phys. Rev.

4. "Adsorption and Desorption Processes of Cl on Si(111)7×7 surface"
   T.Yonezawa, H.Daimon, K.Nakatsuji, K.Sakamoto and S.Suga:
   accepted in Appl. Surf. Sci.

5. "PSD Mechanism of Cl^+ Ions from Cl/Si(111) Surface"
   T.Yonezawa, H.Daimon, K.Nakatsuji, K.Sakamoto, S.Suga, H.Namba and T.Ohta:
   submitted to Jpn. J. Appl. Phys.

6. "Energy Barrier for Ion Desorption"
   T.Yonezawa, H.Daimon, K.Nakatsuji, K.Sakamoto and S.Suga:
   to be submitted to Phys. Rev. Lett.

7. "Angle Resolved Photoelectron Spectroscopy of the Si(111)3×1-Na surface"
   T.Okuda, K.Sakamoto, H.Nishimoto, H.Daimon, S.Suga, T.Kinoshita and A.Kakizaki:
   to be submitted.